RANS-CFD Based Assessment of Corrections Applied to the Measured Characteristics of Supersonic Configurations in a Low Speed Wind Tunnel

Nicolas Mavriplis

A thesis

submitted in partial fulfillment of the

requirements for the degree of

Master of Science in Aeronautics and Astronautics

University of Washington
2022

Reading Committee:
Eli Livne, Chair
Mohammed Reza Soltani

Program Authorized to Offer Degree:
Aeronautics & Astronautics

University of Washington

Abstract

RANS-CFD Based Assessment of Corrections Applied to the Measured Characteristics of Supersonic Configurations in a Low Speed Wind Tunnel

Nicolas Mavriplis

Chair of the Supervisory Committee:

Professor Eli Livne
Aeronautics & Astronautics

The CFD software package Star-CCM+ was used to investigate the effects of the model support system and test section walls on a double-delta wing, representative of long-range supersonic configurations, in the University of Washington's Kirsten Wind Tunnel in an effort to improve current wind tunnel test corrections. The Star-CCM+ simulation-derived support corrections were validated using past wind tunnel models and support corrections. Simulations indicated that the interference effects due to the model support system are non-negligible and must be accounted for. New model support corrections were computed using CFD and wind tunnel data. Wall effects corrections were also evaluated via RANS CFD and results compared well to classical corrections traditionally applied by the Kirsten Wind Tunnel. The pitching moment curve slope was underpredicted, however, with CFD simulations. Engine nacelle form factors were also calculated with Star-CCM+ to add new nacelle internal duct drag corrections to wind tunnel data. All CFD derived corrections were applied to past uncorrected wind tunnel data, compared to data with KWT's standard corrections, and to Star-CCM+ simulations of the models in freestream conditions. The CFD derived corrections appear to improve the resulting "free flight" wind tunnel data for the wing alone case. More work is necessary, however, for full configurations and CFD-based corrections should be validated with follow-on dedicated "Tare and Interference" (T&I) testing.

Acknowledgements

First and foremost, I would like to thank Eli Livne for his support through-out my academic career, both in undergraduate and graduate school. I am more than privileged to have an advisor who has been patient, understanding, supportive, and encouraging through my academic and personal ventures. Chet Nelson has also immensely impacted my academic career in both undergraduate and graduate school. He has taught me an incredible amount of knowledge on airplane design and aerodynamics and instilling intuition and logic with knowledge. I would also like to thank Reza Soltani for his support and guidance through the years. His willingness to meet often to talk through problems and his aerodynamic expertise has helped much. I also need to thank Eddie Ting, my research partner, for his constant support and guidance through the past few years, both personally and academically. A special thanks for the folks at the Kirsten Wind Tunnel: Cara, Riley, Miguel, and crew, for their work and answering many questions.

All of these people have made this work and thesis possible.

Contents

List of Figures

List of Tables

Nomenclature

Abbreviations

BMC Balance Moment Center

CAD Computer Aided Design

CFD Computational Fluid Dynamic

FPA Fork and Pitch Arm

KWT Kirsten Wind Tunnel

MMC Model Moment Center

MSS Model Support System

OML Outer Mold Line

PDEs Partial Differential Equations

psf Pound-force per square foot

SCALOS Supersonic Configurations at Low Speeds

T&I Tare & Interference

UWAA University of Washington William E. Boeing Department of Aeronautics and Astronautics

VDI Virtual Desktop Interface

W15 2015 Wing

Variables

α Angle of attack

β Sideslip angle

Ψ Yaw Angle

C_D Coefficient of Drag

C_L Coefficient of Lift

C_M Coefficient of Pitching Moment

C_N Coefficient of Yawing Moment

C_R Coefficient of Rolling Moment

C_Y Coefficient of Side Force

$C_{D_{min}}$ Drag Coefficient minimum (of drag polar)

C_{D_o} Drag Coefficient at 0 lift

C_{L_W} Wing Lift Coefficient

Re	Reynolds number
S_{ref}	Wing Reference Area
D	Drag Force
L	Lift Force
PM	Pitching Moment
RM	Rolling Moment
SF	Side Force
y+	Distance from wall normalized by the viscous length scale
YM	Yawing Moment

Chapter 1

Introduction

1.1 Background

The work presented in this thesis is part of the NASA-funded Supersonic Configurations at Low Speeds (SCALOS) project, of which the main goal is to study representative long-range supersonic configurations and variations from the applied aerodynamics perspective. The SCALOS project is built upon the basis of years of undergraduate capstone design work and Kirsten Wind Tunnel (KWT) data [4], most of which was conducted using one of the KWT's fork-styled model mounts. Reasons for originally specifying the fork type mount for the core model design were 3-fold;

1. the thin supports were anticipated to minimize flow interference on the surface of the model,

2. the available fork mount allowed testing of wing-alone cases with no additional fairings or body components,

3. KWT had an existing standard fork-mount correction (including model interference on the fork), historically based on a generic calibration wing model.

While these types of mounts are perfectly acceptable to use, a proper Tare and Interference (T&I) test must be performed to accurately account for the forces and moments of the support imposed on the model in the wind tunnel and the effects of the model support system on the **measured** forces and moments. That is, the presence of the support system (and walls) affects the flow around the model and makes it different from what it would be in free flight of the model. The balance (the force and moment measuring system) in many wind tunnel tests is not mounted inside the model, connecting the model to its support structure, to measure forces of moments on the model itself. The balance may be in a part of the support system that is removed from the model. The balance, therefore, would measure forces and moments on both the model and the support system together. The challenge in such a case is to obtain data for the aerodynamic forces and moments on the model in free flight, correcting the measured data for the effect of aerodynamic interference and walls and separating the measured data into contributions from the model itself and contributions from the forces and moments on the support structure. The effects described above are known as Tare & Interference (T&I) effects. The corrections developed to account for them are known as T&I corrections. While KWT's standard fork "T&I" corrections were satisfactory for most purposes, use of the SCALOS data for absolute level data (e.g. comparison with CFD) raised concerns about potential bias introduced by differences between the support interference of the rectangular calibration wing versus the larger delta type wings of the SCALOS study.

A traditional T&I wind tunnel test involves mounting the test model upright and upside down and using an image fairing / support, shown in Figure 1.1. Figure 1.2, shows the mounting settings necessary to perform the test. The process is explained in [2]. In addition to runs with the model mounted on the support system upright and upside down, the tests are repeated with the addition of the mirror support system. In essence, the addition of an image support fairing practically doubles the aerodynamic interference effect of the fairing on the model. The addition of an image fork or strut (depending on whether the model is supported on a strut or a fork) practically (approximately) doubles the interference effects of the force / strut. And when the image fork or strut is attached to the upper side of the model (whether it is inverted or not) the loads contributions of the fork/strut itself double approximately as measure by the outside balance. The effects of the support system fairing and the support fork/strut can now be identified and later subtracted from raw measurements in tests of the model on its strut/fork to yield the loads on the model itself due to the model itself.

The preceding capstone design wind tunnel models were not designed to be mounted upside down for T&I tests. The assumption was that T&I corrections for the fork mount and the pylon that covers part of it that were developed years ago at the KWT were appropriate and adequate for the educational purposes of

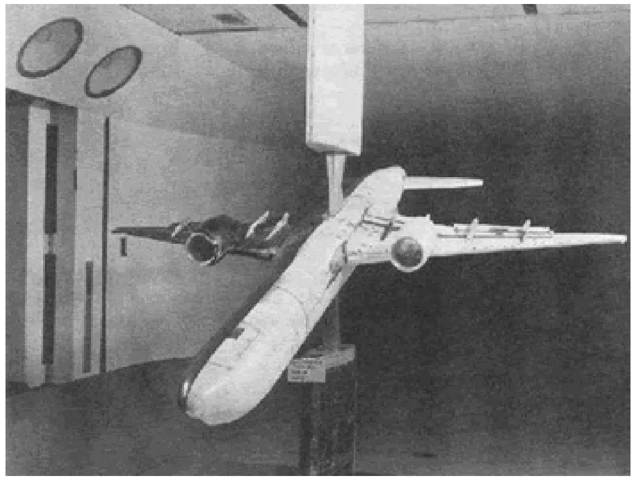

Figure 1.1: Image of Single Strut & Fairing With Boeing 757 Model [1]

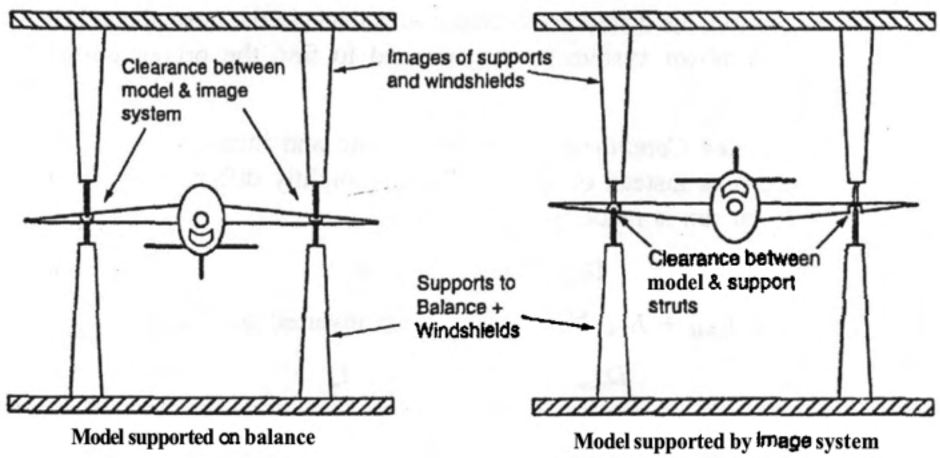

Figure 1.2: Mirror Image Method for Determining Support Effects on a Model[2]

the capstone design projects. But some anomalies in the data from recent tests and a careful examination of how the corrections for the fork mount were developed led to the conclusion that the establishment of proper correction for the SCALOS tests had to be redone because of the very different geometry of the configurations involved relative to what was used at the KWT to develop its standard corrections.

Without accurate wind tunnel data on the fork model mount, corrected for fork/faring interference and loads contributions, simulating the mount using Computational Fluid Dynamics (CFD) became the next-best solution approach of choice. The practice of using CFD for wind tunnel corrections has become more widespread. CFD modeling makes possible the simulation of a model that "floats" in the test section (that is, no supports are present), a model that is supported by the mounting system used, the effects of test section walls or no walls can be investigated. CFD simulations allow the planned and careful isolation of determining parameters, testing their effects methodically.

While several computational tools are available to assess the effect of the fork mount and faring on a representative SCALOS model (including aerodynamic panel methods and handbook estimates for the geometries involved) , Reynolds Averaged Navier Stokes (RANS) CFD was selected because of the accuracy needs regarding skin friction drag and the highly separated flow nature of cranked delta wings of the SCALOS project at high angles of attack. An earlier paper published by the author and his SCALOS colleagues highlights the inabilities of linear codes (vortex lattice and panel codes) to capture the longitudinal pitching moment characteristic as well as drag for select SCALOS configuration [5]. Therefore, accurate corrections at high angles of attack with highly non-linear flow required the use of RANS-CFD coupled with experimental data from the KWT. Alternatively, the ability of CFD, when carefully used, to provide quality incremental data has already been established by the aerodynamics CFD community. Accurate increments are, therefore, attainable because of the focus in increments. This tends to work well with CFD simulations that can suffer from certain inaccuracies because errors from simulations tend to cancel[6]. In other words, simulations of increments can be accurate and useful even when the simulations themselves may slightly miss.

For the analysis of incremental differences, where P, for example, is some output of the simulation and e is a simulation error term,

$$\Delta P = (P + e)_2 - (P + e)_1 = (P_2 - P_1) + e_2 - e_1 = \Delta P_{actual} + error \tag{1.1}$$

The errors, when multiple simulations are run, tend to cancel out, leading to a smaller error term [6],

$$\Delta P = \Delta P_{actual} + error \tag{1.2}$$

Many others in the applied aerodynamic field have assessed and improved wind tunnel corrections using CFD. See, for example, [7–10]. The CFD-based approach based on RANS simulations was adopted in this work.

1.2 Approach and Objectives

The approach used to develop the CFD-based corrections is described in this section. Details of the various simulations and tests will be discussed in subsequent sections.

1.2.1 The 2020 Disk Tests

In a first series of tests dedicated to this task, a KWT test was carried out (designated UW 9733) to survey the forces and moments on the fork 14-H and pitch arm 7-2 of the model support system - MSS- (the ones used for SCALOS tests) during the summer of 2020. A thin circular disk 24" in diameter was fabricated to be mounted on the MSS to perform yaw corrections tests, as the disk was taken to be representative of the flat bottoms of the SCALOS wings. It was assumed that the drag of the disk would be simple to calculate using classic skin friction equations coupled with a form factor correction, that the lift and moments generated by the disk at zero alpha would be zero, and the drag of the disk would be invariant with model yaw. It was believed that the yaw-only T&I of the disk should show similar trends to the fork on the calibration wing at zero alpha over small yaw angles. The disk data would help calibrate the ability of the CFD to model the trends of the end-plated fork itself in yaw. The rounded edge geometry chosen for the 1% thick disk and small blisters covering the mount fittings caused unexpected pressure drag on the disk, making it impossible to simply estimate the disk's drag by handbook flat plate friction values alone. Published sources of excrescence and disk drag test data were used, together with incremental CFD, to find the effective skin friction form factor of the disk as-tested. The disk helped understand the zero-lift / yaw-only T&I of the fork mount using a simple geometry. Added data was needed to understand the lift-dependent variation of T&I for SCALOS's large delta wings.

1.2.2 FPA Correction Calculation Approach

The first step of creating new corrections using CFD was to validate the simulations and the correction calculation using the KWT's existing corrections. The latest corrections for Fork 14-H were created using experimental data from the KWT and by the KWT staff in 1989 and outlined in UWAL Report 397-F [3]. The process used a straight rectangular wing, with NACA 0015 airfoils to calculate both lift and yaw corrections. This wing is commonly referred to as the "NACA wing", and will be named this way in this paper. Two cases of this wing were modeled and simulated to calculate the CFD derived correction:

1. NACA wing in freestream flight conditions

2. NACA wing mounted on the MSS

The fork and pitch arm corrections simply equal:

$$\text{(FPA Correction)} = \text{(NACA wing on MSS)} - \text{(NACA wing freestream)} \tag{1.3}$$

The simulations were initially carried out using relatively coarse meshes and assuming incompressible flow. While the yaw corrections correlated decently with the established KWT corrections, the lift corrections did not. The move to finer CFD meshes and compressible flow led to overall good correlation of CFD to KWT experimental corrections, validating the simulations and correction calculation approach.

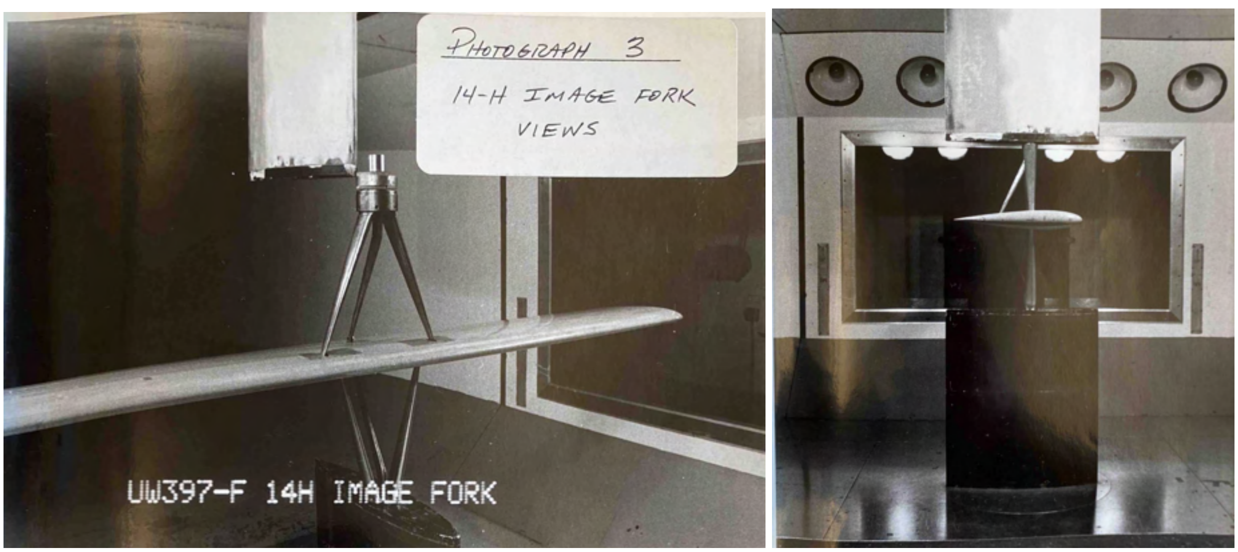

Figure 1.3: NACA Wing Tare & Interference Test in the KWT
[3]

Additional efforts to study the effects of the fork mount by CFD included simulating the isolated FPA (fork and pitch arm) with no model mounted on it and with pin fairings and the FPA with the disk mounted to compare to data collected when testing these two cases in test UW 9733.

(a) MSS and Pin Fairings

(b) MSS and Disk

Figure 1.4: Test Bodies Mounted on the Model Support System in the KWT

1.2.3 Historic KWT Disk and Rectangular Wing Tests on the Fork Support

During the process of recreating and validating these corrections with CFD, it was discovered that in 1956 the yaw corrections for Fork 14-H were evaluated through testing at the KWT using a flat circular disk with tapered trailing edges. The yaw corrections created by the KWT with the disk turned out to be significantly different in two of the moment corrections than those created with the rectangular wing. This has instigated revisiting other established KWT wind tunnel corrections that can be evaluated by CFD: wall and blockage corrections.

1.2.4 Wall Effects

In the work described here blockage and wall corrections were also analyzed for the sake of creating a complete CFD derived correction to KWT uncorrected data. Similarly, two sets of CFD simulations were run using a representative double-delta wing, originally modeled in 2015 and tested in 2015:

1. Wing alone in freestream

2. Wing alone in KWT test section

The same approach applies, the calculation yielding the incremental wall correction is;

$$\text{(Wall Correction)} = \text{(Wing in test section)} - \text{(Wing in freestream)} \tag{1.4}$$

The walls of the test section were modeled using a slip condition. Modeling no boundary layer on the wall simplifies the problem while retaining the majority of the wall effects and drastically reduces the mesh and computation cost.

Adding these two corrections (the support effects incremental correction and the wall effects incremental correction) together yields the total correction from KWT experimental data to freestream conditions. It is assumed by this analysis that the MSS has negligible effect on the wall and blockage effects. The accuracy of these obtained corrections is analyzed in the following chapters and the at the conclusion of this thesis the overall CFD-derived corrections are compared to the complete "standard" KWT corrections performed by the KWT as a final step of assessing which corrections to use for best WT test results.

1.2.5 Nacelle Internal Drag Correction

For aerodynamic performance testing, it is standard industry practice to remove the "internal drag" of the nacelle duct from the measured aero coefficients. This correction is applied because the internal forces are part of the propulsion flow-path and are accounted as part of "installed thrust". CFD simulations were used to calculate an analytical form factor to equate skin friction on a plate to skin friction inside the nacelles. For this two sets of CFD simulations were run:

1. Nacelle in freestream conditions

2. Nacelle equivalent plate in freestream conditions

The interior surface area and length of the nacelle were measured via CAD and an equivalent area and length flat plate CAD model was produced. Both CAD models were simulated in freestream conditions and the skin friction drag was calculated on the areas of interest in CFD. With the use of textbook skin friction coefficient equations and the derived form factor, the nacelle internal duct drag could now be subtracted from the KWT measured data for the model variations with the hollow nacelles on them at different locations. The computed internal duct forces were subtracted from the model forces and moments as a vector quantity, aligned with the nacelle & nozzle centerline.

1.2.6 Objectives of This Thesis Study

To summarize and conclude this section, the objectives for this thesis are to evaluate and generate corrections for measured KWT data for SCALOS configurations, including :

1. Improvement of the model support corrections and mount interference accounting to minimize any bias in the test results for the SCALOS project cranked-delta wings.

2. Assessment of the KWT blockage and wall corrections corrections and their applicability to the SCALOS configurations

3. Creation of engine nacelle internal drag correction to account for the effects of the core of the flow-through model nacelles

Chapter 2

Experimental Setup

2.1 Kirsten Wind Tunnel

All SCALOS wind tunnel tests were carried out in the Kirsten Wind Tunnel, facility of the University of Washington Aeronautical Laboratories (UWAL) in Seattle. The tunnel has a test section of 12 ft in width by 8 ft in height and by 10 ft in length. It is a low-speed, closed-circuit, dual-return wind tunnel as shown in figure 2.1. The tunnel has two sets of 14' 9" diameter seven-bladed propellers capable of test section speeds up to 200 MPH or 100 psf. The dimensions of the Kirsten Wind Tunnel Test Section are shown in figure 2.2 . The cross sectional area of the test section is 96ft^2 neglecting the chamfered corners or 91.5ft^2 [11].

The raw data from the external balance, which is mounted under the floor of the test section, requires correction for obtaining final force and moment values on the free model. The mechanical interaction of forces and moments in the balance system are corrected using standard correction protocols of the tunnel. Strut tare and interference corrections and weight corrections are then applied. Moments are transferred from balance moment center (BMC) to Model Moment Center (MMC). Corrections for blockage, flow angularity, and wall effects are computed and added to the initial coefficients. The final coefficients are transferred from wind axes to stability axes (see Figures A.1a and A.1b in the appendix for the definition of axes). The order in which corrections are applied can cause differences in the final corrected data; the order in which corrections are applied by the KWT are highlighted in the flow chart in Figure 2.3.

In the plots containing KWT data, several sets of data are presented: uncorrected, "online", and "standard" data. KWT "online data" and "standard data" are the two sets of data the KWT delivers to customers. "Online data" is corrected data missing only the model support corrections. This is done to help customers with almost immediate results during a test for the evaluation of trends, key characteristics, problems, etc., and to expedite data visualization while customers are onsite. "Online data" may also leave out additional correction factors specified by the customer. "Standard data" accounts for every correction listed in Figure 2.3 and is delivered by the KWT to customers after the test is concluded. All of the data and results plotted in this thesis is in wind axes since all KWT corrections are applied in wind axes.

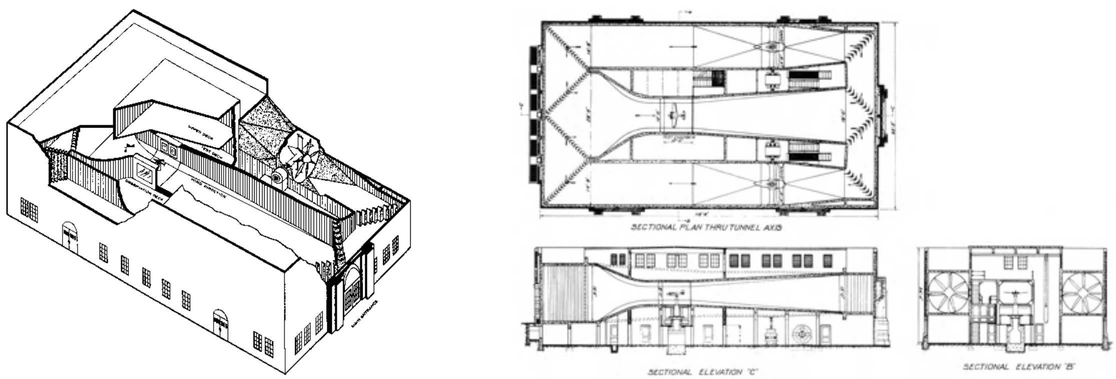

Figure 2.1: The Kirsten Wind Tunnel (KWT) at the University of Washington

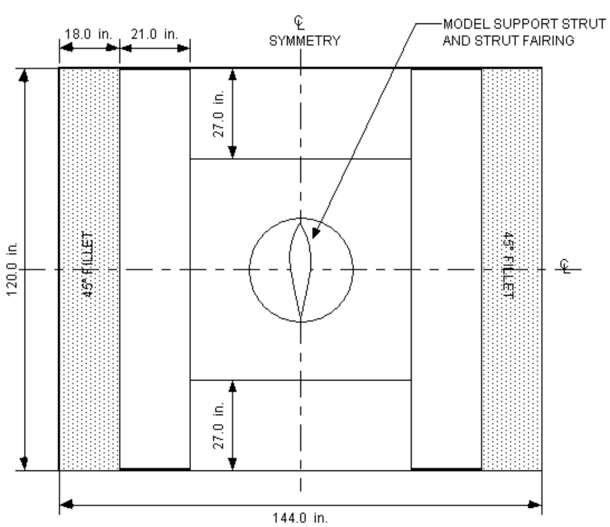

(a) KWT Test Section Dimensions

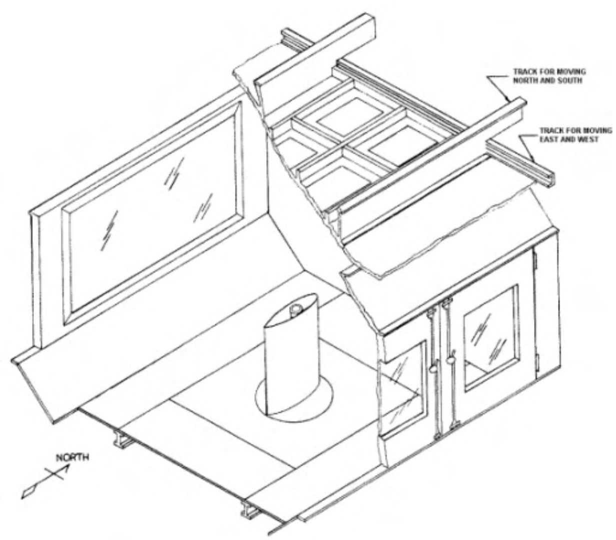

(b) KWT Test Section Cutaway

Figure 2.2: KWT Test Section Drawings

The KWT's standard corrections for the fork-type model support were developed in the 1980s using a calibration model, a high aspect, rectangular wing, 96" in span and 18" in chord, with a symmetric NACA 0015 airfoils. The development of those corrections followed standard wind tunnel correction development procedures using an image system. The configuration that was used for those corrections is much different, however, from the low aspect ratio, swept wings, and overall very slender shapes of the SCALOS project. In addition, over time the Fork 14-H and associated pitch-arm have experienced some wear of the machined-in trip dimples and the surface smoothness, which could have an indeterminate impact on the fork boundary layer state and separation characteristics. This warranted a new drag assessment for the fork mount for the present decade.

The KWT fork support "T&I" corrections are applied in two parts: One correction is based on the lift of the test model and Reynolds number based on freestream dynamic pressure. The other correction is based on the yaw angle and Reynolds number based on freestream dynamic pressure. Those are added together to form the total support correction for any given condition. It is assumed that the two correction components are linearly independent (i.e. minimal cross-coupling of alpha and yaw influences on the fork).

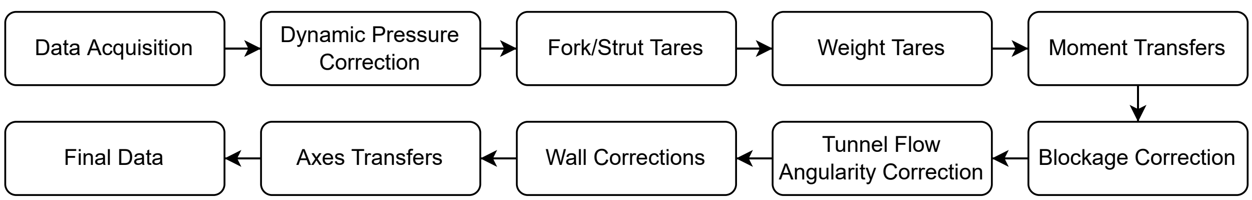

Figure 2.3: KWT Data Reduction Flow Chart

2.2 Models

The Model Support System (MSS) is made up of three main parts: the base fairing, fork 14-H , and pitch arm 7-2 (See: Figure 2.4). The fairing cap is the cover to the base fairing which is installed after the supports are installed and can vary slightly in shape and height, depending on the installation. Fork 14-H is a static two-prong mount on which the model mounts and pivots. The pitch arm is also connected to the model. This arm slides vertically (in the Z-direction) to angle the model in angle of attack. The tripod made up by these two parts rotates as a unit to provide sideslip position. The base of this tripod is housed in the fairing, which extends down to the floor of the test section, but it does not touch the fork and pitch arm . That is, no aerodynamic force from the fairing is transferred to the fork and the strut that connects it to the balance below (i.e. in wind tunnel terminology, the fairing assembly is "non-metric"). The fairing does affect the flow field, though, and this effect should be accounted for (including calibrated test section dynamic pressure and any tunnel "free-stream" flow angularities).

The forces and moments of the fork and pitch arm assembly (FPA) are carried down to the balance and they need to be corrected out of the measured wind tunnel data. Test UW 9733 tested the FPA with pin boss fairings attached to identify the forces and moments on the fork without anything mounted over it, Figure 1.4a. The dimensions for the pin fairings are given in Figure 2.8 and were also modeled and simulated in Star-CCM+ (more - in Section 4.1). It is important to note that the pin fairings (added to provide streamlined fairings covering the irregular end-fittings of the fork) do not have trip dots. Figure 2.4 shows the MSS in the KWT with its parts (fork, pitch Arm, fairing, etc.) defined.

The pitch arm and fairing cap CAD models were obtained from the KWT but no CAD model of fork 14-H existed so a CAD model was created with the sketch provided by the KWT staff, figure 2.5b. Some small simplifications were made to the CAD model for the sake of simplifying the CFD workflow such as removing open-air cavities in the model and not modeling the mounting pins since the pins are inside the model mounted upon it.

The disk, created to investigate the end-plate effect of models on the fork itself and the variation of basic fork correction with yaw, is is 24" in diameter, 0.25" thick (disk t/c 1%), and has 'blister' fairings which cover the connection junctions to the MSS since the disk is so thin. Figure 1.4b shows the disk mounted to the MSS in the wind tunnel. The disk has trip dots 0.75" from the leading edge which cover 170 degrees of the leading edge. The disk design was intended to mimic the flat bottoms of the SCALOS wings, provide, by itself, no lift, induce the least amount of drag and interference, and have identical forces/moments at any sideslip angle. The intention of this was to isolate the forces and moments of the FPA as much as possible. Additionally, the drag on the disk was assumed to be simple to calculate using turbulent skin friction equations and a form factor. In practice the aerodynamics of this disk proved to be more complex than anticipated. More on this - in Section 4.4.

The wing designed by the capstone class of 2015 (W15) served as the representative wing for SCALOS project and the wind tunnel corrections calculated in this thesis. The inboard wing in-spar region and integral

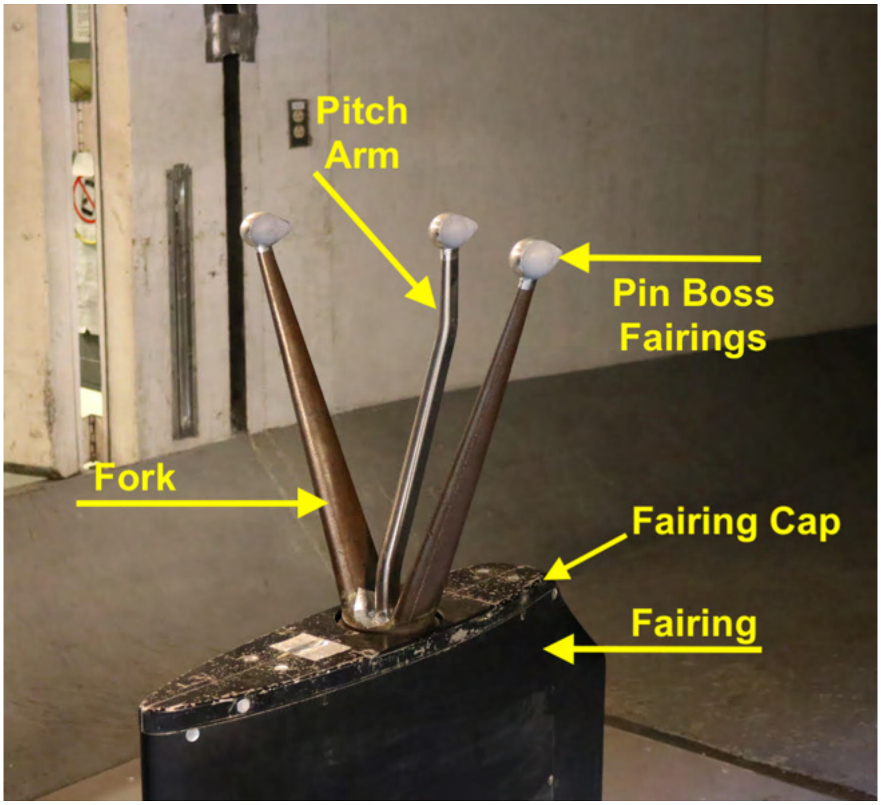

Figure 2.4: KWT Model Support Definitions

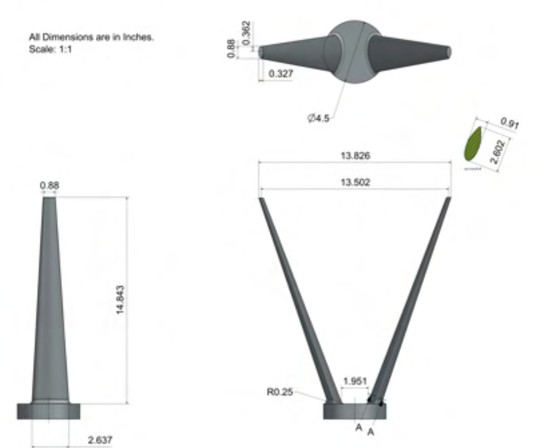

(a) CAD Dimensions of the 14-H Fork

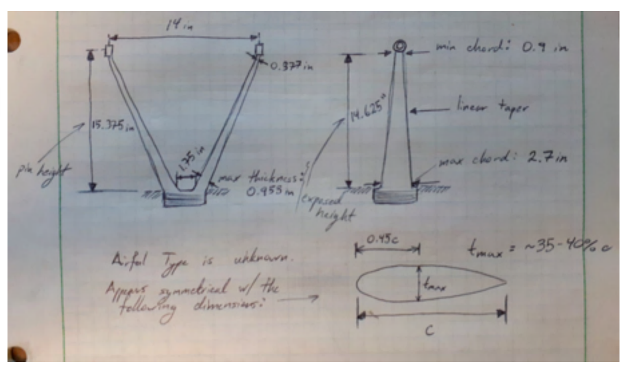

(b) Measured Dimensions of the 14-H Fork

Figure 2.5: Dimensions of the 14-H Fork

carry-through center-body of this model hardware is common with the 2013 UW undergraduate Capstone class design. This modular "core" model has been used as the basis of multiple test configurations for

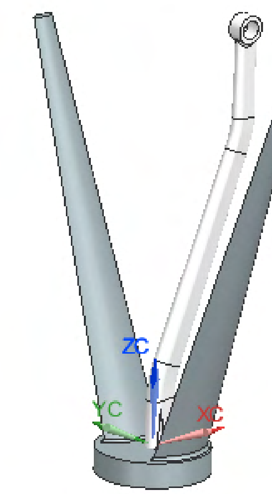

(a) CAD Model of Fork 14-H (grey) and Pitch Arm (white)

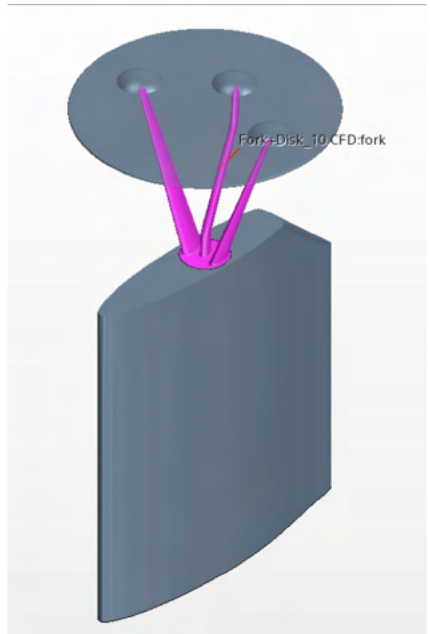

(b) Fork and Pitch Arm Surfaces in Star-CCM+

Figure 2.6: Fork and Pitch Arm CAD Definitions

subsequent UW capstone efforts and the SCALOS investigation wings. The basic airfoil used was a NACA 66-204-45 section of 4% thickness to chord ratio (similar to fighter aircraft wings, slightly thicker than the 2-3% t/c of most supersonic transport wings). This choice simplified construction of the research UAV's used for several related UW projects based on these wind tunnel models.

The wing planform, as it is mounted, has a 2 degree angle of incidence. This provided the highest lift to drag ratio and thus highest efficiency across a range of lift coefficients [12]. Despite the thicker airfoils, the wing and the family of configurations built based on it, were deemed adequate for aerodynamic studies of the effects of planform variations at low speeds, with much attention to the flow in the leading edge area and the lines along which separation develops and vortices are shed.

The 2015 wing is the most "middle of the road" planform, among the many wing planforms tested at the UW over the years, in terms of span and sweep of the SCALOS planforms and thus serves as a representative planform, Figure 2.9. Figure 2.11 shows key dimensions of W15 compared to W17 and W20, two wings that were also extensively tested for the SCALOS project. The outboard section of the wing is interchangeable. Different configurations could be installed and tested, making the wing well suited for iterative changes from one capstone project to another. The fork support mount point (the BMC) is 26.378" back from the leading

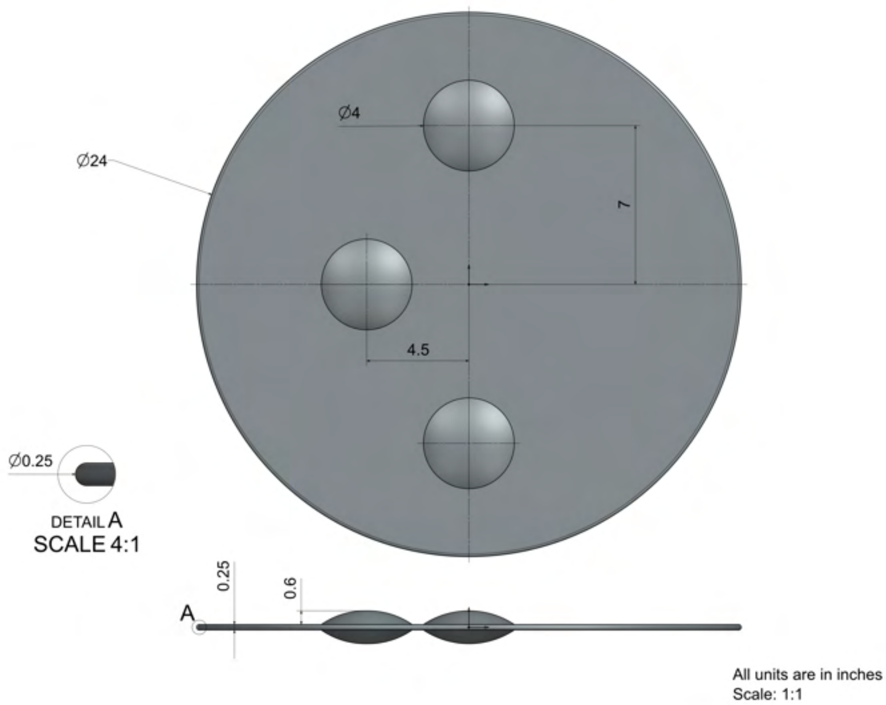

Figure 2.7: Dimensions of the Disk

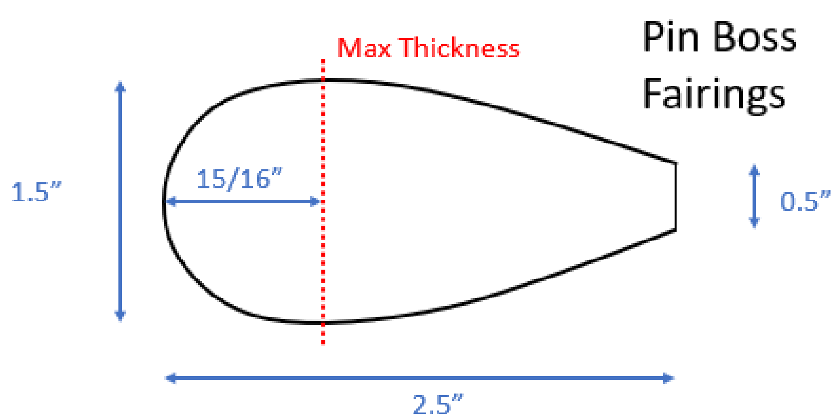

Figure 2.8: Dimensions of the Pin Boss Fairings

point of W15. The 25% Mean Aerodynamic Center (MAC) used as the center of gravity point (MMC) is 4.261" aft from the BMC (+x-direction) and 1" down (z-direction).

It should be noted that the angle of attack alignment for W15 was historically done using a custom-built alignment spine, a flat surface used to calibrate zero angle of attack. However, this alignment spine was lost several years ago. Therefore, alignment was done using the wing-fuselage connector spine. This spine was presumed to be a sufficient replacement. The spine is pictured in Figure 2.10.

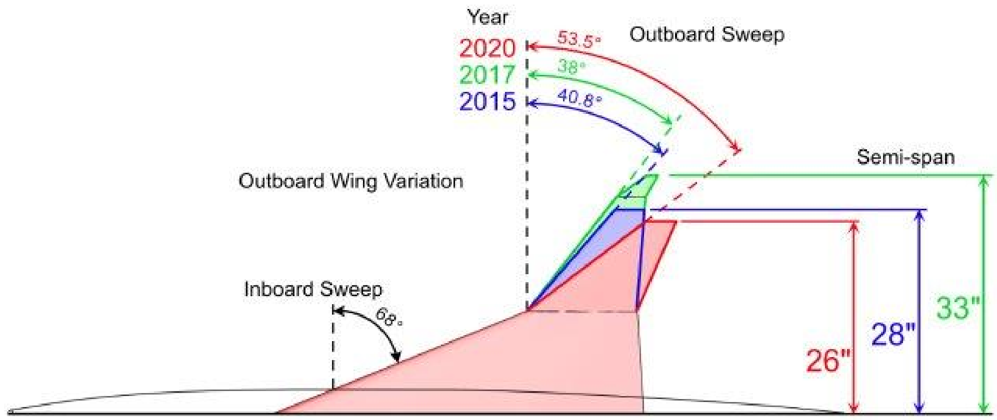

Figure 2.9: Comparison of W15, W17, W20

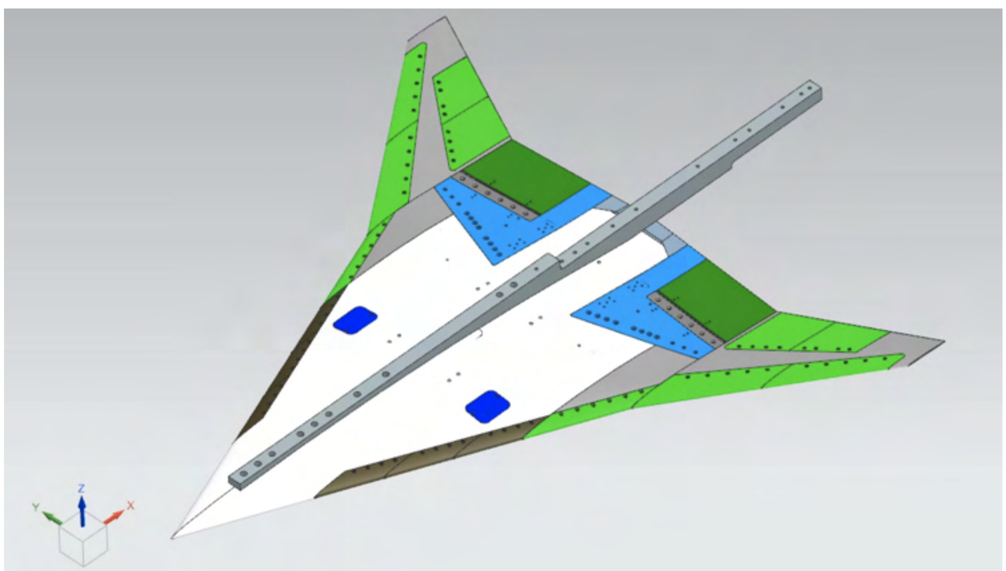

Figure 2.10: W15 CAD Model with Fuselage Mounting Spine used for aoa alignment

Table 2.1: Characteristic Dimensions of the 2015 Wing

MAC	b	S_{ref}
26.0656"	55.93"	8.296 ft^2

The wind tunnel tests carried out for the SCALOS project were conducted at the KWT at multiple dynamic pressures, sideslip angles (β), and angles of attack (α). Table 2.2 lists the nominal dynamic pressure

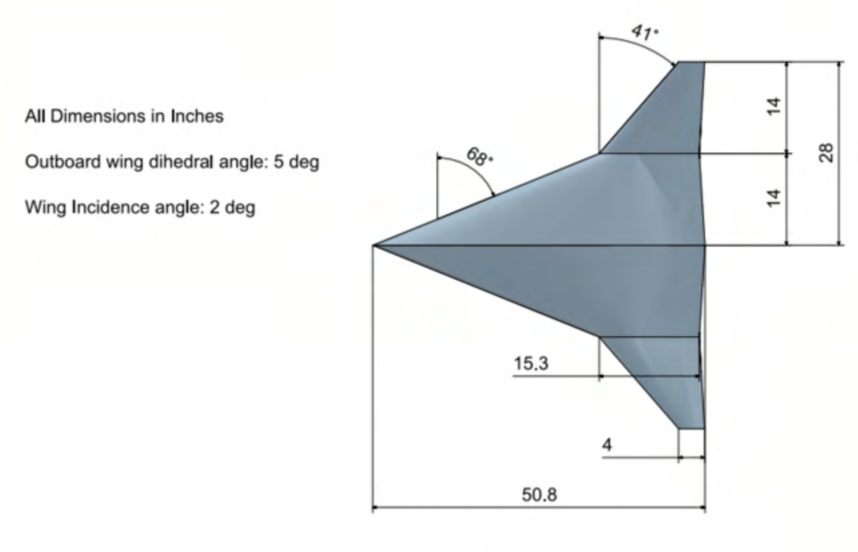

Figure 2.11: Dimensions of the 2015 Wing

and the corresponding Reynolds numbers (Re) based on the 2020 Mean Aerodynamic Chord (MAC) length of 26.0656" (identical to W15) and sea level conditions.

Table 2.2: Dynamic Pressures and Reynolds Number in the KWT

q (psf)	5	10	20	30	40	80
Re	8.53×10^5	1.20×10^6	1.70×10^6	2.08×10^6	2.39×10^6	3.31×10^6

Figure 2.12: MSS and W15

Chapter 3

Computational Fluid Dynamics

3.1 Background

3.1.1 Software and Computing Platform

Star-CCM+ was the Computational Fluid Dynamics software of choice for the work described here. Star-CCM+ has the complete suite of modules and functions necessary to complete a CFD simulation: mesh, simulation, and post-processing. The graphical user interface is simple, intuitive, and easy to use. The software is capable of simulating large scale turbulent problems, so there are no limiting factors, regarding our work, in using it. It uses one implicit solver and so less theoretical CFD knowledge is necessary for using it. The OpenFOAM code was considered briefly but was not selected because it has no graphical user interface, needs a separate post-processing software, and, compared to the user-friendliness of Star-CCM+, was found to require a steep learning curve.

For the CAD work required, NX the program of choice. This has been the legacy CAD software for capstone design classes in the UWAA department. Aerotec (The company that built the SCALOS wind tunnel models) uses NX and that made the CAD file transfers process between wind tunnel model geometry and CFD meshing seamless. NX is a powerful software that has many features that other software packages do not have that are helpful in cleaning and preparing CAD models for CFD. Furthermore, Star-CCM+ and NX are now both owned by the same company, making a license purchase simpler for the department/College of Engineering.

Some CAD models were available from Aerotec (the manufacturer of capstone models since 2013) and the Kirsten Wind Tunnel. CAD models from Aerotec included all holes and tolerances necessary for machining the parts. They were not OML (Original Outer Mold Line), smooth CAD models. Much time was spent deleting holes, shelves, gaps, etc., and uniting multiple parts into one, smooth, water-tight body in order to be used in Star-CCM+. Star-CCM+ is like any other CFD software regarding CAD flexibility, it needs a water-tight model to run fluid simulations. While Star-CCM+ offers many CAD and mesh altering features and commands to fix broken or complicated CAD, CFD-ready CAD was imported into Star-CCM+ from Siemens NX.

3.1.2 Governing Equations of Fluid Flow

The Navier-Stokes equations, mathematically modeling aerodynamic flows at the range of Reynolds and Mach number at which full-size subsonic and supersonic airplanes operate, are presented below in conservative, differential form [13, 14].

Conservation of Mass

$$\frac{\partial \rho}{\partial t} + \nabla \cdot (\rho \bar{u}) = 0 \tag{3.1}$$

Conservation of Momentum

$$\frac{\partial \rho \bar{u}}{\partial t} + \nabla \cdot (\rho \bar{u} \otimes \bar{u} - \sigma) = 0 \tag{3.2}$$

Conservation of Energy

$$\frac{\partial \rho e}{\partial t} + \nabla \cdot \big[\rho e \bar{u}) + p\bar{u} - \tau \cdot \bar{u} - k\nabla T\big] = 0 \tag{3.3}$$

These equations in 3-dimensions include five partial differential equations and seven unknowns (ρ, u_1, u_2, u_3, e, P, T).

The additional equations necessary for solution are the equation of state and a thermodynamics relation for the energy.

Typically, the ideal gas law is used as the equation of state.

$$P = \rho R T \tag{3.4}$$

The thermodynamic relationship relates energy to to temperature.

$$e = c_v T \tag{3.5}$$

These equations are spatially and temporally discretized and solved in Star-CCM+ (and any equivalent RANS-CFD code). One should note that several simplifications are commonly used to reduce the computational effort.

An list of flow model simplifications are, going from the higher-fidelity / high computational effort to the lower fidelity / lower computational effort:

- No simplifications: Direct Numerical Simulation (DNS)
- Turbulence Model simplifications: Reynolds Averaged Navier Stokes Equations (RANS) and filtered Navier-Stokes Equations (Large Eddy Simulations)
- Inviscid Flow: Euler Equations
- Inviscid and Irrotational Flow: Potential Flow Equations

Different levels of accuracy are associated with the discretization of the equations. Discretization schemes are only accurate to a certain degree, be it second, third or even fourth degree accurate. The discretization is never a "perfect" representation of the partial differential equations (PDEs) due to truncation errors. Because of the the imperfectly-discretized equations, numerical errors propagate and can become ungovernable. The discretization accuracy for both the spatial and temporal parts of the equation must be selected carefully. A high-quality mesh is also necessary for solution convergence and accuracy.

3.1.3 Boundary Conditions and Equations

Boundary conditions and initial conditions used in the simulations were formulated as functions of wind tunnel dynamic pressure (given in pounds-force per square foot (psf)) using the incompressible equation for dynamic pressure and isentropic relations for pressure as a function of velocity [15].

$$u = \sqrt{\frac{2q}{\rho}} * 0.3048 \tag{3.6}$$

$$P = P_{atm}\left[1 + \left(\frac{\gamma - 1}{2}\left(\frac{u}{a}\right)^2\right)\right]^{\frac{-\gamma}{\gamma-1}} \tag{3.7}$$

where $\rho \equiv 0.002377$ slug/ft, $a \equiv 343$ m/s, $\gamma = 1.4$, $P_{atm} = 101325$ Pa. Note the 0.3048 factor in Equation (3.6) is the conversion from ft/s to m/s since q is given as lbf (the way it is used in the wind tunnel to set the flow condition) and the following calculations use SI units. The reference pressure is often measured as a dfifference from one atmosphere in Star-CCM+ and so in that case $P_{ref} = P - P_{atm}$.

3.1.4 Meshing and Physics Models

The selection of structured or unstructured grids is the first decision to make when generating a CFD mesh. Unstructured meshes were used because of the ease in Star-CCM+ of producing high-quality meshes for more complicated geometry.

The mesh modules/types used are:

- Surface remehser
- Polyhedral mesher (Volume)
- Prism Layer Mesher (Volume/Surface interface to capture boundary layer).

The prism layer mesh is a quasi-unstructured mesh extruded exponentially from the surface of the model. This produces exceptionally thin cells that align with the body and capture the boundary layer. All meshes in this thesis target a y+ value of one, a number that generally produces the most accurate results (and is now a standard in the aerospace industry) [16, 17] and a total height equal to the height of the boundary layer at end of the wing. y+ is defined as the distance from the wall normalize by the viscous length scale, Equation (3.12). The following equations are necessary for calculating the wall spacing, i.e. the first cell thickness[18].

$$Re_x = \frac{\rho U_\infty L}{\mu} \tag{3.8}$$

$$C_f = \frac{0.026}{Re_x^{1/7}} \tag{3.9}$$

$$\tau_{wall} = \frac{C_f \rho U_\infty^2}{2} \tag{3.10}$$

$$U_{fric} = \sqrt{\frac{\tau_{wall}}{\rho}} \tag{3.11}$$

$$y^+ = \frac{U_{fric} y}{\nu} \tag{3.12}$$

$$\Delta s = \frac{y^+ \mu}{U_{fric} \rho} \tag{3.13}$$

Equation (3.9) is commonly referred to as the Prandtl one-seventh power law for turbulent flow.

Given the first cell thickness, Δs from Equation (3.13), the necessary equations for building the prism layer mesh in Star-CCM+ are discussed below [16]. The growth ratio, r, (a.k.a. the stretching ratio) was chosen to be 1.3, a choice suggested by the Star-CCM+ External Aerodynamics Best Practices document[16] and the total thickness, t, was calculated using flat plate boundary layer theory, Equation (3.9) evaluated at the length of the MAC. The resulting total thickness of the boundary layer is 13.2 mm so a final total thickness of the prism layer mesh was 18 mm to safely encapsulate the boundary layer within the mesh and account for any prism layer trimming done by the software (done to ensure smooth transition between the prism layer mesh and the volume mesh). The number of prism layers, n, was the unknown solved for, Equation (3.14) [16].

$$n = log_r\left(1 - \frac{t(1-r)}{\Delta s}\right) \tag{3.14}$$

All simulations used the following physics models: time steady, ideal gas, compressible flow, turbulent flow, Spalart-Allmaras turbulence model [19], and all-y+ treatment. The solver is a coupled solver and utilizes the Automatic CFL solution accelerator with default settings. The far-fields were modeled 50x each body's characteristic length away as freestream boundary conditions. Boundary conditions were a freestream boundary specified by Mach number and static pressure, both of which were back-calculated using the KWT's corrected dynamic pressure measurement reading, and a turbulent viscosity ratio of 1. The

Spalart-Allmaras turbulence model was used and turbulence was specified using the turbulent viscosity ratio which was set to one for all simulations[16] . Furthermore, turbulent viscosity ratios of 0.1 and 10 were also tested in one simulation (W15 freestream). No significant difference in force and moment data was apparent.

3.2 Simulation Validation Studies

Before proceeding to the CFD-based research itself, it is important to build confidence in the math model used and the results of the CFD simulations. Three types of studies are presented in this section to validate mesh and physics assumption choices for the W15 - the main subject model for which corrections are applied. Additional validation studies are presented in this thesis to validate certain processes and models. In this section baseline settings are studied.

3.2.1 Mesh Refinement Study

A mesh refinement study was performed on the 2015 wing half model in freestream conditions. Five different meshes were used, four of which target surface mesh generation and the fifth aimed at investigating the effect of using a high y+ approach (roughly y+ = 30) with the prism layer mesh, Table 3.1. Star-CCM+ automatically calculates the wall distance from the meshes and the appropriate wall functions are automatically used [16, 20]. All simulations were modeled in freestream conditions with a spherical freestream boundary 50x the length of the MAC away from the model, Figure 3.3. Models were split in half, lengthwise with a symmetry plane, to reduce computational run time. Figure 3.1 shows the mesh produced from CAD to highlight the necessity to re-mesh, in much more detail, the geometry for CFD purposes. Figure 3.2 shows the re-meshed surface (baseline settings), ready for CFD use. The standard wake refinement setting is shown in Figure 3.4 and the standard prism layer settings are shown in Figures 3.5 and 3.6.

Figures 3.7 to 3.10 show drag, lift, and pitching moment coefficients as well as lift over drag as functions of the angle of attack in free flow for the different meshes used. The CFD results are compared to KWT test results obtained with the W15 wing alone on the fork support - the KWT raw, uncorrected, data, and the KWT data corrected using the standard corrections for the fork support. Note that all CFD discretizations capture the shapes and trends of the curves quite well, with more sensitivity of the CFD curve shape results in the case of the pitching moment, as can be expected. The standard mesh results follow the fine mesh results quite well. Because the focus of this work is on the effects of differences in configurations - that is, on "deltas" - the standard mesh was considered adequate and was used for all subsequent simulations. Figure 3.11 shows the lift and drag value convergence as a function of mesh size for several angles of attack where N is the number of nodes and h is a cell size metric [21]. The lift and drag values are normalized by value with finest mesh.

Mesh Settings	coarse	medium	standard	fine	high y+
Target Surface Size	5 cm	2.5 cm	1 cm	0.5 cm	1 cm
Minimum Surface Size	0.5 mm	0.25 mm	0.1 mm	0.05 mm	0.1 mm
Surface Growth Rate	1.3	1.2	1.1	1.05	1.1
Wake Isotropic Size (max size)	50 cm	25 cm	10 cm	5 cm	10 cm
Number of Prism Layers	25	25	25	35	6
Total Number of Volume Cells	2.09M	3.98M	8.22M	12.34M	1.21M

Table 3.1: W15 Mesh Settings for Mesh Refinement Study

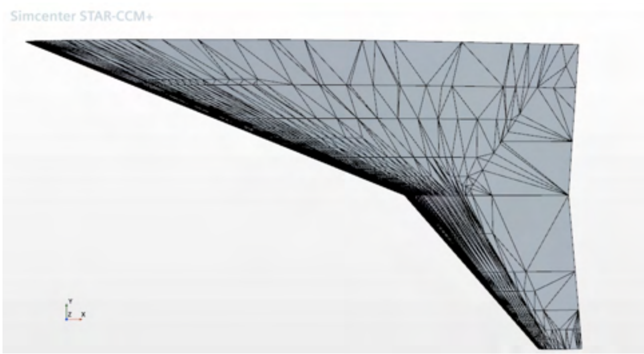

Figure 3.1: W15 CAD Mesh

Figure 3.2: W15 CFD Surface Mesh

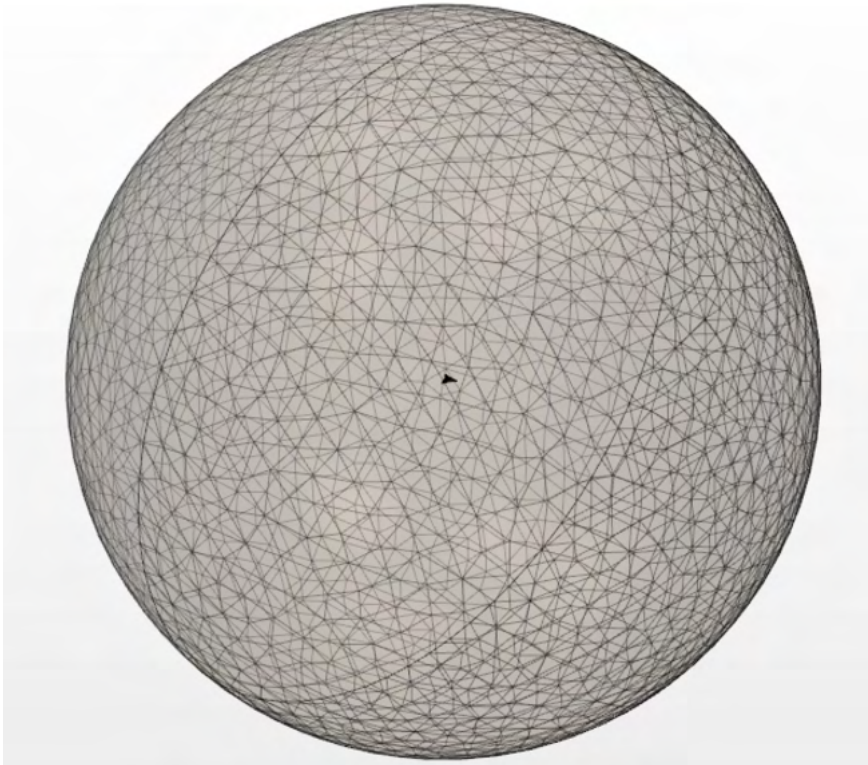

Figure 3.3: W15 Flow Domain

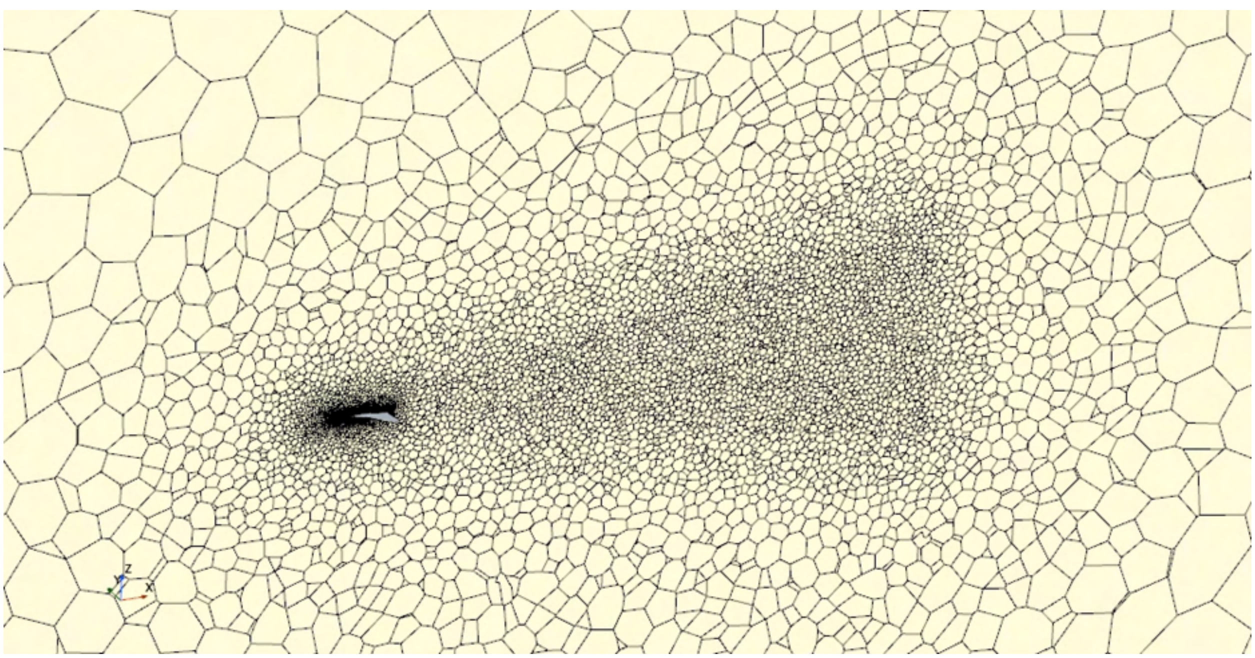

Figure 3.4: W15 Wake Volume Mesh Refinement

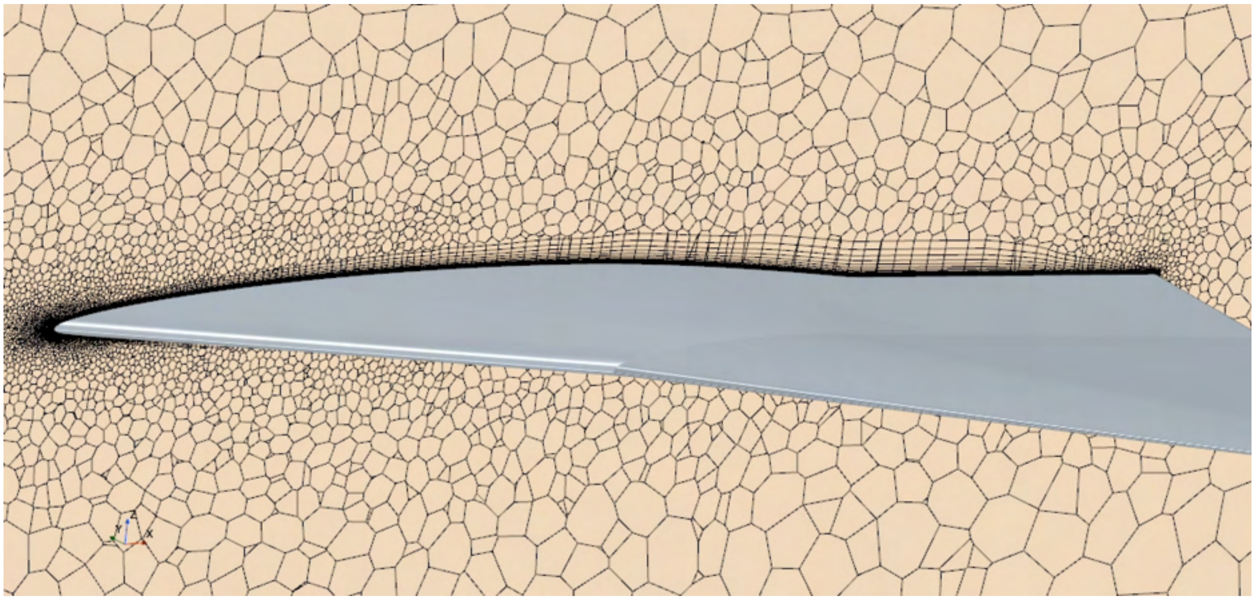

Figure 3.5: W15 Prism Layer and Volume Mesh

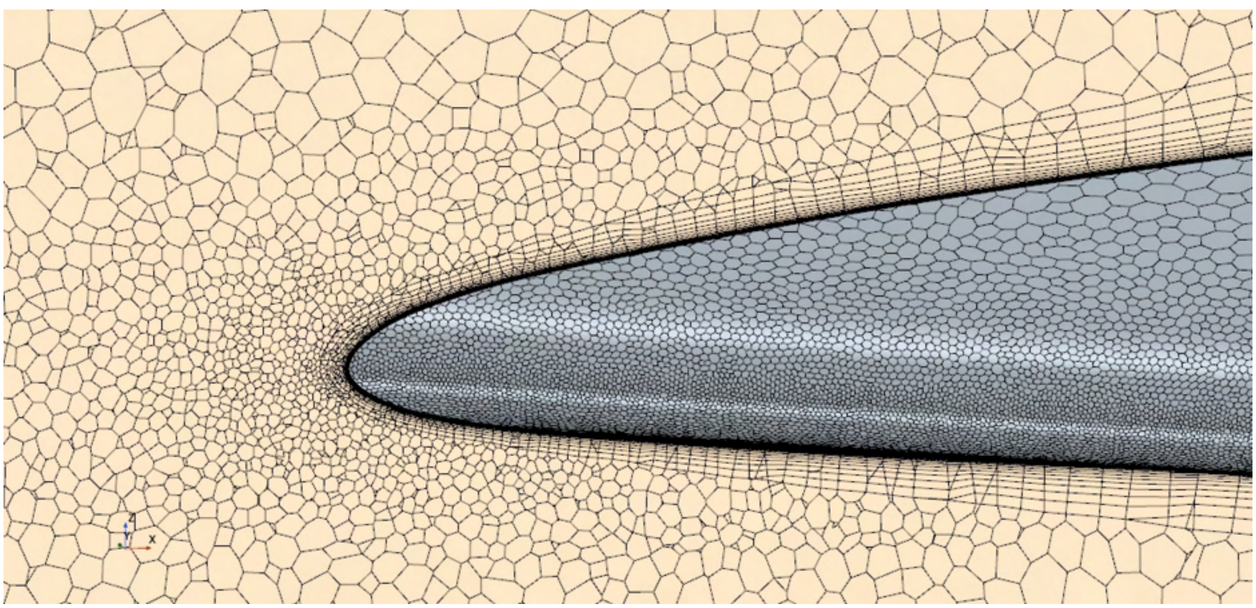

Figure 3.6: W15 Leading Edge Prism Layer and Volume Mesh

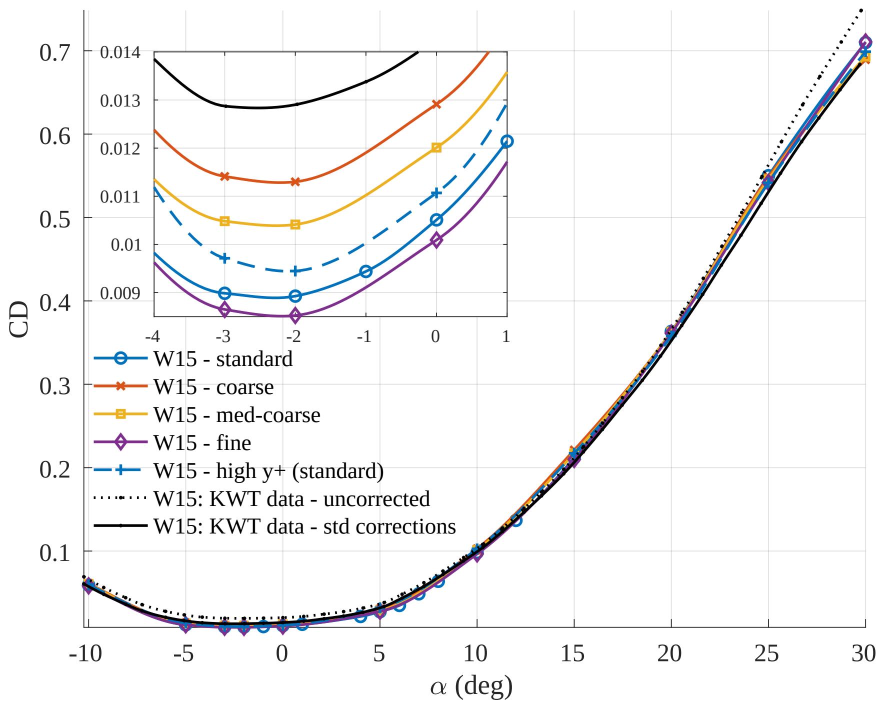

Figure 3.7: W15 Drag Polar for Various Meshes

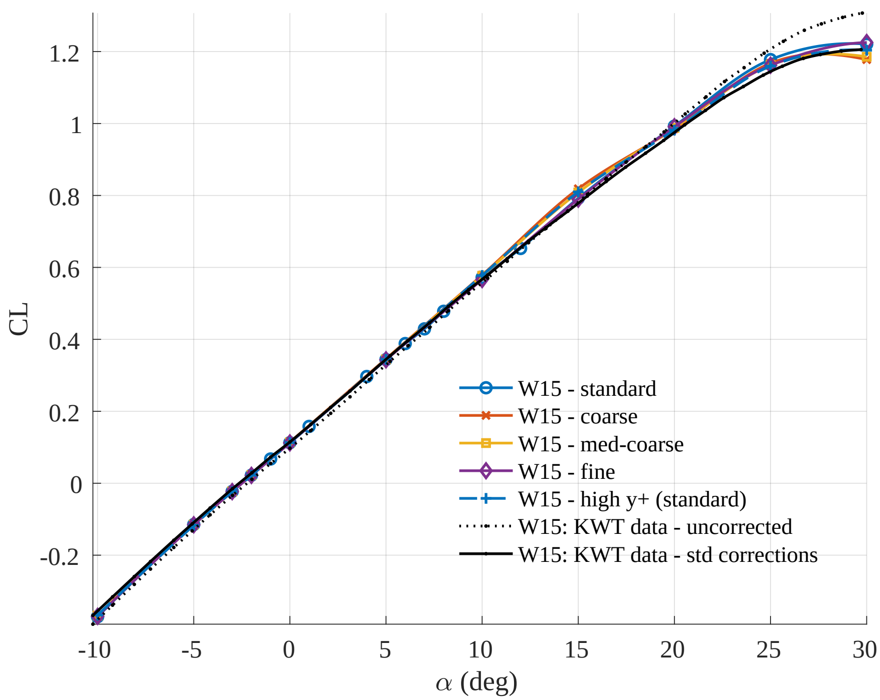

Figure 3.8: W15 Lift Curve for Various Meshes

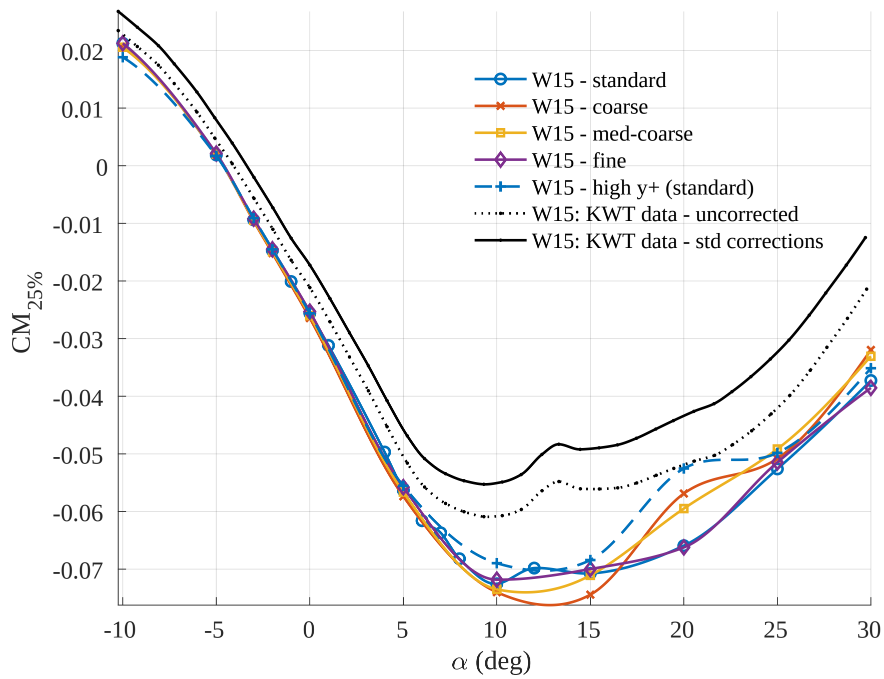

Figure 3.9: W15 Pitching Moment for Various Meshes

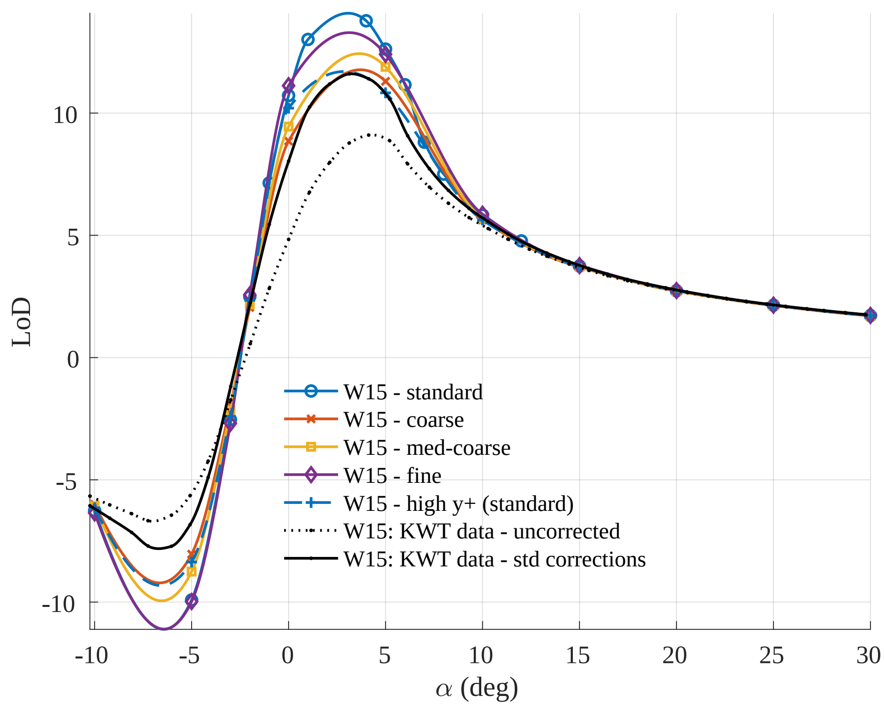

Figure 3.10: W15 Lift to Drag ratio for Various Meshes

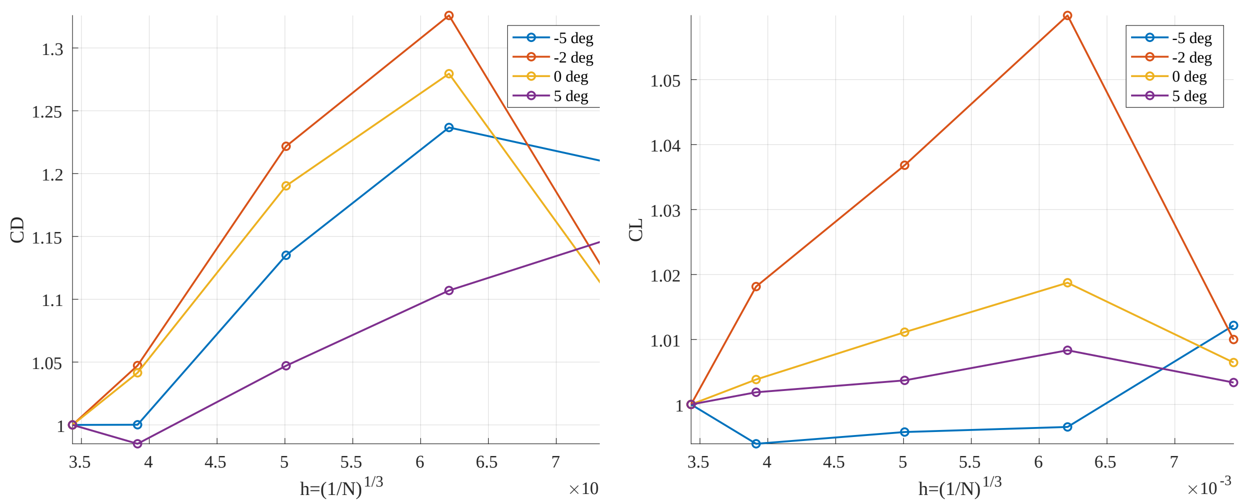

(a) Effect of Mesh Size on Drag

(b) Effect of Mesh Size on Drag

Figure 3.11: Effects of Mesh Size on Lift and Drag

3.2.2 Studying the Effects of Physics Modeling Inputs

An earlier study reported the results of investigating the accuracy of various flow assumptions using various CFD software packages [5], all done using the standard mesh settings from Section 3.2.1.

Figures 3.12 to 3.14 show the inability of the models based on the inviscid assumption to capture the flow phenomena post vortex breakdown. The incompressibility assumption, while relatively resulting in a reasonably accurate shape, still lacks accuracy point by point. Using a compressible flow model yields the best data. It's also noteworthy that the Star-CCM+ data closely follows the CFD data from AD-Flow, a University of Michigan's flow solver which used a structured grid. This demonstrates builds confidence in the adequacy of the Star-CCM+ capability used for the results reported here.

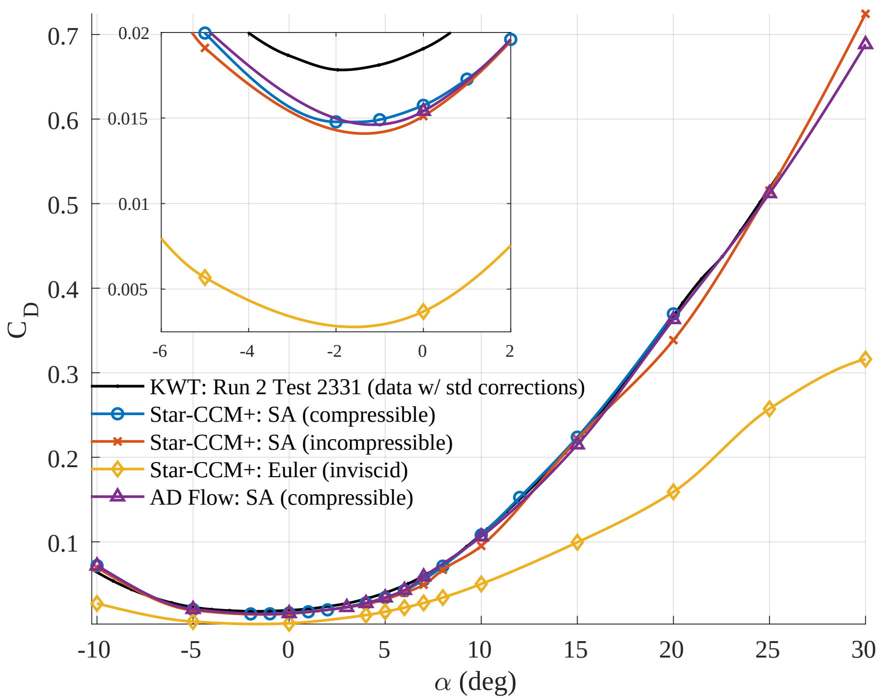

Figure 3.12: Star-CCM+ Physics Study - Drag

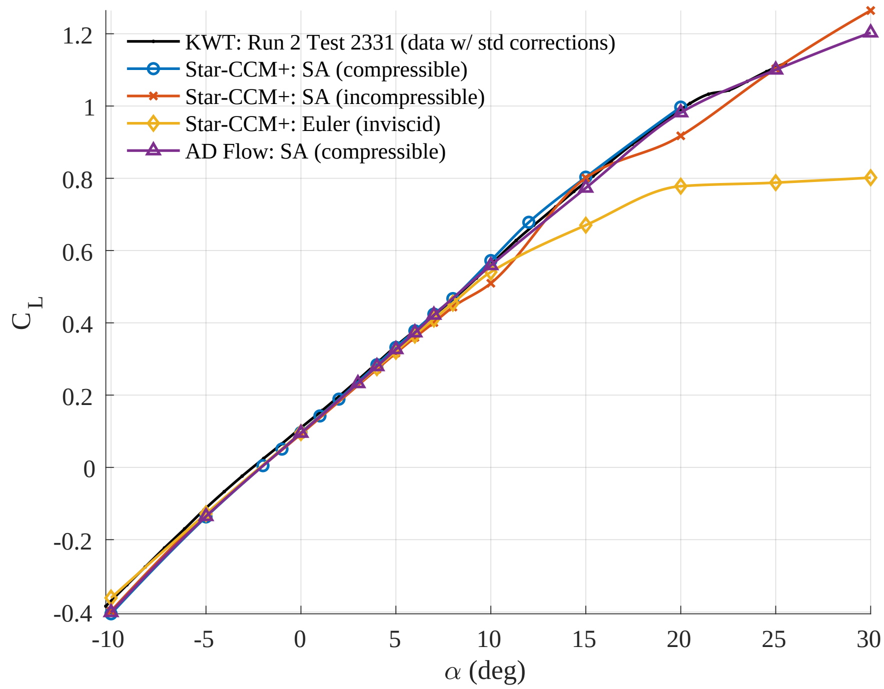

Figure 3.13: Star-CCM+ Physics Study - Lift

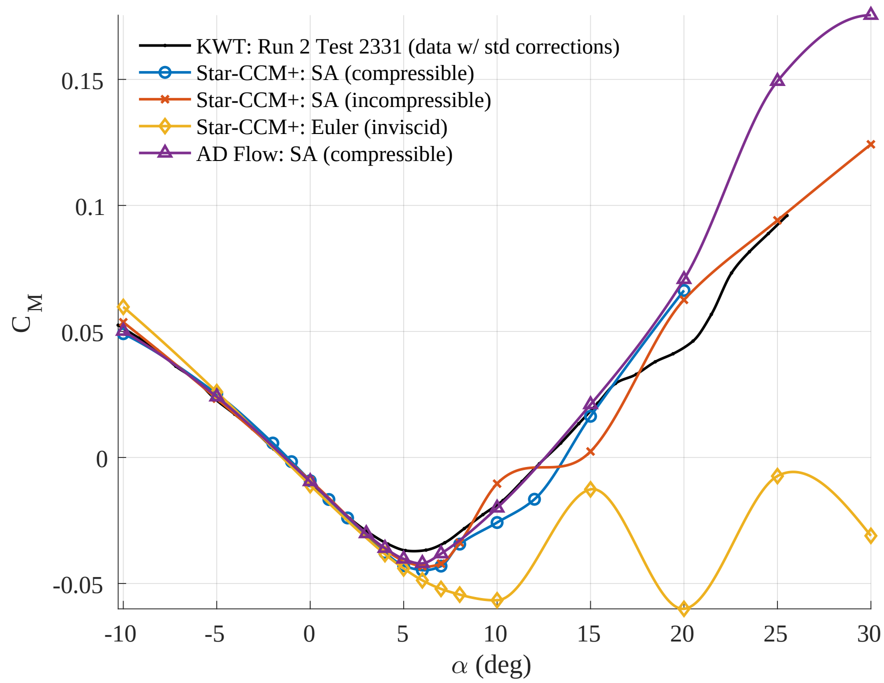

Figure 3.14: Star-CCM+ Physics Study - Pitching Moment

3.2.3 Flow Visualization

Overall, the Star-CCM+ CFD simulations show satisfactory vortex flow skin friction agreement with the KWT experimental flow visualization photos at all angles of attack pictured, Figures 3.15 to 3.18. The thin grey tubes are streamlines created at the vortex cores calculated by Star-CCM+ and are shown to help visualize the flow off the surface of the wing. Dashed black lines are overlaid onto the CFD images to highlight the areas of high shear stress gradients corresponding to the lines observed in the KWT experiments formed by the accumulation of fluorescent dye. Star-CCM+ results show early separation on the outboard wing at each angle of attack case analyzed - a similar result observed from Ito et al.[7]. This also builds confidence in the simulation accuracy.

The differences between the CFD simulations and the KWT experimental flow visualization (and the data in Figure 3.9) may be attributed to two factors: One: the CFD prematurely models the vortex breakdown of the wing; and Two: the walls and boundary layers of the KWT test section cause delayed breakdown of the vortices either because of flow angularity or dynamic pressure differences that is not perfectly corrected in the math models. The first factor is most likely to be the dominant one, considering that the Spalart-Allmaras turbulence model is a simplification of the Navier-Stokes equations (which are approximation of true physics).

Even though the exact flow field predictions (absolute levels, absolute flow vis.) don't match perfectly, so long as the CFD looks like it is capturing the trends (flow and force/moment) then the increments between CFD runs for configurations or alpha changes are good. If increments are good, then CFD forms a valid basis for corrections. Using CFD for corrections in this manner should be close to the same level of uncertainty (or less) than corrections that are experimentally developed in the tunnel, and save considerable setup cost and test time. Certainly better than ignoring corrections and a good check on (and hopefully improvement over) classical handbook methods or old-school Panel Method low-order CFD used 25 years ago. Additionally, CFD helps separate out the overlapping effects of corrections, interference, fork vs pylon/strut contributions, vs wall effects, etc.

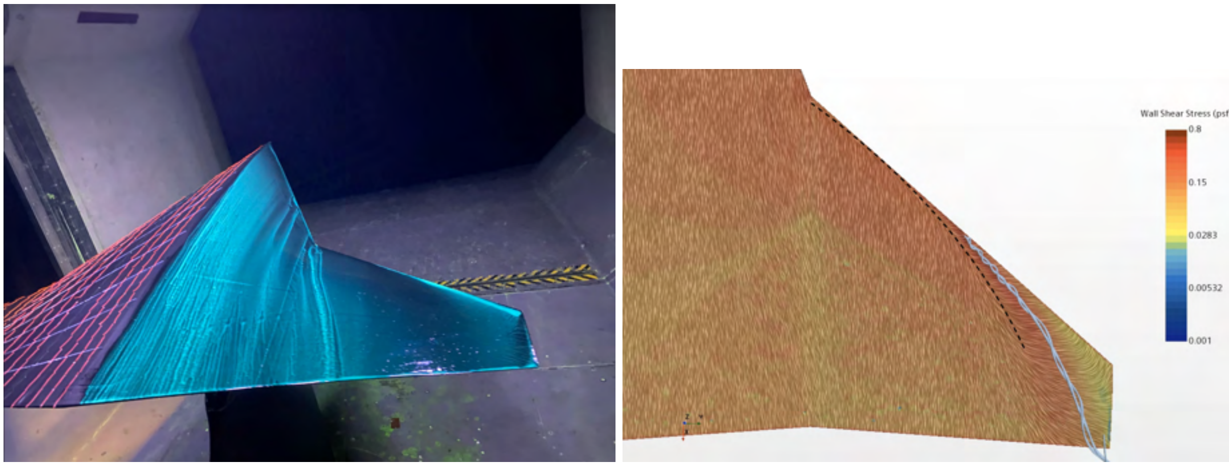

Figure 3.15: Comparison of KWT to CFD Skin Friction Visualization at $\alpha = 5^o$

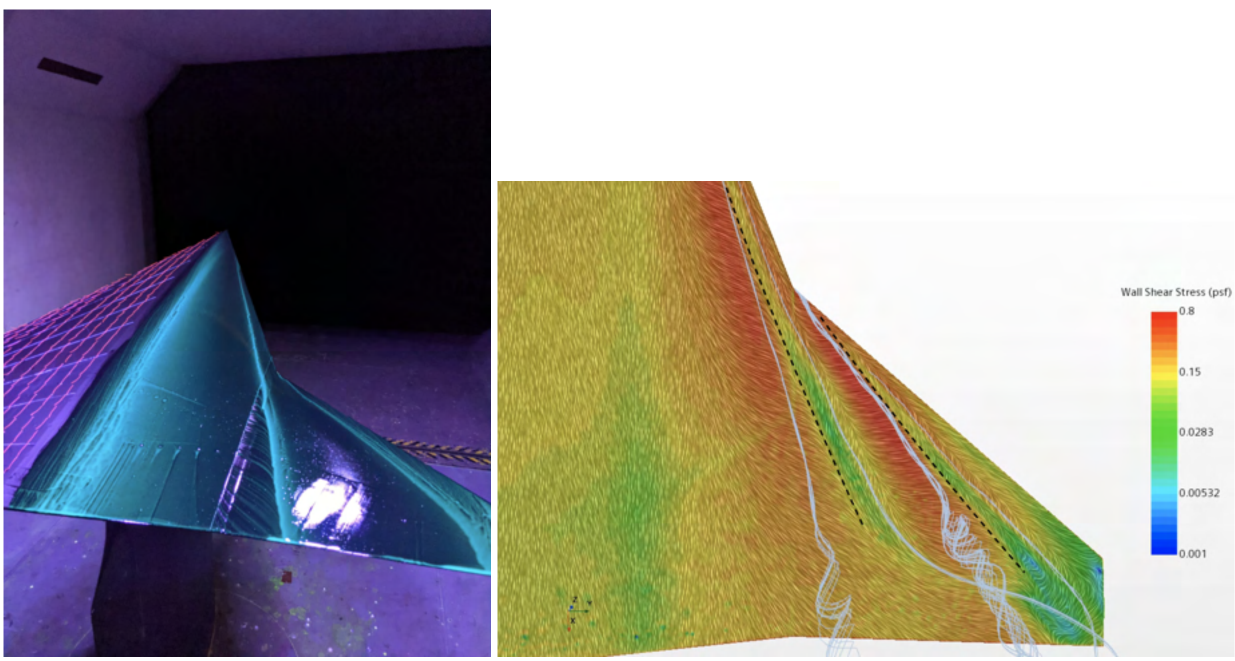

Figure 3.16: Comparison of KWT to CFD Skin Friction Visualization at $\alpha = 10^o$

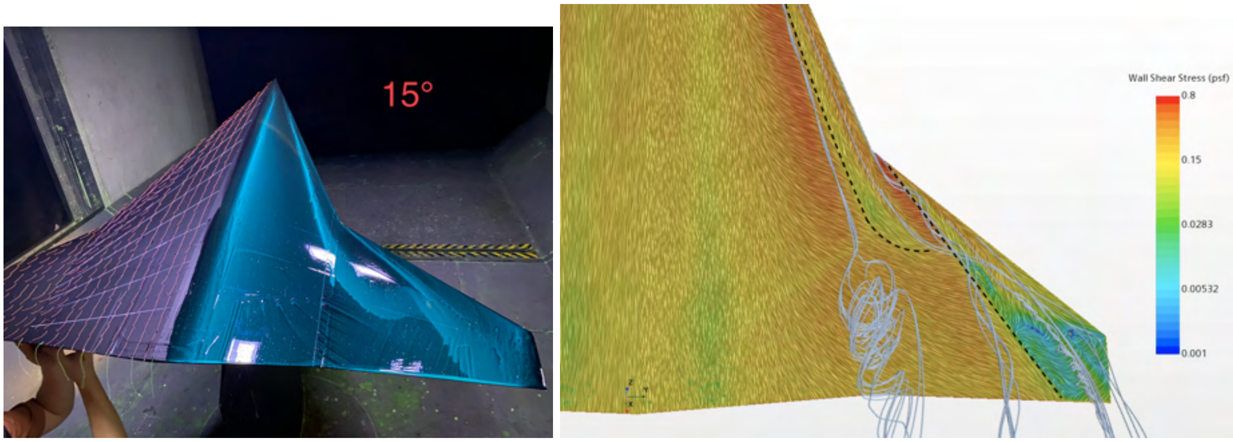

Figure 3.17: Comparison of KWT to CFD Skin Friction Visualization at $\alpha = 15^o$

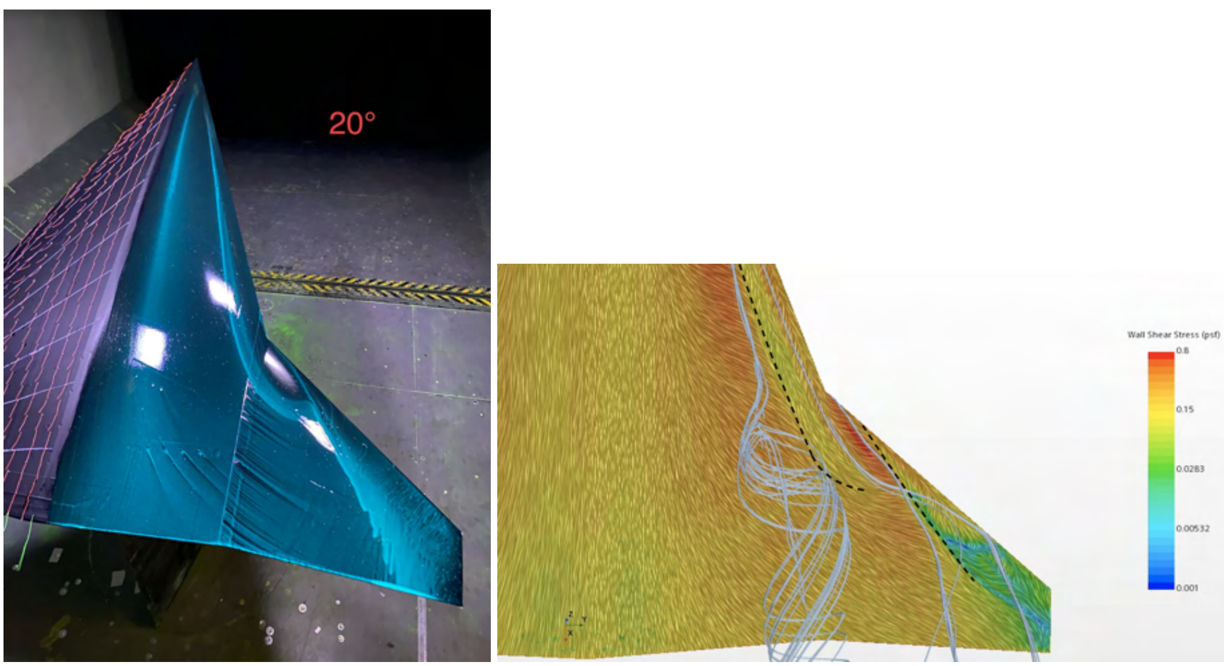

Figure 3.18: Comparison of KWT to CFD Skin Friction Visualization at $\alpha = 20^o$

Chapter 4

Model Support System Corrections

4.1 Introduction

The T&I corrections for the model support system are applied to the measured raw data in two parts: one set of T&I corrections as a function of sideslip angle and one set as a function of lift. Lift (pitch) T&I corrections include only drag, lift, and pitching moment T&I corrections. Yaw T&I corrections include all six forces and moments but drag, lift, and pitching moment are normalized to start at zero. Adding the two T&I corrections together forms the complete T&I correction for any given pitch and yaw combination. The lift coefficient of which the corrections are a function of, is the lift coefficient of the wing mounted on the support, C_{L_W}.

Lift coefficient is conventionally defined as:

$$C_{L_W} = \frac{L}{qS_{ref}} \tag{4.1}$$

Figures 4.1 and 4.2 show the T&I corrections for Fork 14-H at various dynamic pressures. The KWT Standard T&I corrections are given as forces (lbf) and moments (lbf-in) divided by dynamic pressure (psf) only (yielding ft^2 or ft^2-in as the units of the corrections). This allows customers to factor in their own reference areas (and reference lengths) to arrive at the final dimensionless coefficient correction - a "one-size fits all" correction approach. It was determined by the KWT in 1988 [3] that the fork corrections differed minimally past 25 psf. Thus, only one correction was deemed necessary above that dynamic pressure, indicated as 25+. The CFD based MSS T&I correction was only computed at one dynamic pressure, 40 psf. By extrapolating the correction to multiple dynamic pressures can be done by applying the differences in the original KWT corrections from one nominal dynamic pressure to another. It is assumed here that the same dynamic pressure effect applies and consequently the CFD derived correction is considered valid for any dynamic pressure above 25 psf.

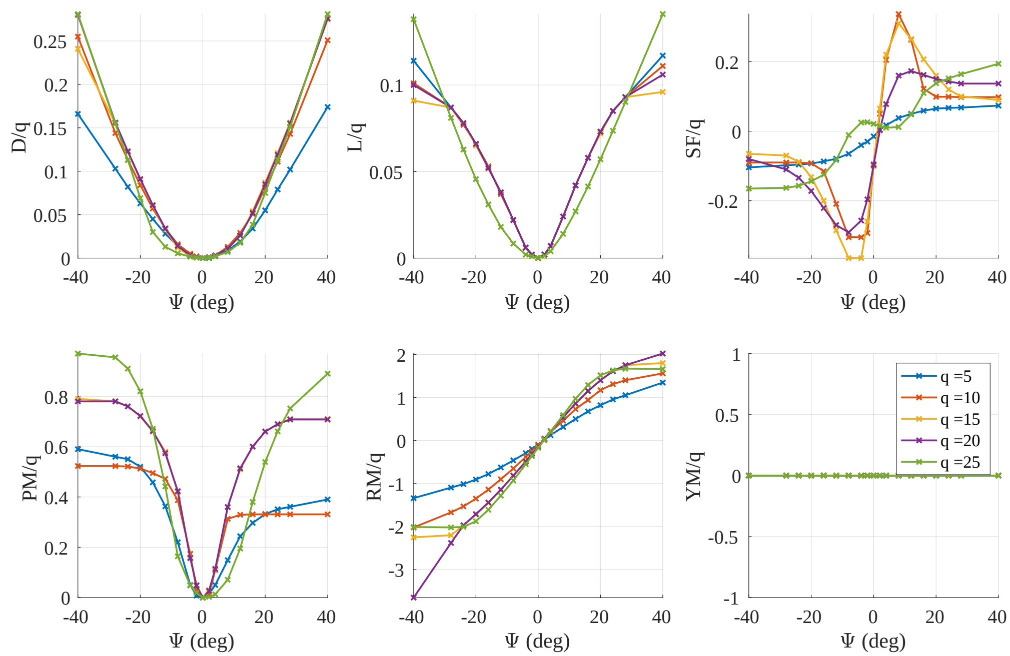

Figure 4.1: 1988 KWT Fork 14-H and Pitch Arm Sideslip Corrections for the NACA Wing Calibration Model

This set of T&I corrections was calculated in 1988 using the common T&I test procedure involving inverted mounting and a dummy strut and are outlined in UWAL Report 397-F [3]. The test performed in 1956 suspended the NACA wing calibration model and a flat disk by wires over the model support system and therefore could not directly measure the interference effects of the MSS on the models. The test in 1988 found slight differences in the T&I values but most notably, an increase in excrescence drag. These T&I corrections (in Figures 4.1 and 4.2) supersede those calculated in UWAL Report 397-B, performed in 1956, for the same fork and are nominally referenced as the KWT "Standard" MSS T&I.

The process of calculating T&I corrections for each test body mounted on the FPA (fork and pitch arm) is as follows: Each body (W15, NACA wing, Disk) was simulated alone in freestream conditions and on

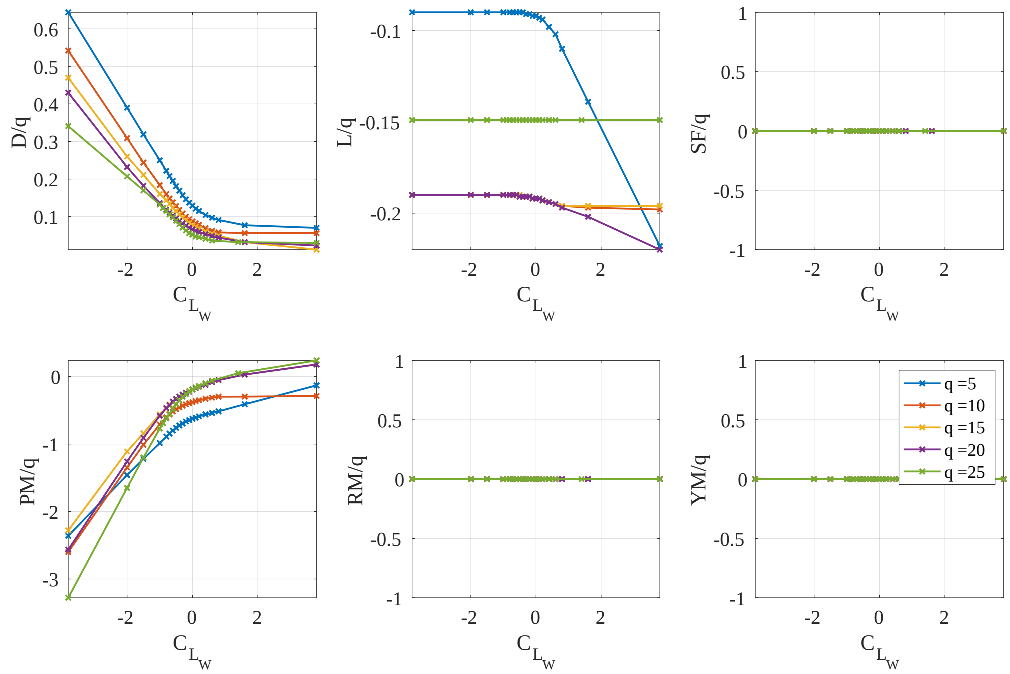

Figure 4.2: 1988 KWT Fork 14-H and Pitch Arm Lift Corrections for the NACA Wing Calibration Model

the MSS in freestream conditions. No walls were modeled, boundary conditions were identical, and mesh settings were held constant (as much as possible). In the NACA wing test case the floor on which the MSS stands on was modeled as a symmetry plane. The floor was also given the freestream boundary condition and the results showed no force and moment differences on the FPA or the NACA wing between the freestream and symmetry conditions. The W15 on MSS simulations modeled the system entirely in the freestream, i.e. no floor surface with imposed freestream or symmetry boundary condition. Rather the system was in a sphere (semi-sphere for alpha sweep simulations) like that shown in Figure 3.3.

Forces and moments on both the body and FPA were collected in CFD. The T&I delta calculation, shown visually in Figure 4.3, is:

$$\text{T\&I} = (\text{Body+FPA})_{\text{onMSS}} - \text{Body}_{\text{Freestream}} \tag{4.2}$$

Aerodynamic interference of the FPA (and the MSS fairing cap) on the body and interference of the body on the FPA are inherently part of the (Body+FPA) quantity.

Interference upon the wing (or test body) was also calculated, shown visually in Figure 4.4, as:

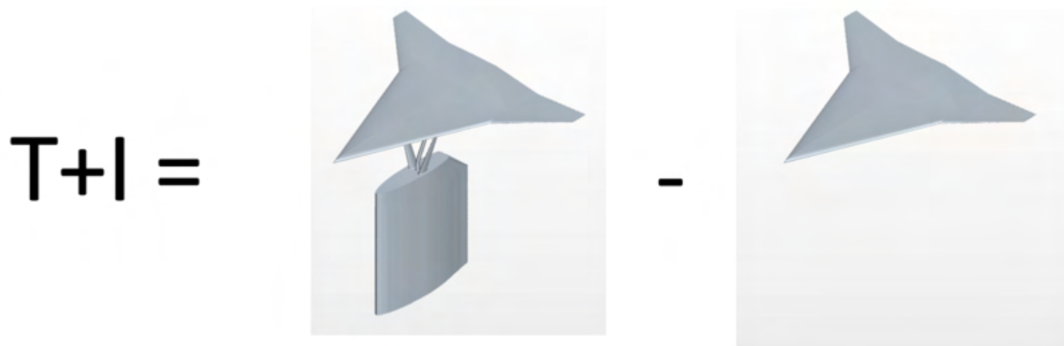

Figure 4.3: Visual Depiction of the T&I Calculation

$$\text{Interference} = \text{Body}_{\text{onMSS}} - \text{Body}_{\text{Freestream}} \tag{4.3}$$

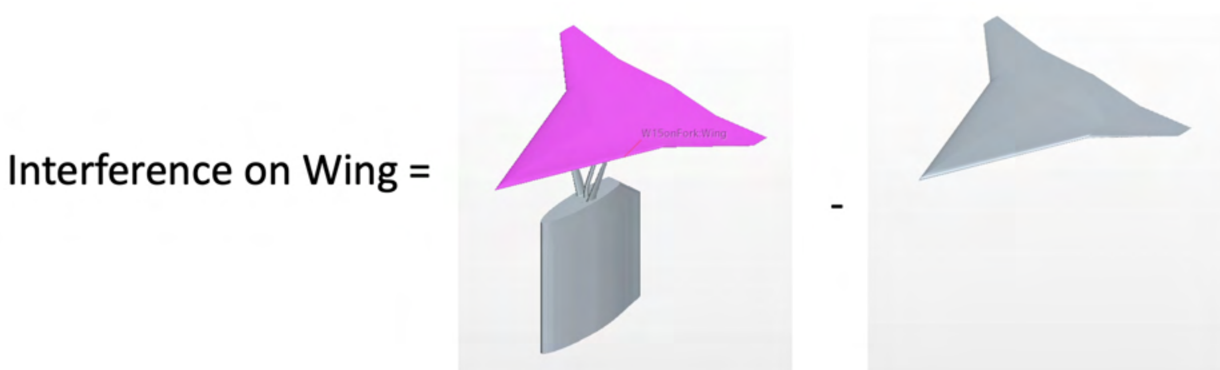

Figure 4.4: Visual Depiction of the Calculation of Interference Upon the Wing

The CFD simulations give us the freedom to isolate the forces and moments on the FPA and the body and identify the elements of the interference on the T&I corrections, i.e. the I in T&I.

Figure 4.5 shows the three bodies modeled on the MSS as they are simulated in Star-CCM+. The disk had surface mesh refinement on the edges of the bulges that meet the disk surface, on the edges of the intersection of the fork and disk, and on the top of the fairing cap, Figure 4.6. The trip dots on the disk were not modeled in the CAD model or Star-CCM+ simulation. Early simulations modeling the trip dots on the disk with turbulence suppression proved to have no discernible difference chiefly in drag, pressure or shear.

Similarly, W15 and NACA wings had surface mesh refinement on the trailing edges, wingtip edges, on the edges of the intersection of the fork and disk, and on the top of the fairing cap.

The prism layer setting proved to be robust in building adequate prism layer meshes on the fork, Figures 4.8 and 4.9. Additionally, the prism layer mesh on the fairing was coarsened to adequately solve the boundary layer flow without striving for the utmost of accuracy in order to reduce mesh size and, therefore, computation time, Figure 4.7.

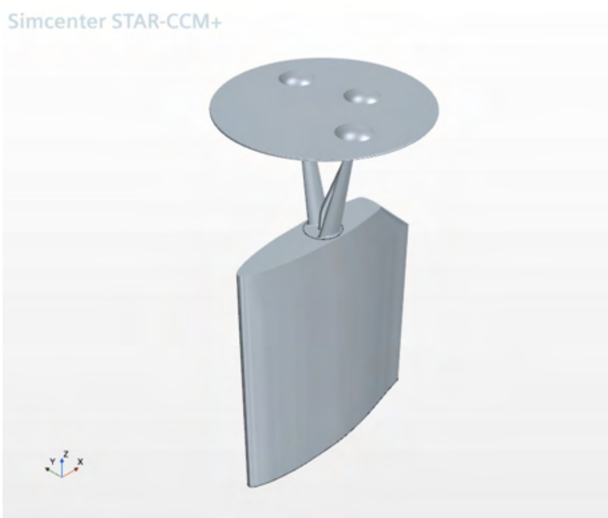

(a) Disk and MSS Model in Star-CCM+

(b) W15 and MSS Model in Star-CCM+

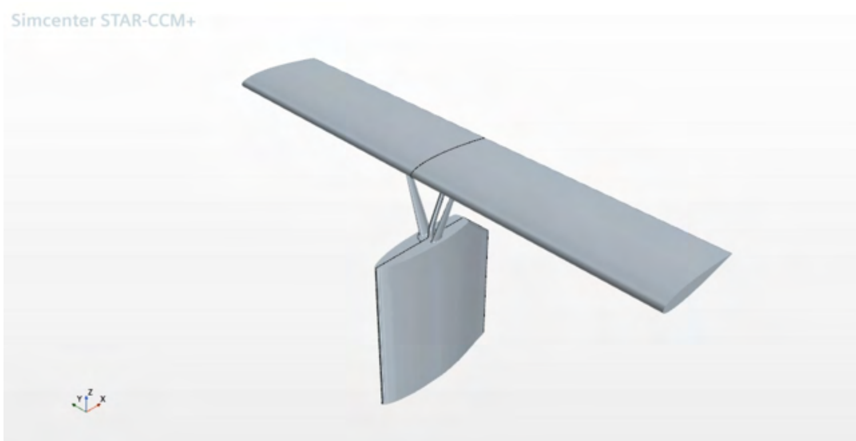

(c) NACA Wing and MSS Model in Star-CCM+

Figure 4.5: Modeled Bodies on Model Support System in Star-CCM+

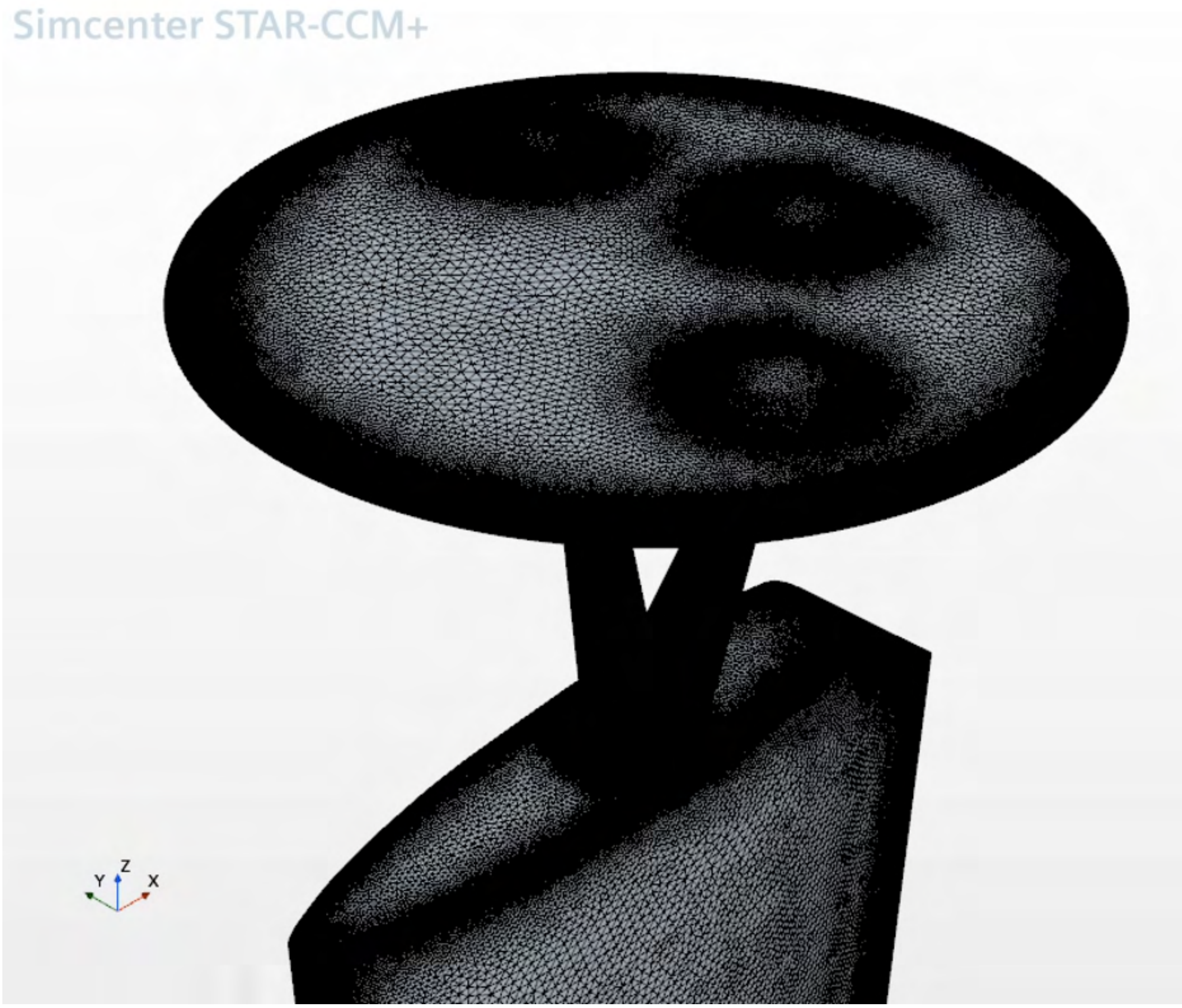

Figure 4.6: Surface Mesh Refinement of the Disk and MSS Model

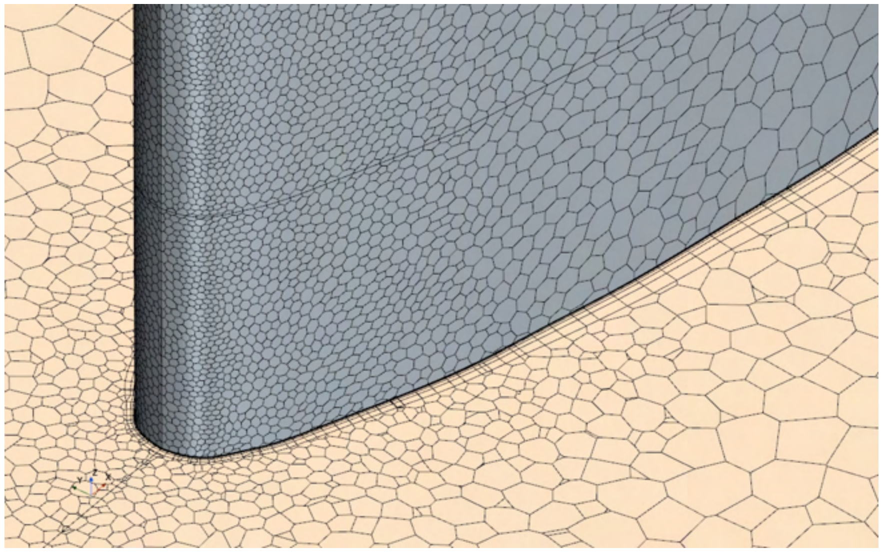

Figure 4.7: Fairing Volume and Prism Layer Mesh Close Up

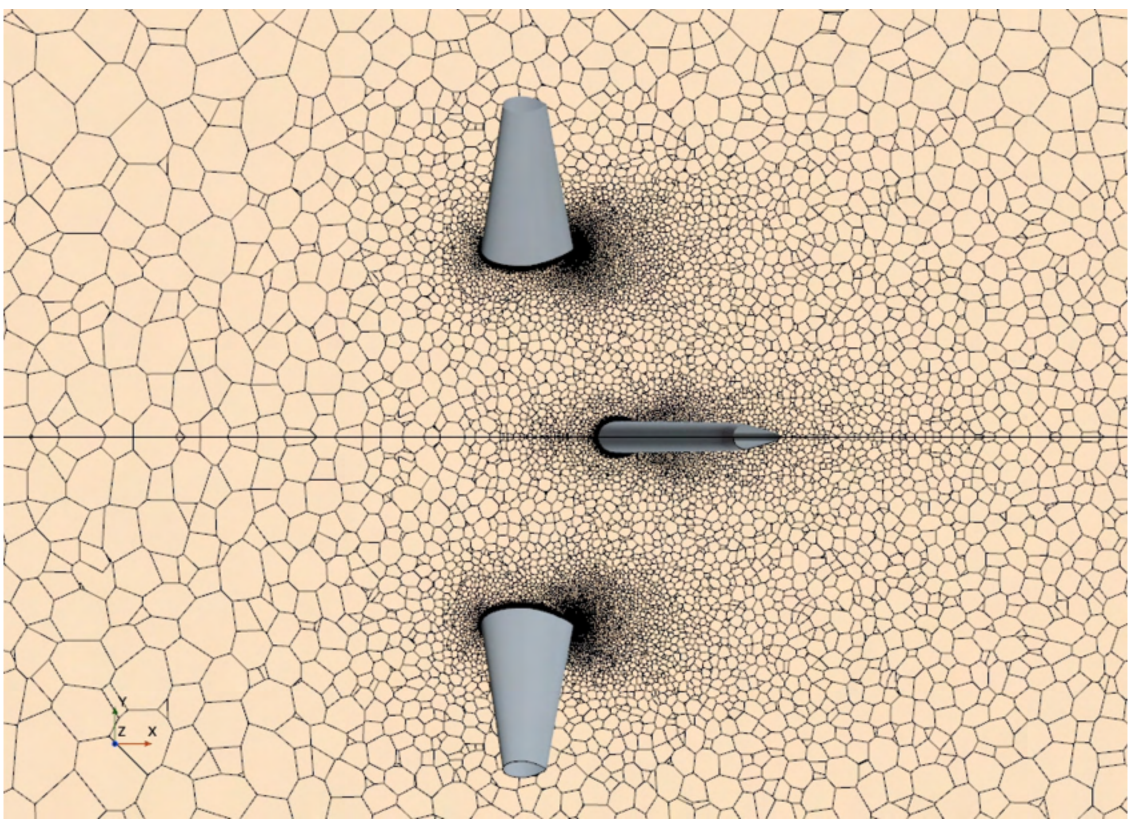

Figure 4.8: Fork Volume Mesh

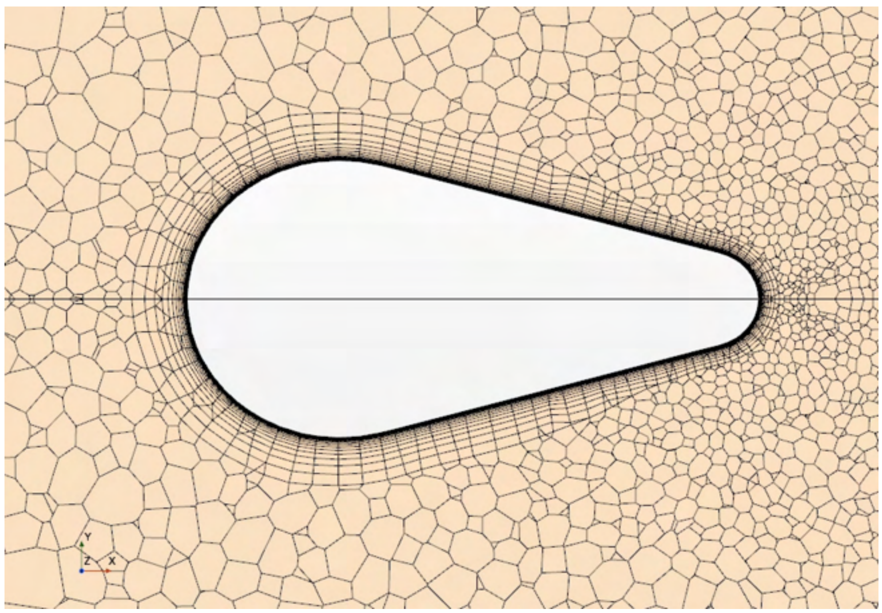

Figure 4.9: Pitch Arm Volume and Prism Layer Mesh Close Up

4.2 Standard KWT Fork 14-H T&I Corrections

As seen from Figure 4.10, the KWT's common experimental correction technique included the three-dimensional NACA-airfoil wing installed on the FPA, with a similar FPA - a "dummy FPA" - attached to the ceiling of the tunnel and brought down very close to the upper surface of the model, without touching the model. That is, in a case like this the dummy fork affects the configuration aerodynamically, but the balance below the floor measures only the loads on the model and the actual fork. There also has to be an image "dummy" fairing from the ceiling that covers the dummy fork the way the floor fairing covers the actual fork. The ceiling dummy fork can be attached or not attached to the top of the wing. When it is attached to the top of the model the external balance measures the integrated loads of the model and the two forks in the presence of two (floor and ceiling) fairings. For actual models the model has to be tested in the upright and inverted (upside down) positions and tested on the floor support alone and also on the floor support in the presence of the ceiling mirror-image support.

The resulting variations for the NACA Wing of the corresponding forces and moments corrections with respect to both the yaw angle and wing lift coefficient, for several dynamic pressures were shown earlier in Figures 4.1 and 4.2.

This figures show that the effects for most dynamic pressures tested are symmetric with respect to the yaw angle as expected. For dynamic pressures of five and ten psf, however, the moments (pitching,yawing, and rolling) are not symmetric. The asymmetries are most likely an effect of imperfect (not fully symmetric) manufacturing but the authors of the original UWAL correction and interference report did not investigate the root cause(s). As a starting point, the KWT and the SCALOS team continued to use this data to account for the fork 14-H tare and interference corrections for all SCALOS tests. However, it was obvious that the SCALOS wings were completely different than the NACA Wing and there was a concern that the this T&I correction scheme might not be accurate enough. Specifically, you can see from the photo in Figure 4.10b that the supports are on an area of the wing where they could impact wing pressures (short chord, significant surface curvature), increasing interference on the wing but the wing area and chord would have much less influence on the flow around the FPA than the large cranked-delta wings. It was decided, therefore, to further investigate the tare and interference effects via CFD, since the SCALOS wind tunnel models available for tests at the start of the project were not prepared for being mounted upside down and so a full T&I campaign using a mirror FPA system was not possible. The photos and data that cover the establishment of the "standard" KWT T&I corrections were taken from the UWAL report [3].

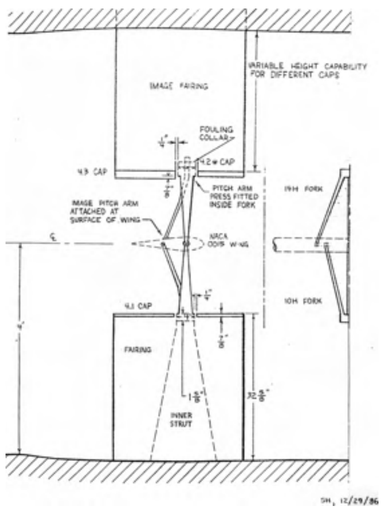

(a) Fork 14-H and Pitch Arm T&I Method Diagram

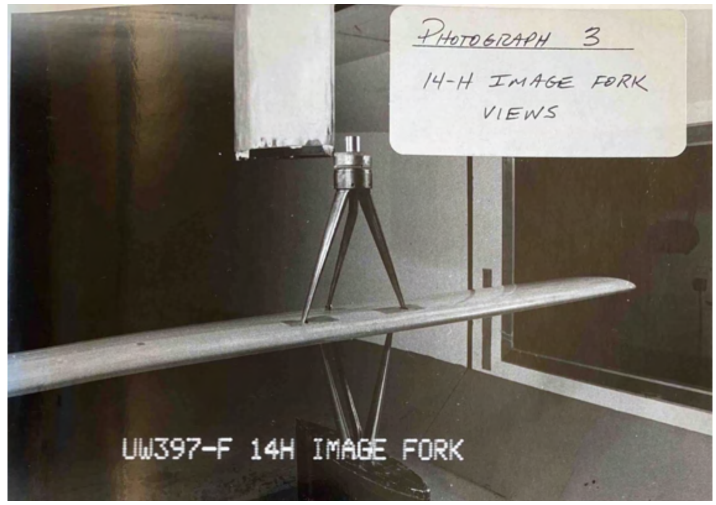

(b) Rectangular Calibration Wing Mounted on FPA with Image Fairing and FPA mounted

Figure 4.10: Original Fork 14-H and Pitch Arm T&I Test[3]

Figure 4.11: 14-H Fork Profile Cutouts in the Disk Blisters and Pin Fairings

An important additional note: The airfoils of fork 14-H were thought to be symmetric and were modeled as such for CFD analysis. Yet, it was discovered in June 2022 that this is not the case, see Figure 4.11. This partly explains some of the asymmetry in yaw that was described earlier.

4.3 Correlation of CFD Predictions with Measured KWT Data

Fork and Fork+Disk Data - CFD Validation

Figures 4.12 and 4.13 show the correlation between the CFD simulations and the KWT experimental data for the cases of the Disk model on the FPA and the case of no-disk, with pins over the pis of the prongs of the fork and pitch arm. Here, forces and moments are normalized by dynamic pressure only, a practice introduced by the KWT to allow S_{ref} and reference length to be applied to the MSS T&I correction for any model. Drag is under-predicted, as expected, mostly due to the CAD model having smooth surfaces and the KWT machined model being relatively rougher. Mesh and turbulence model selection and settings may play a role in drag under-prediction as well. Drag and lift discrepancies likely explain the difference in pitching moment, given that an increase of drag will increase the negative magnitude of the pitching moment since the entirety of the fork is below the tunnel centerline (z-direction). Lift values are offset because lift was zeroed in the KWT during testing by pitching the disk up/down but not this was not done in CFD, yet curve trend similarities are apparent. Negative lift values predicted by Star-CCM+ may be due to the lack of free air modeled between the fairing and fork - CFD models this space simply as a surface (see Figures 2.4 and 2.6a), resulting in a downward force due to the pressure upon it. Also potentially affecting the lift values are the fork airfoils, recall the KWT fork has cambered airfoils while the CFD airfoils are symmetric. The discrepancies in side force and rolling moment are also most likely due to the cambered airfoil sections the real fork has. All of these discrepancies are attributed to the fork and pitch arm model discrepancies. Once yawed past the stall point of the CAD-defined fork, there is an offset in the results but the data trends in the same direction as in the case of the real fork.

Perhaps the most important piece of information gathered from these simulations is the fact that the incremental difference in drag between the FPA+Pins and the FPA+Disk is practically the same for both the KWT and CFD data. The KWT data delta is 37.8 counts and the CFD data delta is 37.4 counts (normalized by W15 reference area), not even a half count difference between the two. Furthermore, evaluating all incremental differences of the disk model upon the fork mount from the fork with the pin fairings for both the CFD and KWT data further supports the argument that the CFD data can reliably be used for incremental data, Figure 4.14. The effect of the disk on side force, rolling moment, and yawing moment is near zero and

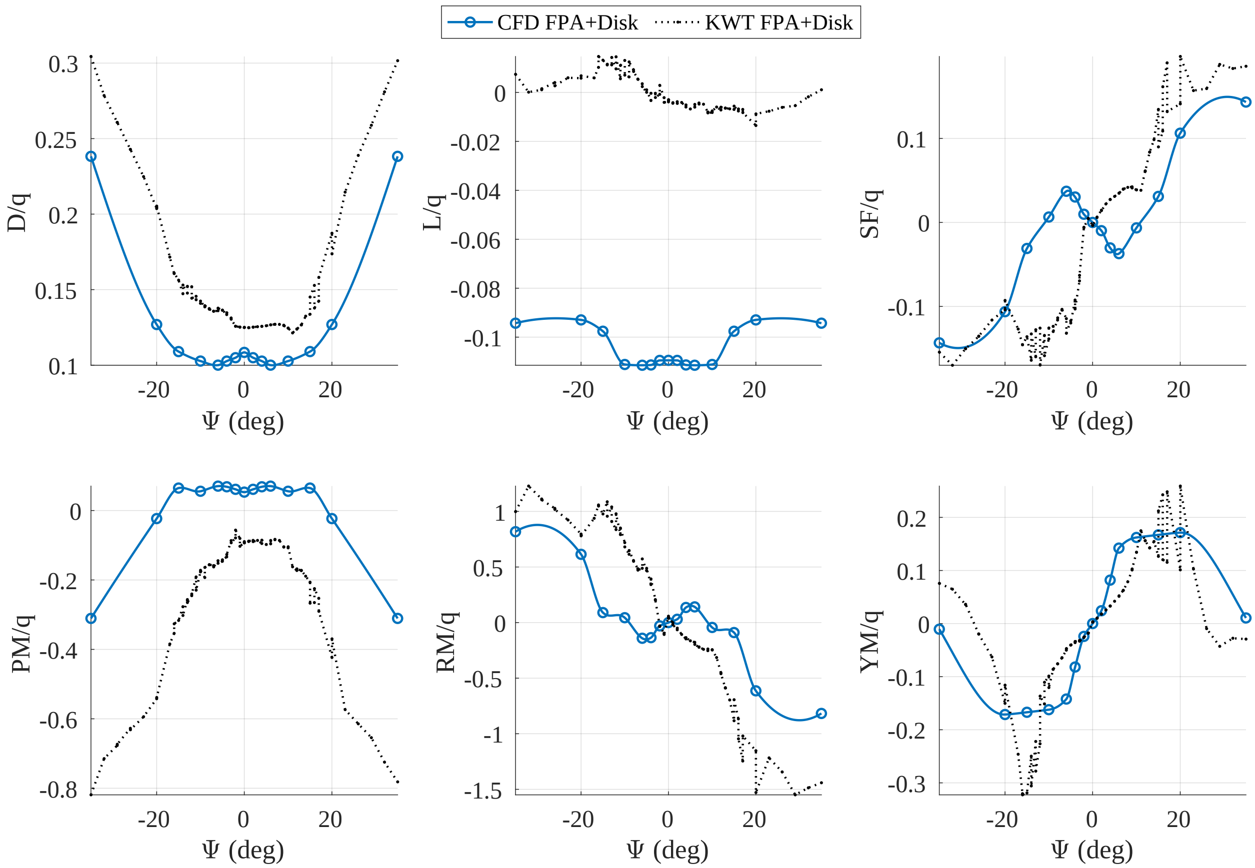

Figure 4.12: Comparison of CFD Data to KWT Data for FPA and Disk (q = 40 psf) (Forces and Moments Normalized by Dynamic Pressure)

has much noise. The effect is negligible, and the cases are modeled well by the CFD simulations. The CFD drag and pitching moment incremental effect values compare well to those of the KWT withing 10 degrees of sideslip and the trends match outside of that region also compare well. The lift trend also compares well, However, the absolute value of the lift near 0 degrees of sideslip angles is larger (more negative), suggesting the simulations over-predict the loss of lift, the start of a recurring pattern seen with these simulations.

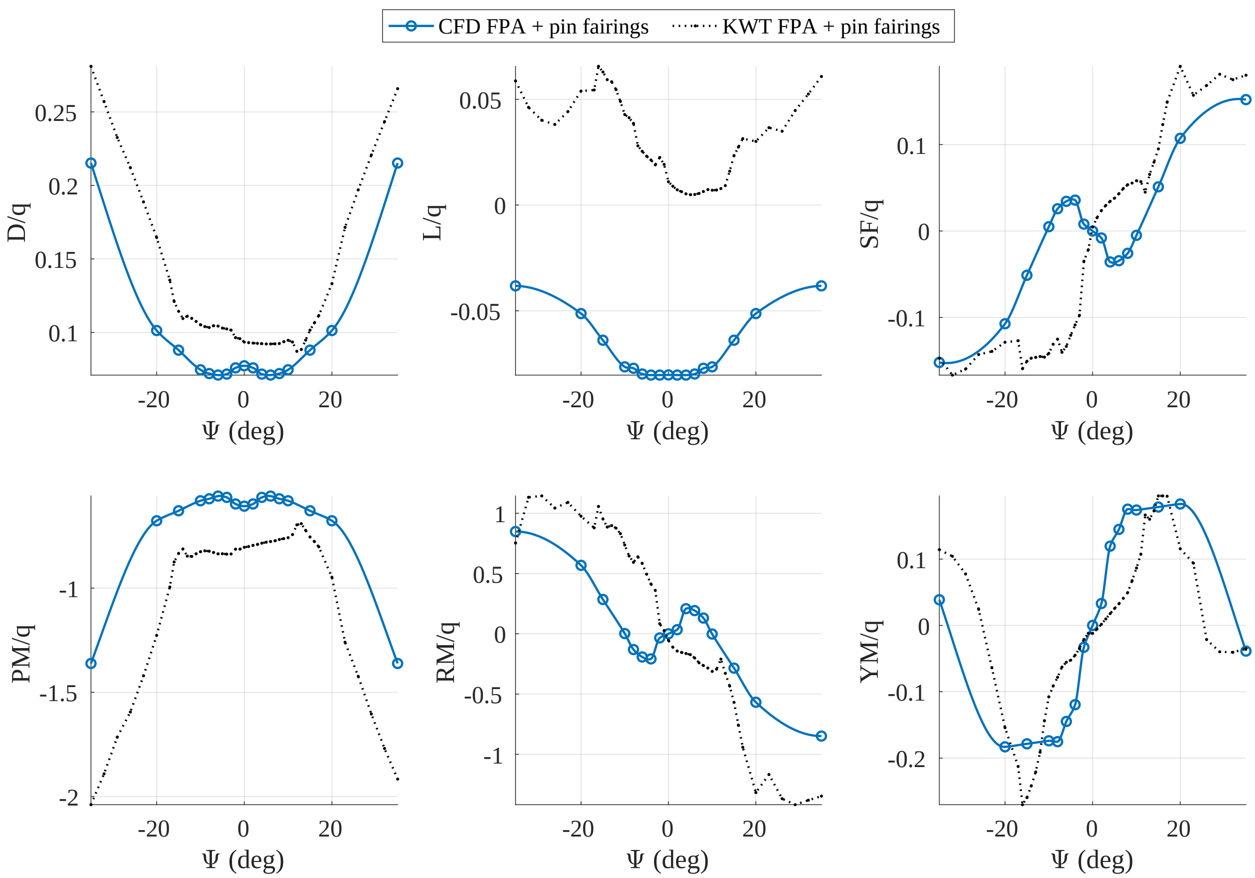

Figure 4.13: Comparison of CFD Data to KWT Data for FPA and Pin Fairings (q = 40 psf)

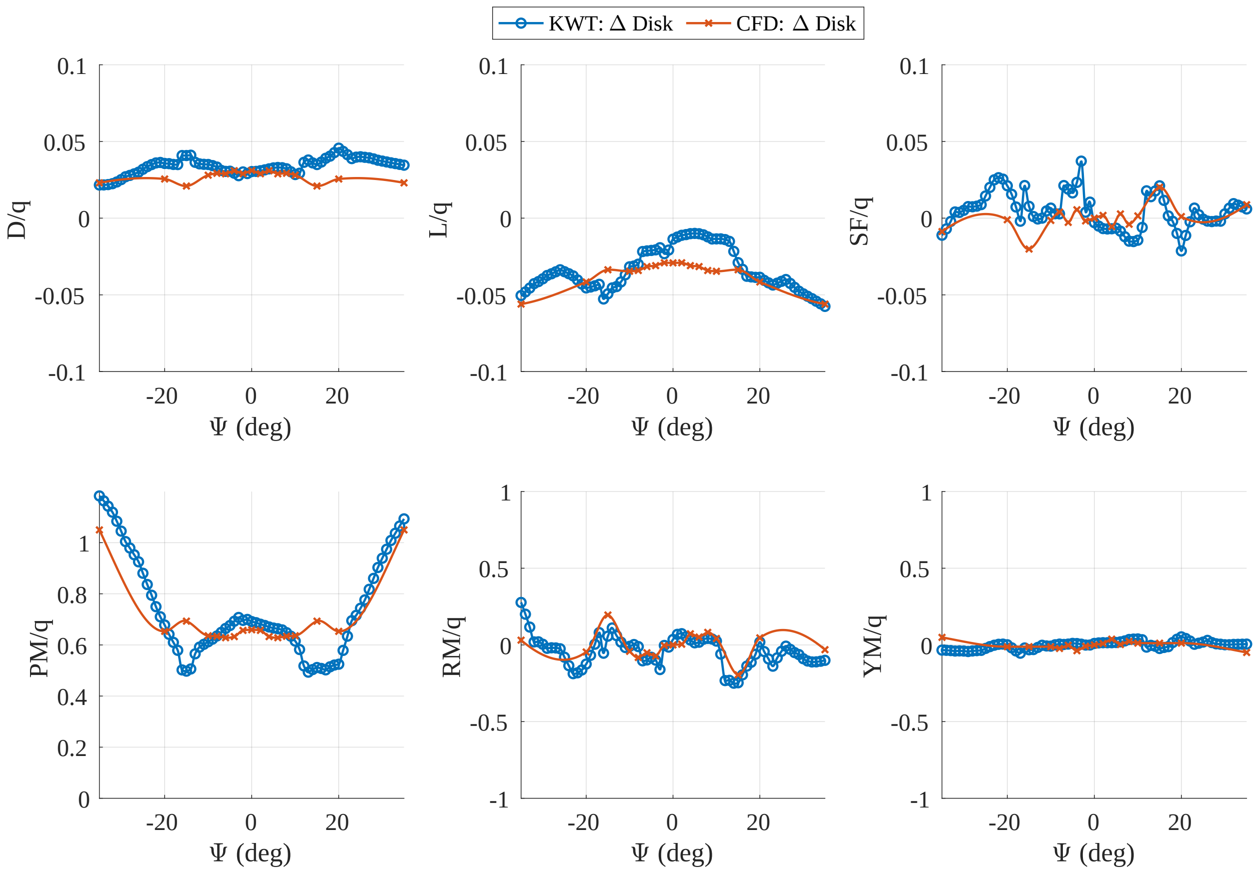

Figure 4.14: Comparison of Incremental Effects of the Disk Model Upon the MSS (q = 40 psf)

4.3.1 NACA Wing T&I Correction Validation

Lift Based Correction

A validation case was performed for the CFD derived T&I corrections using the NACA 0015 wing used in the KWT in both UWAL Reports 397-B and 397-F to validate the use of CFD for incremental data and correction calculation.

CFD results for the NACA 0015 wing in freestream and on the MSS, both isolated and including the FPA, are shown in Figure 4.15 and show the effects of the FPA on the model when pitched. A half model was used in CFD to reduce computational time, thus non-symmetric CFD-based forces and moments are simply zero in this case. Figure 4.16 shows the interference between of FPA upon the NACA 0015 wing is non-negligible and on similar order of magnitude of forces and moments on the FPA itself. Therefore, interference effects should not be neglected or assumed to be insignificant.

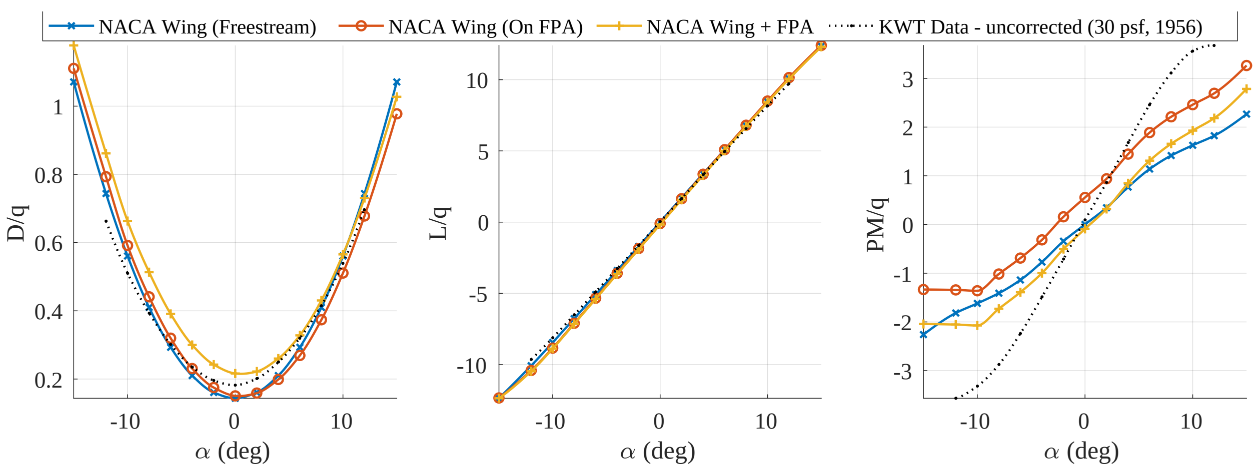

Figure 4.15: CFD Results of NACA 0015 Wing in Freestream and on MSS vs angle of attack (q = 40 psf)

Figure 4.17 shows that the CFD-derived and KWT corrections that are lift-dependent. The curves are similar in direction and slope near zero lift for the drag and pitching moment corrections. The CFD lift correction curve shows variations of the correction as a function of lift. Yet, the CFD-derived line is centered around the same lift value as the constant lift-dependent KWT correction. It is important to note that for the development of the KWT corrections, test data was collected from -0.8 to 0.8 lift coefficient in the KWT and corrections were extrapolated outside of the region by hand. For reasons that are absent in the KWT report that describes the work, the correction due to lift correction was assumed to be constant. [3]. It should also

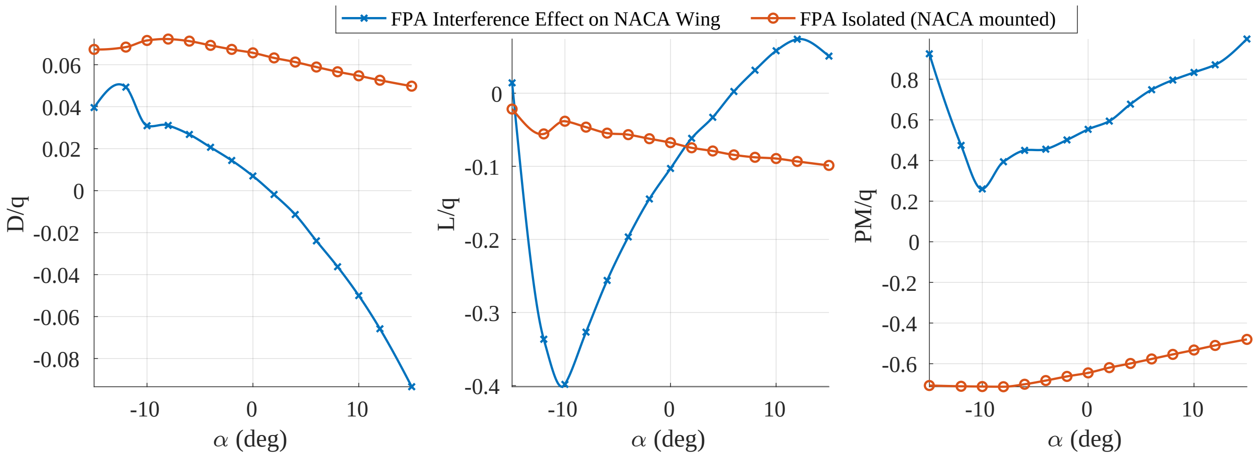

Figure 4.16: CFD Results of FPA and Interference Between FPA and NACA 0015 Wing vs. α (q = 40 psf)

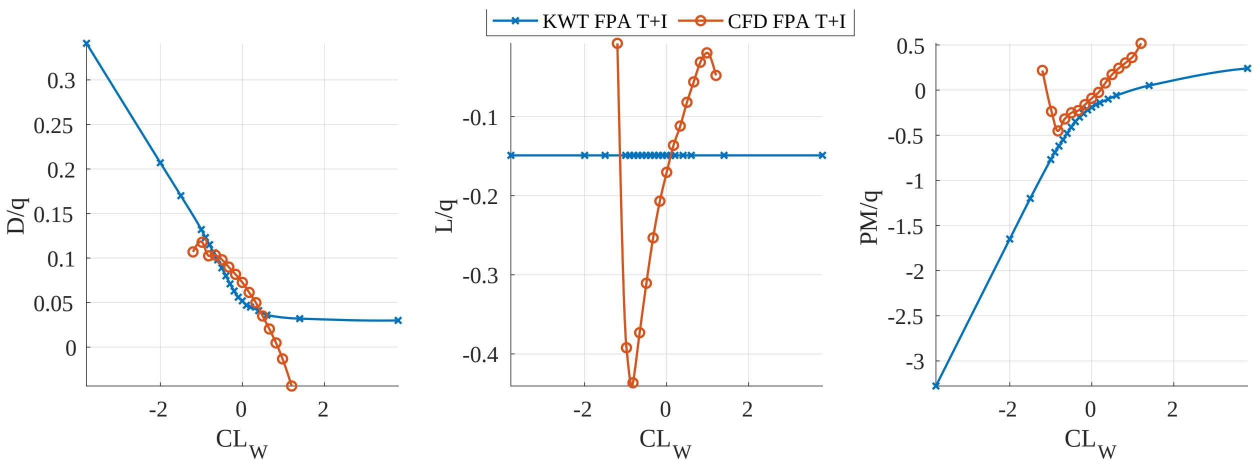

Figure 4.17: Comparison of CFD Predicted Correction and KWT Standard Correction - Lift Based Correction of the T&I Correction (q = 40 psf)

be noted the reference area of the NACA wing was calculated as simply span multiplied by chord.

Yaw Based Correction

Similarly to the lift based simulations, results for the NACA 0015 wing in freestream and on the MSS simulations, both for wing in the presence of the MSS and also the integrated loads on the wing and the MSS together, are shown in Figure 4.18 and present the effects of the FPA on the model when yawed. Figure 4.19 also suggests the interference of the FPA upon the NACA 0015 wing is non-negligible and on similar order of magnitude of forces and moments on the FPA itself.

Figure 4.20 shows that the CFD derived correction trends correlate well to the KWT correction across all load channels although not perfectly (especially in the cases of the lift and yawing moment) - likely due to the differences between the CAD model and the real manufactured FPA and natural limitations of RANS-CFD. UWAL Report 397-F [3] explains the decision to apply no correction for yawing moment because the moments was insignificant. This may have merit considering the maximum yaw moment correction in fig. 4.20 is about eight lbf-in, a possibly negligible amount on a large, installed model.

Knowing the trends compare well between CFD correction methods and KWT experimental methods, and incremental data compares well too, this was deemed sufficient to proceed to simulating the disk and W15 models to augment the KWT Standard T&I corrections.

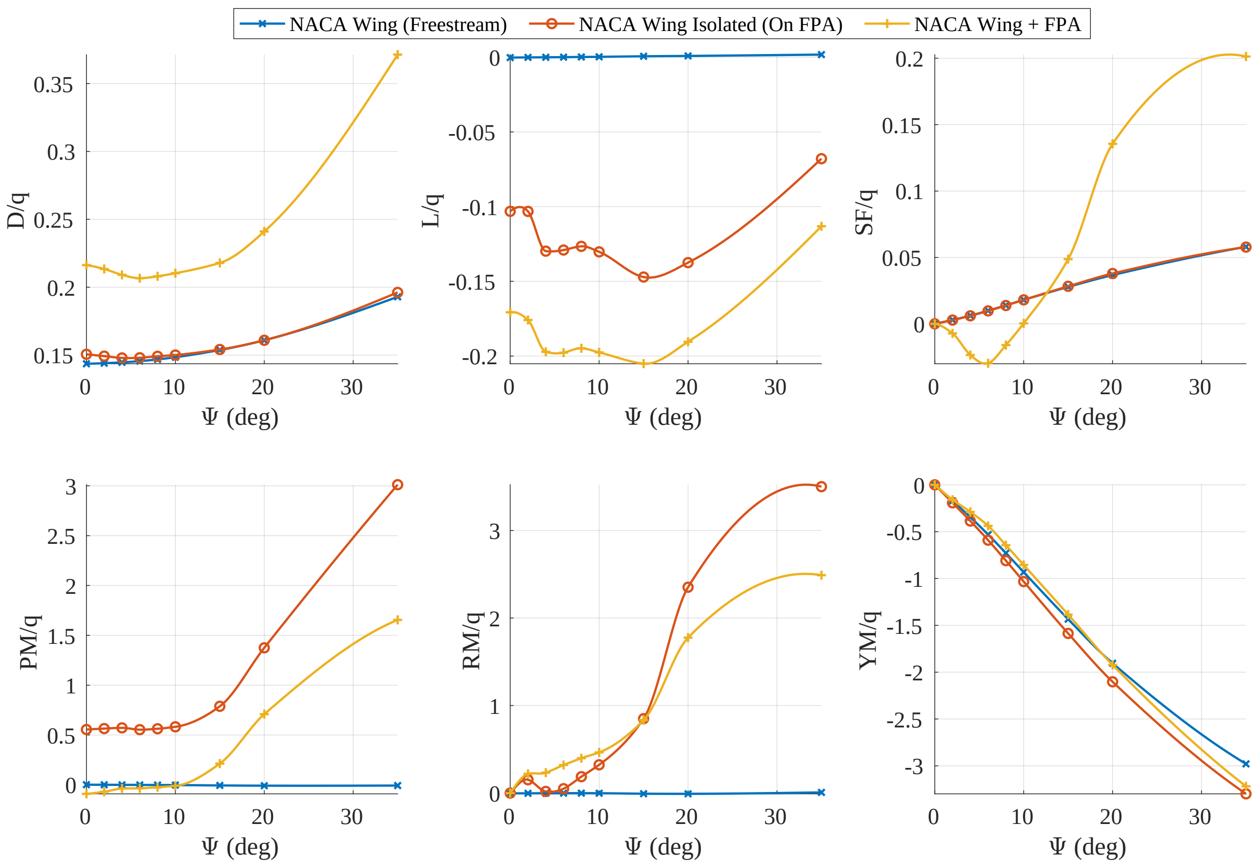

Figure 4.18: CFD Yaw Results of NACA 0015 Wing in Freestream and on MSS (q = 40 psf)

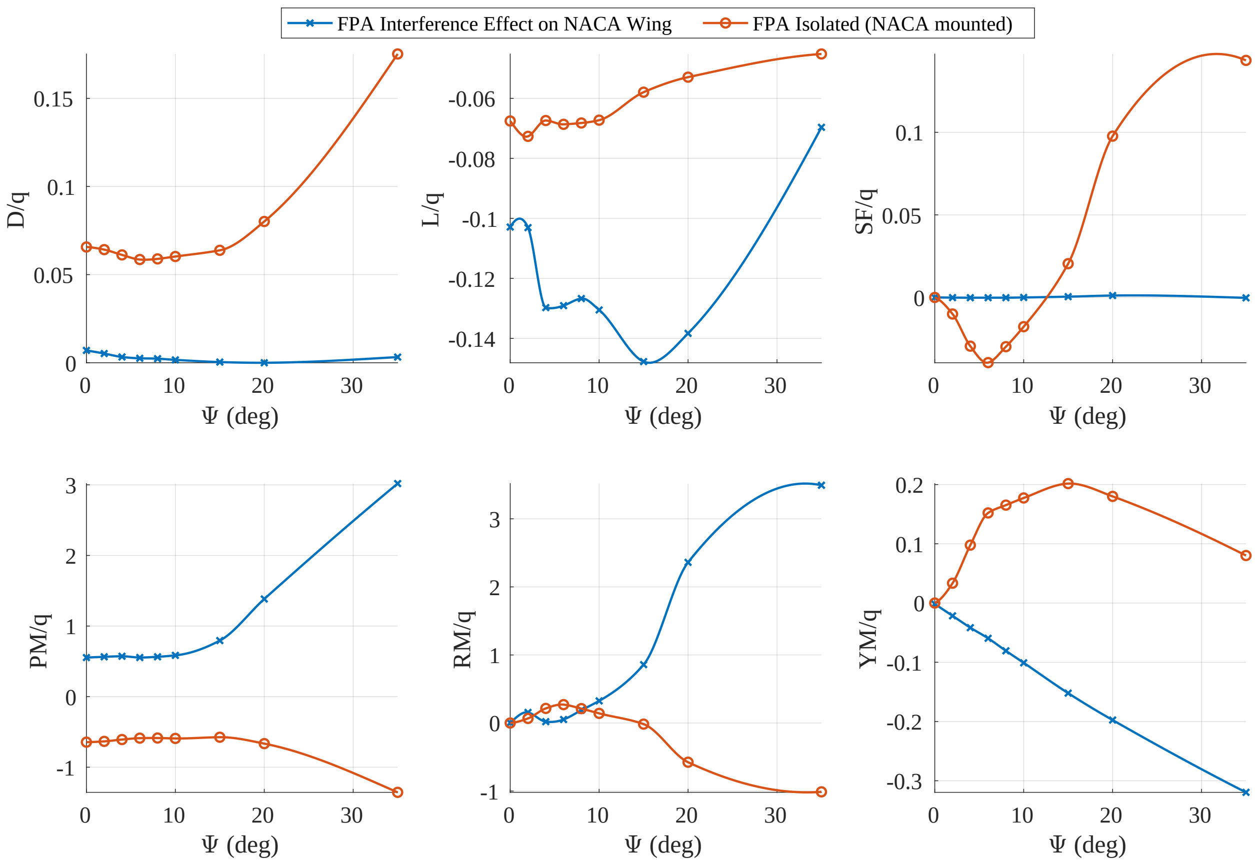

Figure 4.19: CFD Yaw Results of FPA and the Interference Effect of the FPA upon the NACA 0015 Wing (q = 40 psf)

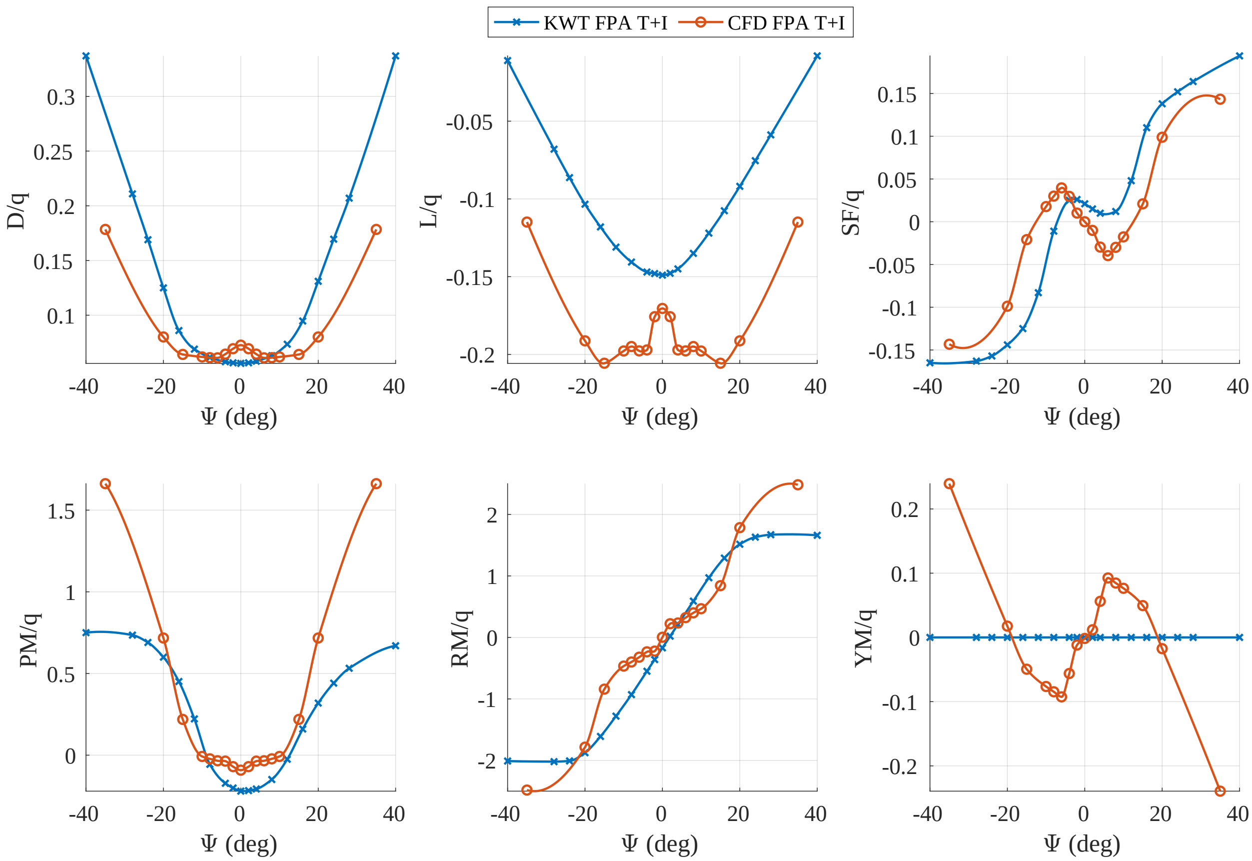

Figure 4.20: Comparison of CFD and KWT NACA 0015 Yaw FPA T&I Correction (q = 40 psf)

4.3.2 Yaw Based T&I Correction with Disk Model

CFD results for the disk yaw simulations are presented in Figure 4.21. Forces and moments on the disk in freestream are negligible. This is, however, not the case when it is mounted on the MSS (labeled "Disk isolated"), again indicating that the interference upon the disk from the FPA is significant. Figure 4.22 shows that the interference on disk is significant but not as large as the interference on the NACA 0015 wing, Figure 4.16.

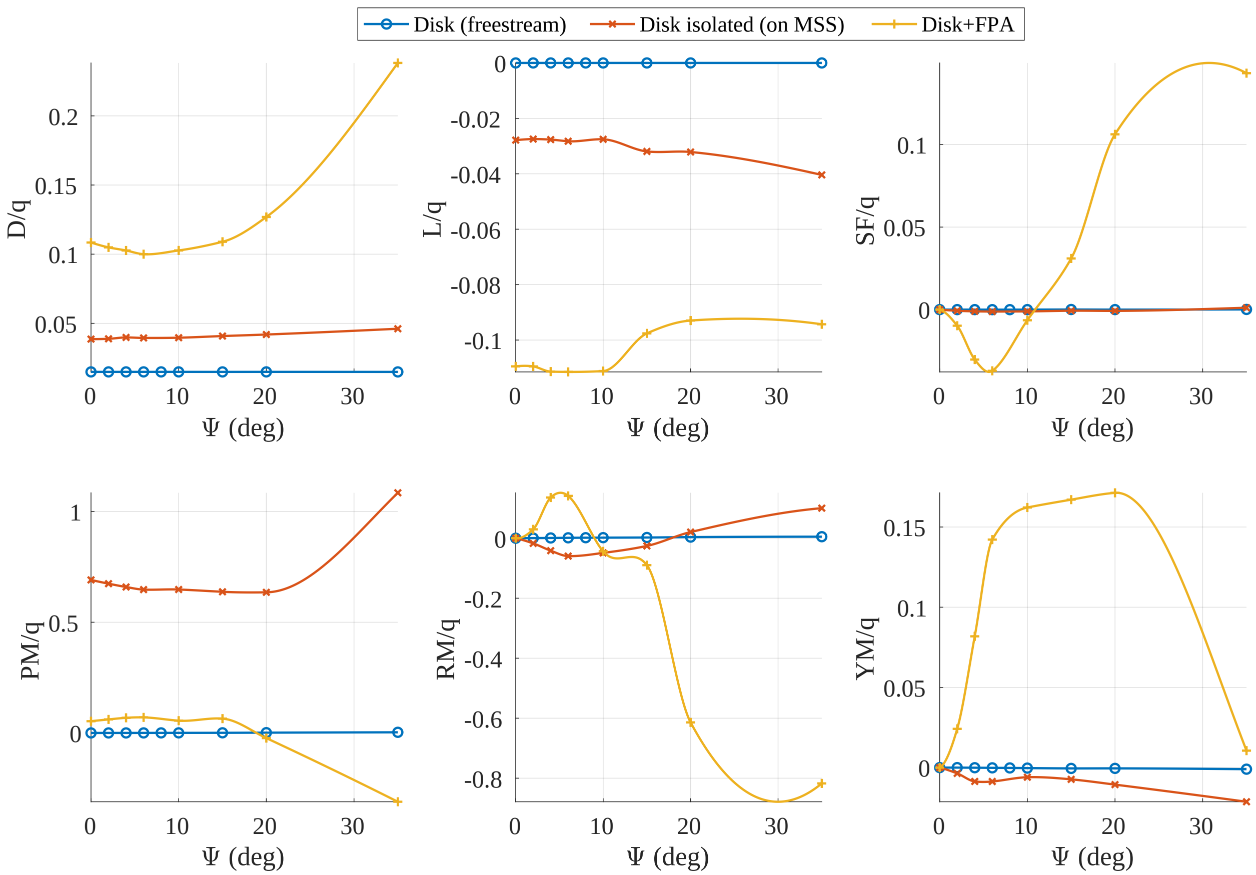

Figure 4.21: Yaw Data of Disk in Freestream and on MSS

When comparing the CFD derived T&I correction to the KWT experimentally derived T&I corrections from 1956 [22], the trends of the results correlates well in Figure 4.23. Again, the pitching moment curve has the correct shape but the CFD derived correction does not account for as much negative pitching moment, resulting in a shift of the curve. The KWT experimental T&I correction for drag is lower (but same trend of the curve) than the CFD derived correction. This is likely because the disk used for T&I tests in 1956 in the

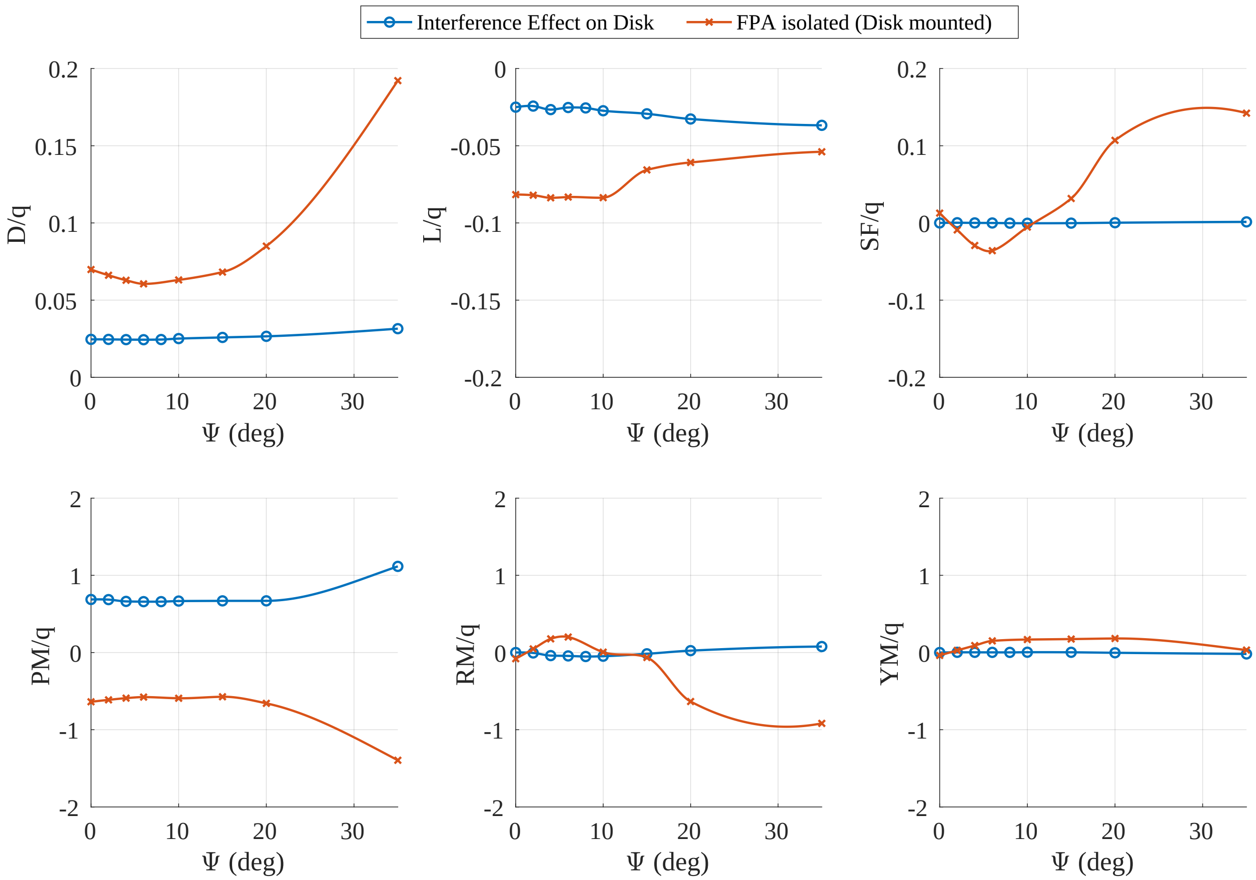

Figure 4.22: Yaw Data of FPA and Interference from FPA upon Disk

KWT used sharp long trailing edges to minimize the wake drag. Lift, side force, and rolling moment curves correlate relatively well. Revisiting the fork validation case, Figure 4.13, CFD under-predicted drag on the fork. Therefore the KWT drag correction is insufficiently low. The lift and pitching moment corrections follow the same trend as in the validation case: lift is negative and the pitching moment curve is similar but also shifted up (more positive).

Comparing this CFD disk yaw correction, Figure 4.23, to the CFD NACA 0015 wing yaw correction, Figure 4.20, the most evident difference is with the pitching moment; the two T&I correction curve shapes are almost exactly reflected across the x-axis. This indicated that the pitching moment T&I correction is much more sensitive to the body mounted on the MSS than previously thought. This leads to the conclusion that the pitching moment T&I correction for the SCALOS project representative wings, needed to be computed using the results from the W15 mounted on the MSS.

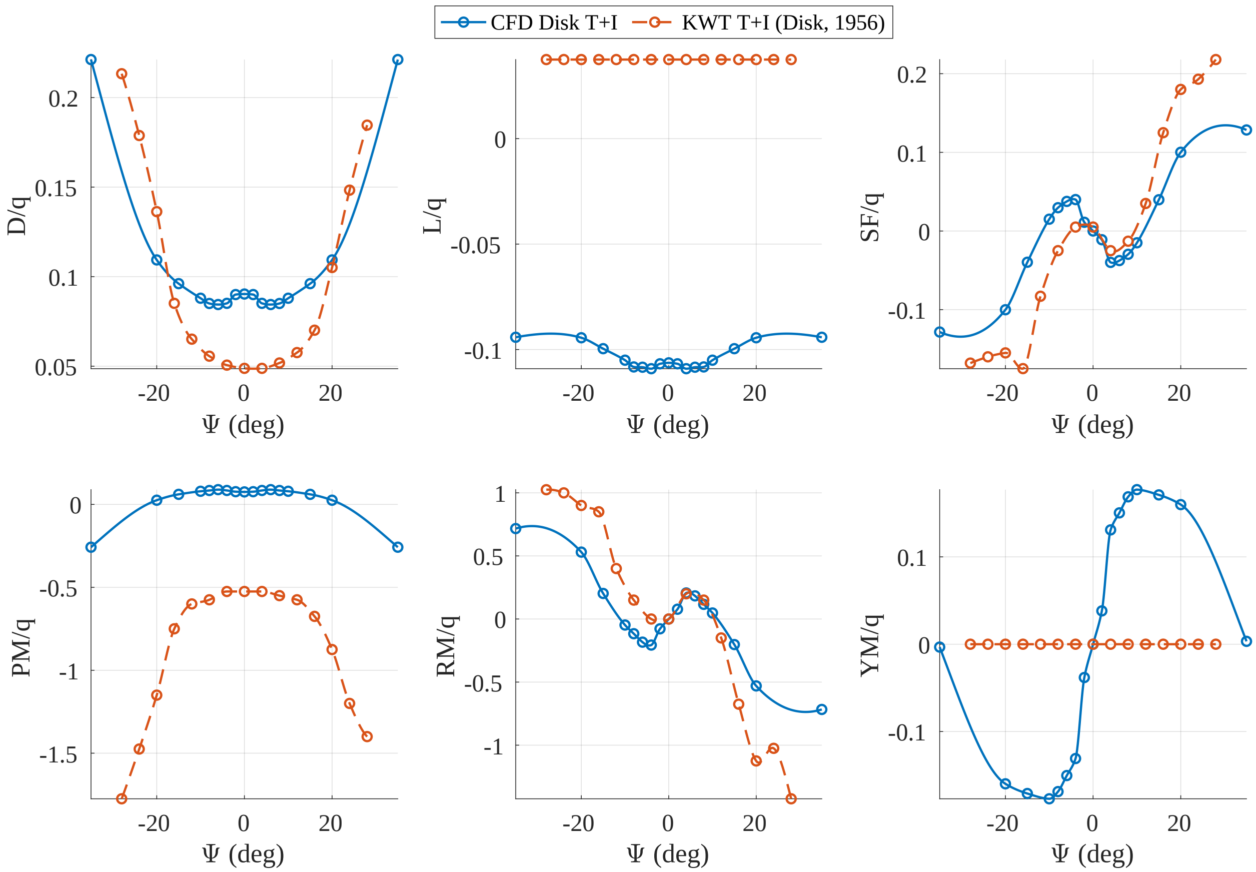

Figure 4.23: Comparison of CFD and KWT Disk Yaw Corrections

4.3.3 Yaw Based T&I Correction with W15

Yaw results for the W15 in freestream conditions and on the MSS are shown in Figure 4.24. Again, interference on W15 from FPA is non-negligible, Figure 4.25.

The CFD-derived W15 yaw correction is shown in Figure 4.26 and is compared to both the KWT disk and NACA 0015 wing corrections. It is evident that the CFD W15 yaw correction correlates much better with the KWT disk yaw correction with about as much error as the CFD disk yaw correction. Comparing the CFD disk to W15 yaw correction, Figure 4.27, the two corrections are essentially identical for side force, rolling moment, and yawing moment - the forces and moments directly dependent on sideslip angle. Lift, drag, and pitching moment correction curves are almost identical in shape but offset, which indicates a difference in interference effects due to lift - an example of the pitch sensitivity on the T&I correction.

Figure 4.28 shows the differences between the interference effects on the disk and the 2015 Wing. The

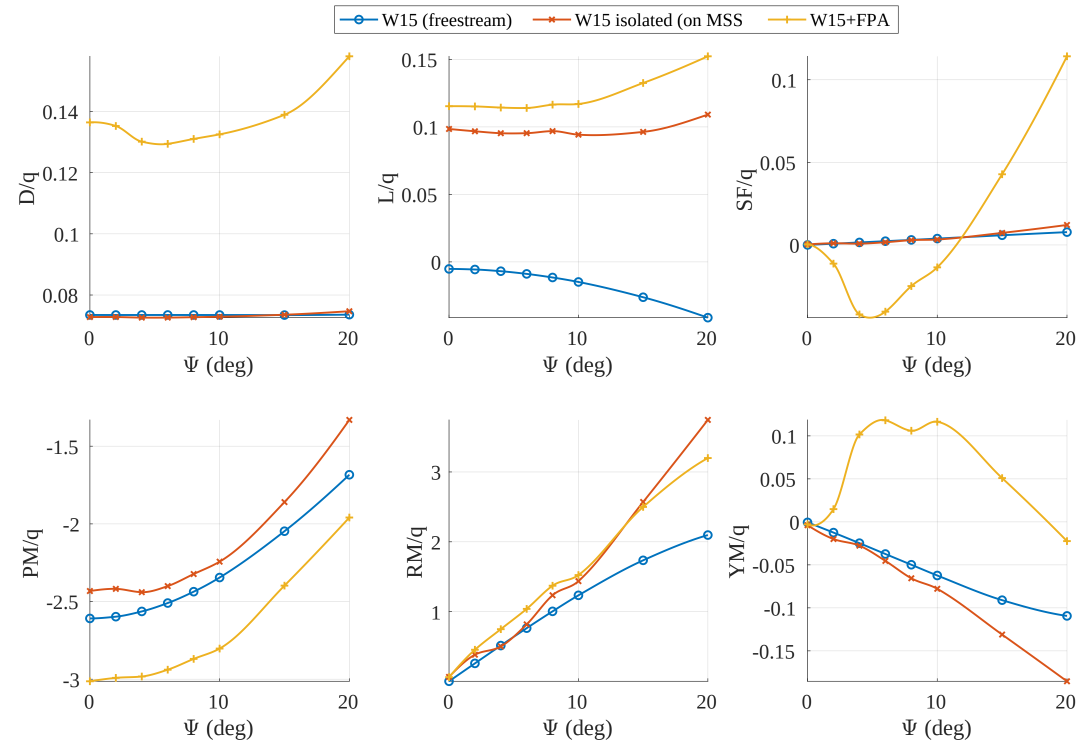

Figure 4.24: Yaw Data of W15 in Freestream and on MSS

most notable differences are in lift, drag, and pitching moment, which explain the differences in corrections in Figure 4.27. The difference in interference effects follows the same lift under-estimation pattern as before in the fork validation simulation case, Figure 4.12. The KWT, in its test, also pitched down the disk -0.024 degrees to produce exactly zero lift, noted in the run logs from test UW9733. There is an angle of attack offset, therefore, between different tests and the CFD simulations. Combined with inaccuracies of drag predictions, this affects the lift, drag, and pitching moment correction establishment. An important lesson here is that in any test the reference pitch and yaw positions of the model must be carefully determined and that corrections should be applied in a way that is consistent with those reference angles.

Reflecting on these discrepancies and the data in Figure 4.27, it seems that using the disk yaw T&I corrections from UWAL report 397-B, with a raise in the excrescence drag value of the correction, will be better, for SCALOS test purposes, than the KWT derived yaw correction using the NACA 0015 wing in UWAL report 397-F. This raises the issue, as already has been mentioned above, that the surface quality of the FPA has changed considerably over the decades which in turn affects the effective Reynolds number of the fork airfoils. With the likelihood that these changes may have affected the flow over the FPA, using the

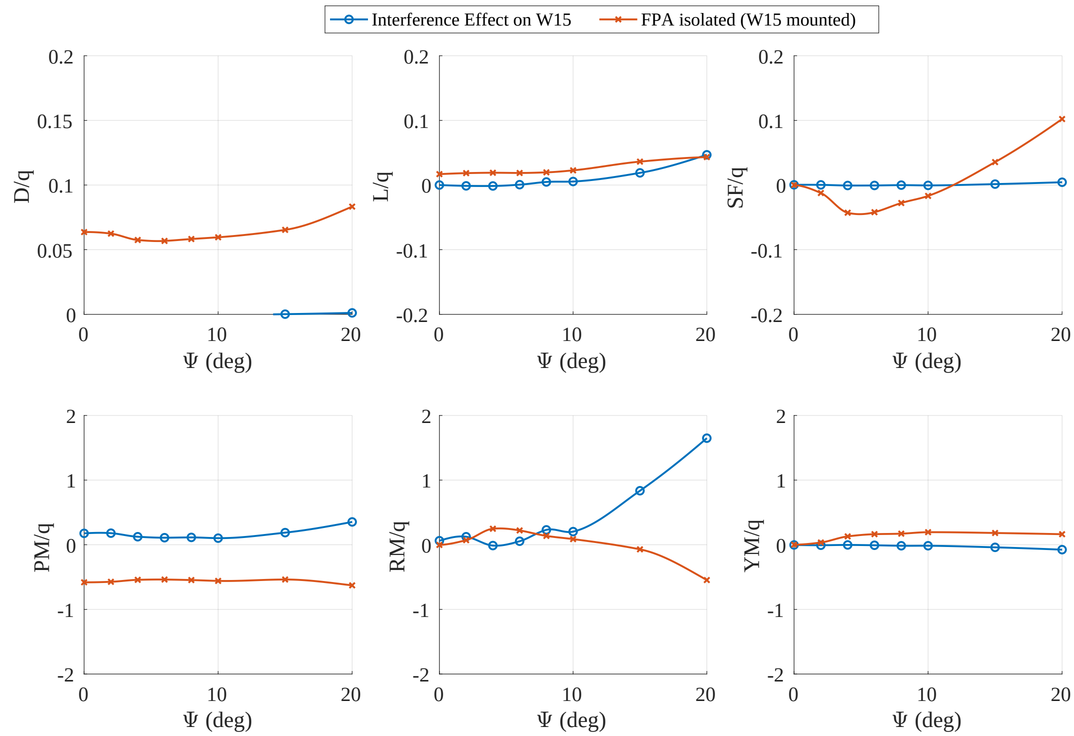

Figure 4.25: Yaw Data of FPA and Interference Between FPA and W15

most recent experimental data of the fork is likely the most accurate approach.

We see in Figure 4.29 that the forces and moments on the FPA vary very little depending on what wing (or disk) is mounted upon it. The reason the W15 case has positive lift is because the wing produced positive lift on the FPA. The same goes for the disk, the disk produced negative lift when mounted to the FPA and thus created negative lift on the FPA. This shows that the body has a negligible interference effect of the FPA forces and moments (especially once reference dimensions are factored in). Therefore, only the interference of the FPA upon the wings/disk needs to be accounted for in the creation of new FPA corrections.

One approach to a final yaw correction for the 2015 wing uses the KWT experimental FPA data with the KWT disk mounted, subtracts the CFD disk and interference forces and moments, and then adds the CFD derived W15 interference effects.

Another approach is to use the KWT experimental FPA-only data with pin fairings attached, subtract the CFD pin fairing forces and moments (interference assumed = 0), then add the CFD W15 interference. Generically; recent KWT data is used with a subtraction of CFD estimated forces and moments of the bodies mounted to derive the new corrections. Both of these hybrid methods are plotted in Figure 4.30. The

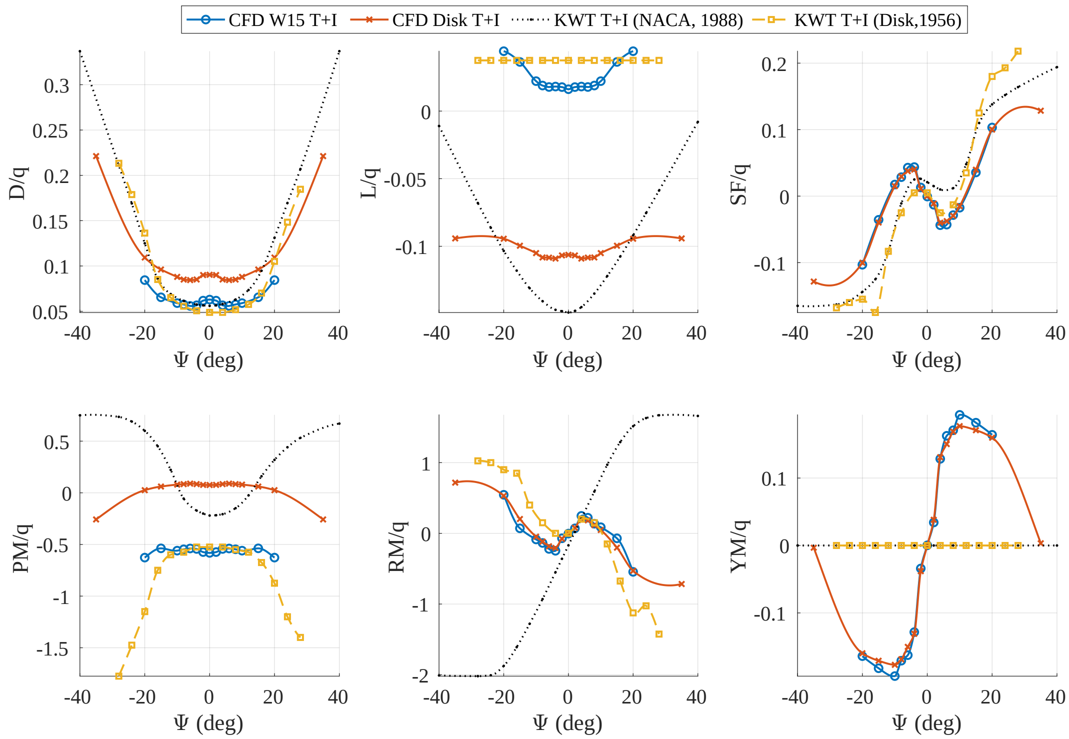

Figure 4.26: Comparison of CFD and KWT W15 Yaw Corrections

differences in the two methods are small. They are different enough from the KWT disk yaw correction from 1956 to consider not using the KWT disk yaw correction.

Evaluating the impact through application to uncorrected KWT data of these yaw based T&I corrections will come in Chapter 7.

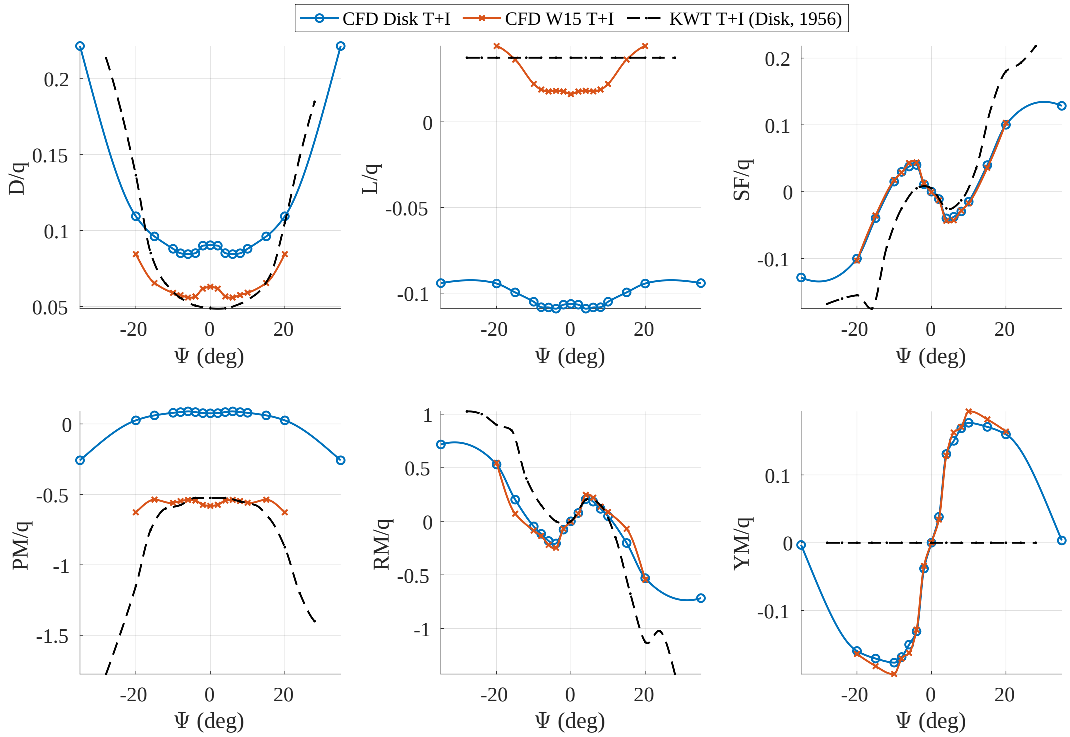

Figure 4.27: Comparison of CFD W15 and Disk Yaw Corrections

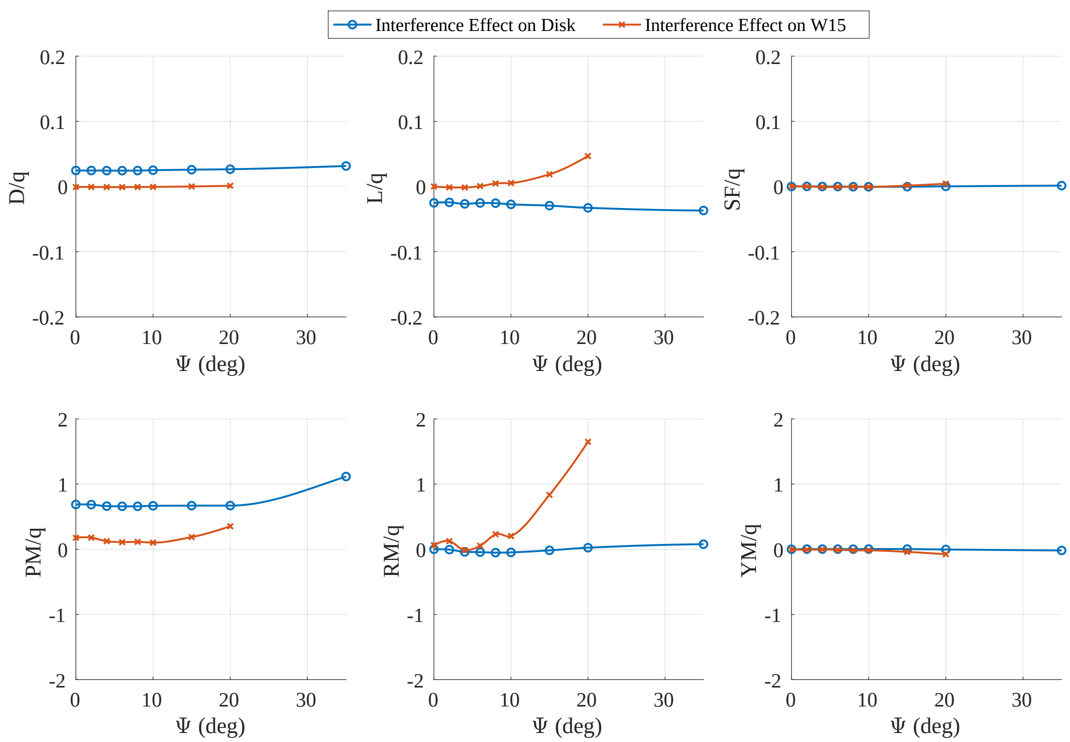

Figure 4.28: Comparison of W15 and Disk Interference

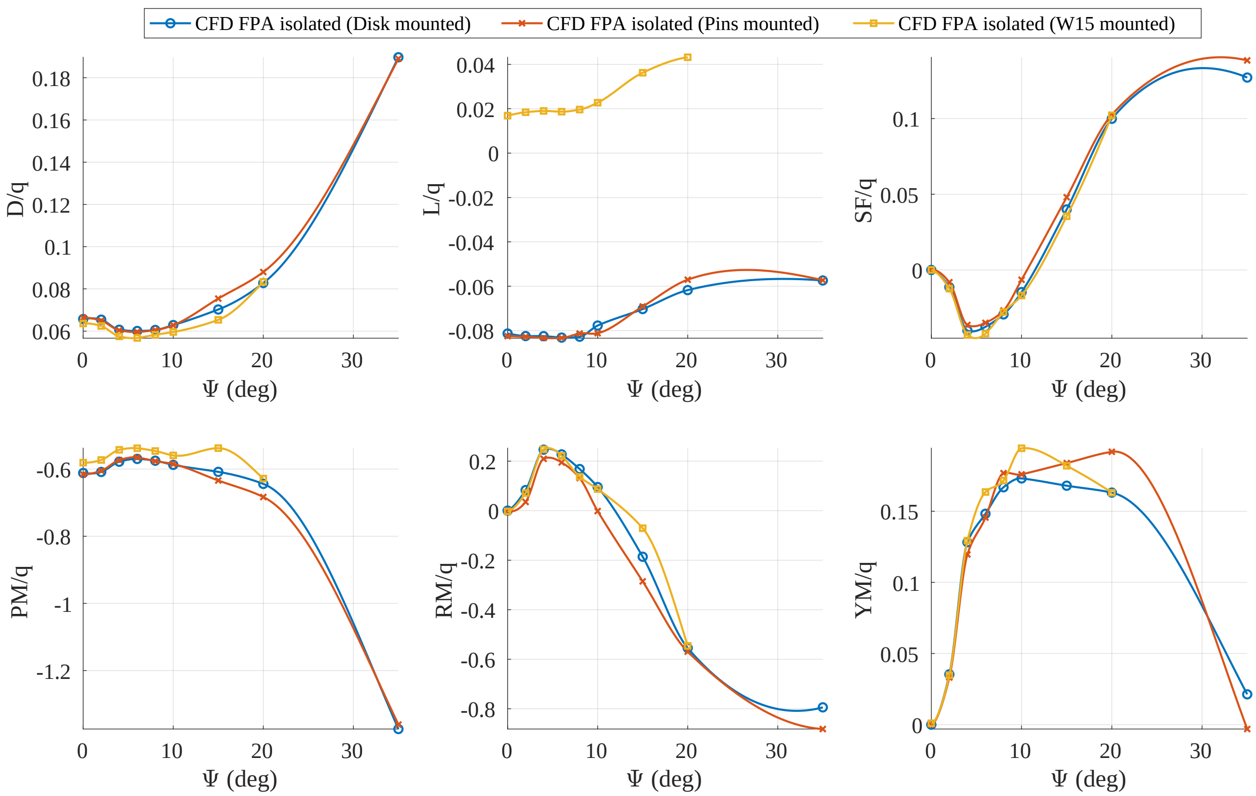

Figure 4.29: Comparison Forces and Moments on the FPA with Various Bodies Mounted - Analysis of Body Induced Interference on the FPA

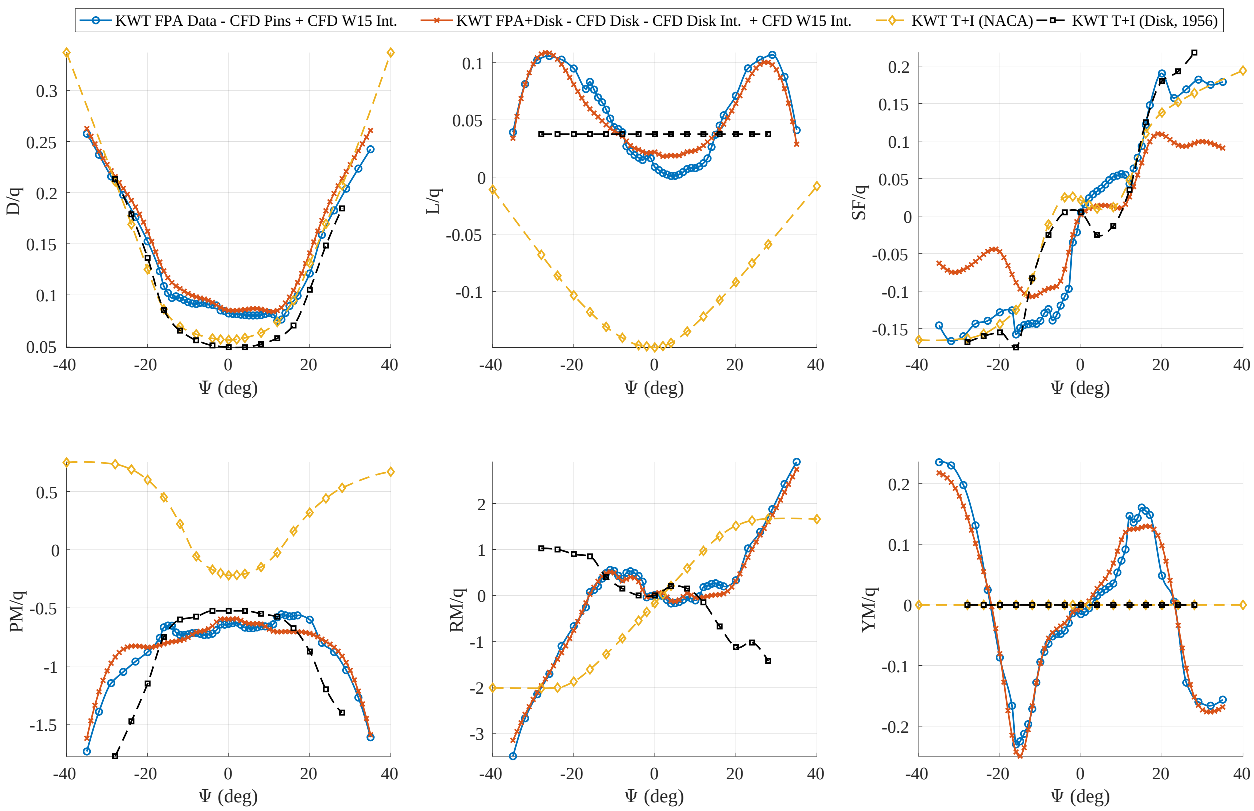

Figure 4.30: Comparison of Hybrid W15 Yaw Corrections to KWT Yaw Corrections

4.3.4 Lift Based T&I Correction using W15

The 2015 wing was simulated in freestream air conditions and on the Model Support System. The results as functions of angle of attack are shown below in Figures 4.31 to 4.35. Pitching moment data for W15 is typically analyzed at 25% MAC (the MMC) but the corrections are applied at BMC so pitching moment at the BMC is also presented. There is a significant offset in the data curves, especially in lift; plotting the data as functions of lift tells us how much of the affects are due to lift, Figures 4.36 to 4.39.

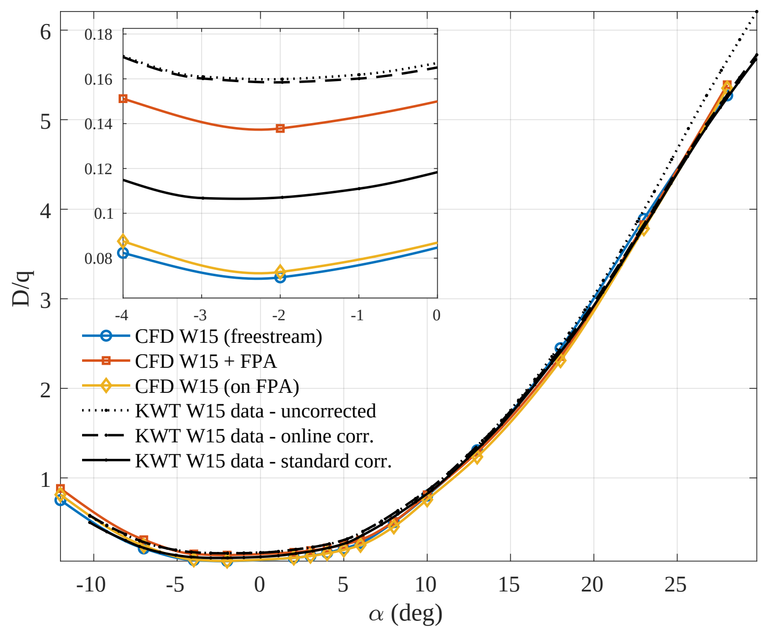

Figure 4.31: W15 Pitch Sweep CFD Results - Drag

Again, the FPA T&I Correction is calculated by subtracting (W15+FPA) from (freestream W15) to include all interference effects. Since the pitch and drag corrections are a function of lift coefficient, the first step in correcting the uncorrected experimental KWT data is to correct for the lift loss due to the fork and interference (about 18 lbs at q = 40 psf), Figure 4.40. This shifts the drag and pitching moment curves to the right in a plot vs wing lift coefficient (adding lift to experimental data). After correcting for the lift, drag and pitching moment can be corrected. Figures 4.36 to 4.38 show that (W15+FPA) data closely follows freestream W15 data. The figures may be somewhat misleading because the lift needs to be corrected.

The CFD results suggest that the shift in lift is larger than what is currently used with the standard KWT FPA T&I corrections (created with the NACA wing in 1988). However, recalling the questionable negative

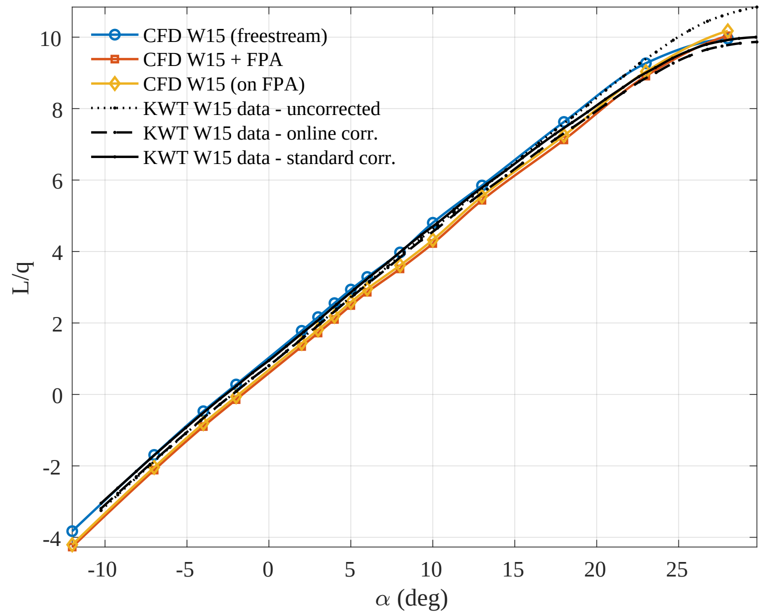

Figure 4.32: W15 Pitch Sweep CFD Results - Lift

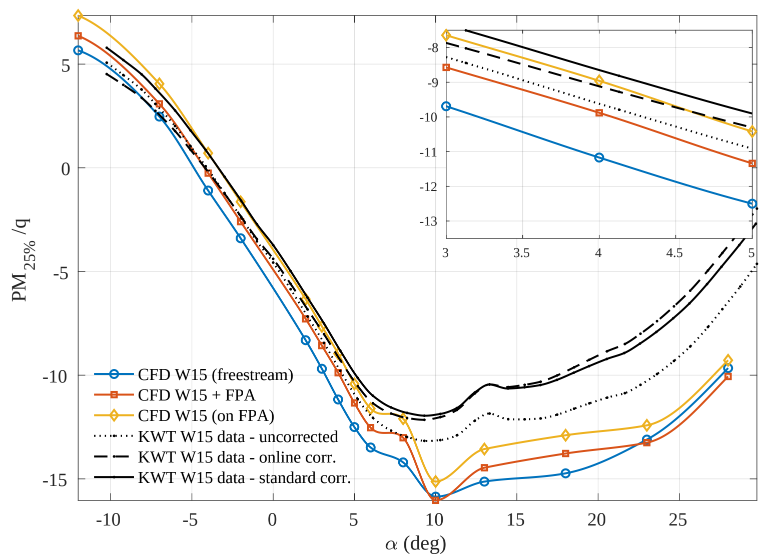

Figure 4.33: W15 Pitch Sweep CFD Results - Pitching Moment at 25% MAC

lift estimates in Figures 4.12 to 4.14, this result must subject to further scrutiny in Chapter 7. This larger lift shift in the curves impacts the drag and pitching moment corrections. The drag corrections becomes negative, i.e. adding thrust, after $C_{L_W} = 0.667$, apparent in Figures 4.36 and 4.42.

For the pitching moment, corrections were evaluated as the mean value across lift coefficient values less than one because those larger than one presumably have much separated flow. We see here that the lift

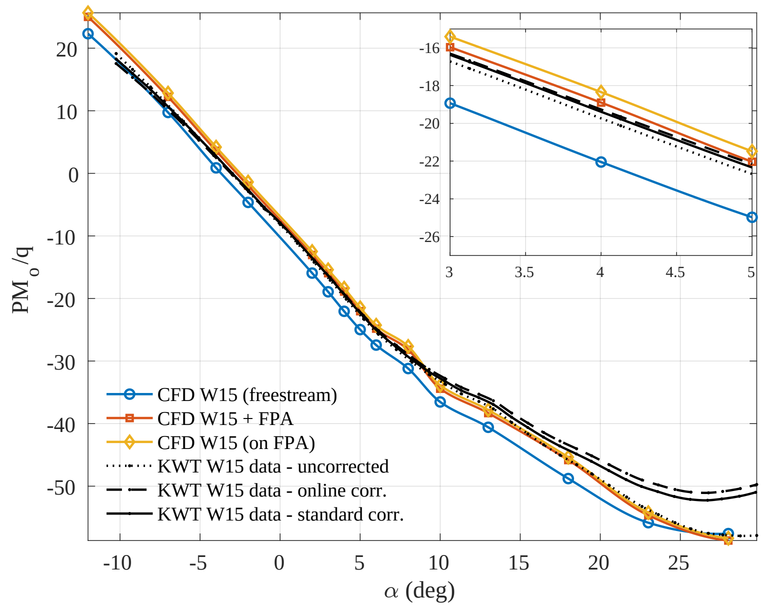

Figure 4.34: W15 Pitch Sweep CFD Results - Pitching Moment at Origin (PMO)

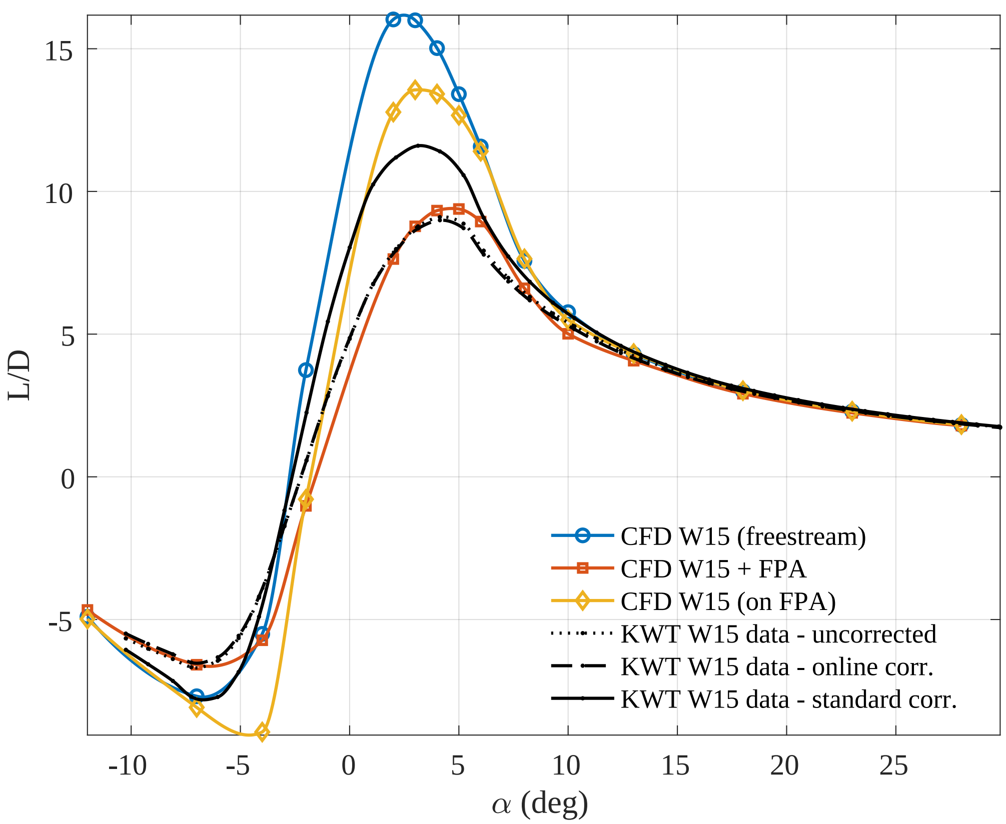

Figure 4.35: W15 Pitch Sweep CFD Results - Lift to Drag Ratio

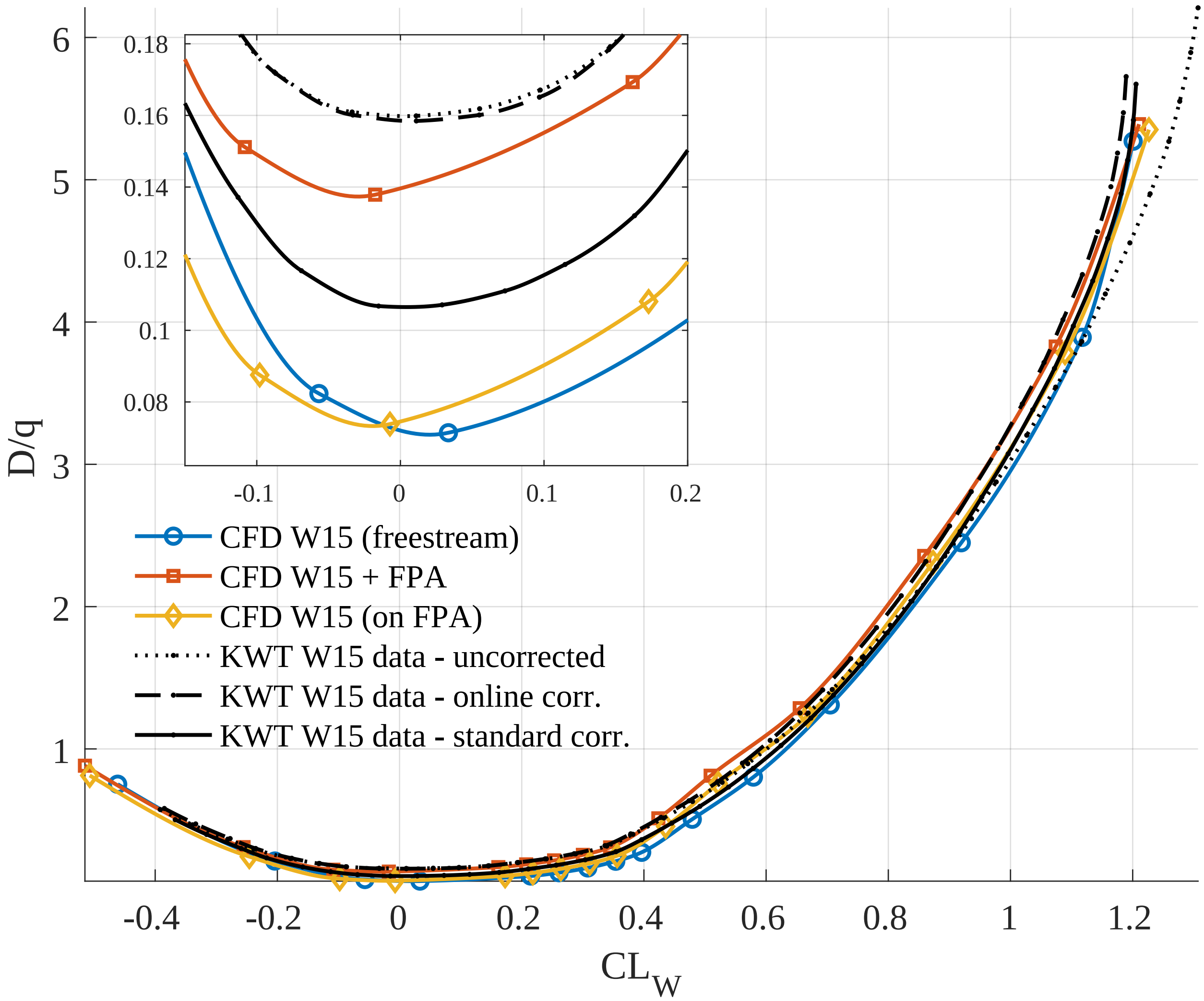

Figure 4.36: W15 Pitch Sweep CFD Results - Drag

corrections for W15 do not correlate well with the lift corrections for the rectangular NACA 0015 wing. This greatly impacts the final data delivered by the KWT when it uses its "standard" corrections.

Evaluating the impact through application to uncorrected KWT data of these lift based T&I corrections will come in Chapter 7.

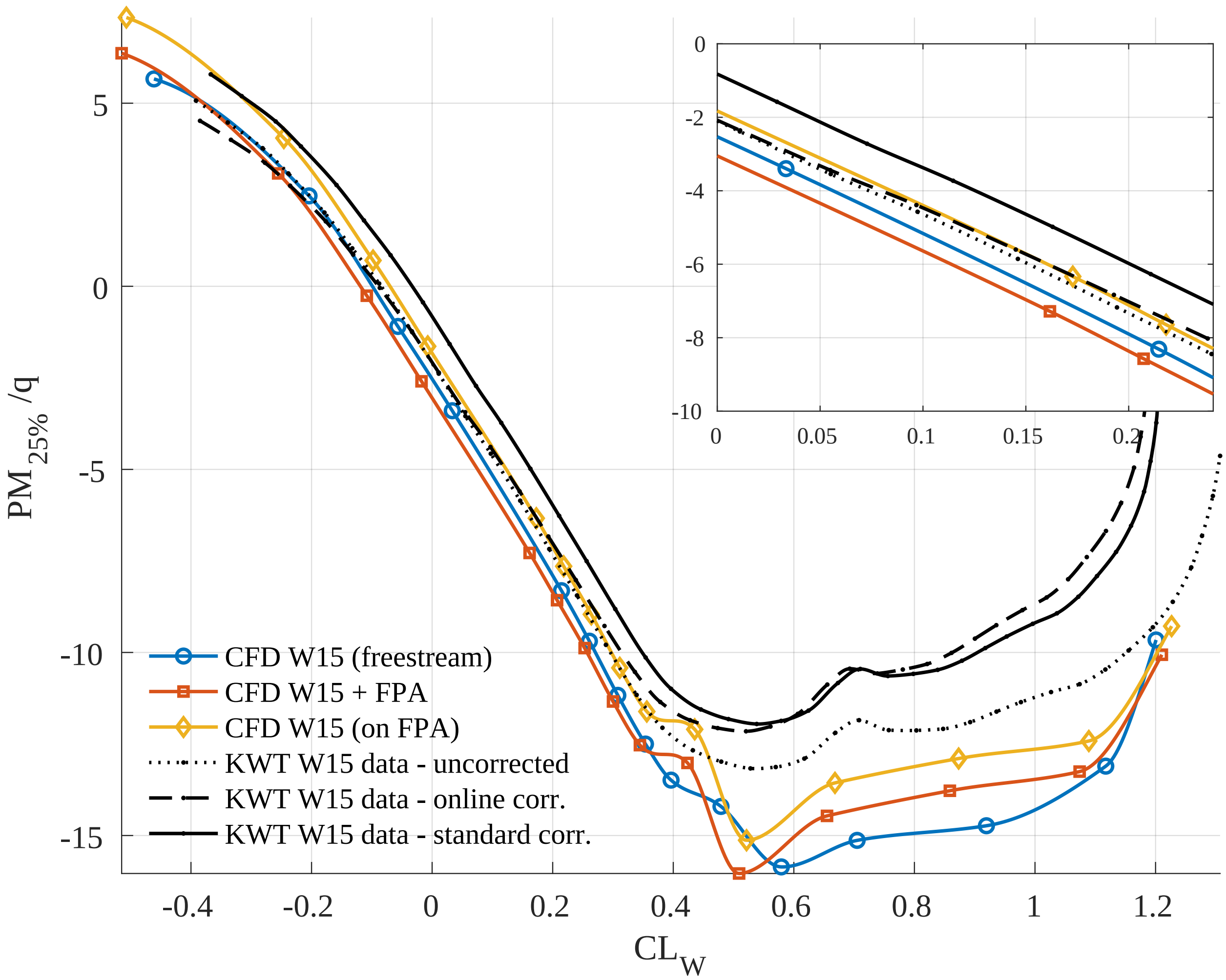

Figure 4.37: W15 Pitch Sweep CFD Results - Pitching Moment at 25% MAC

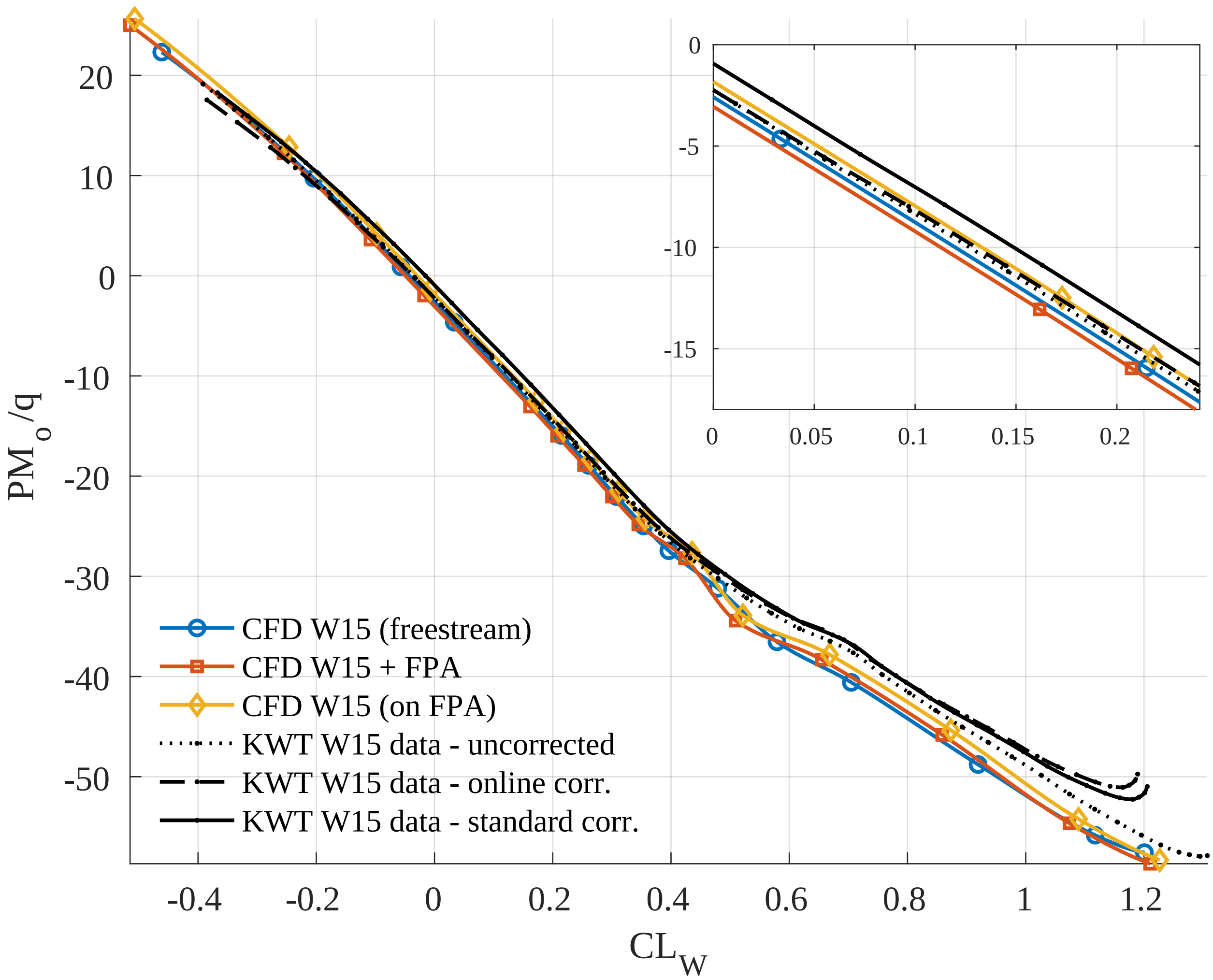

Figure 4.38: W15 Pitch Sweep CFD Results - Pitching Moment at Origin (BMC)

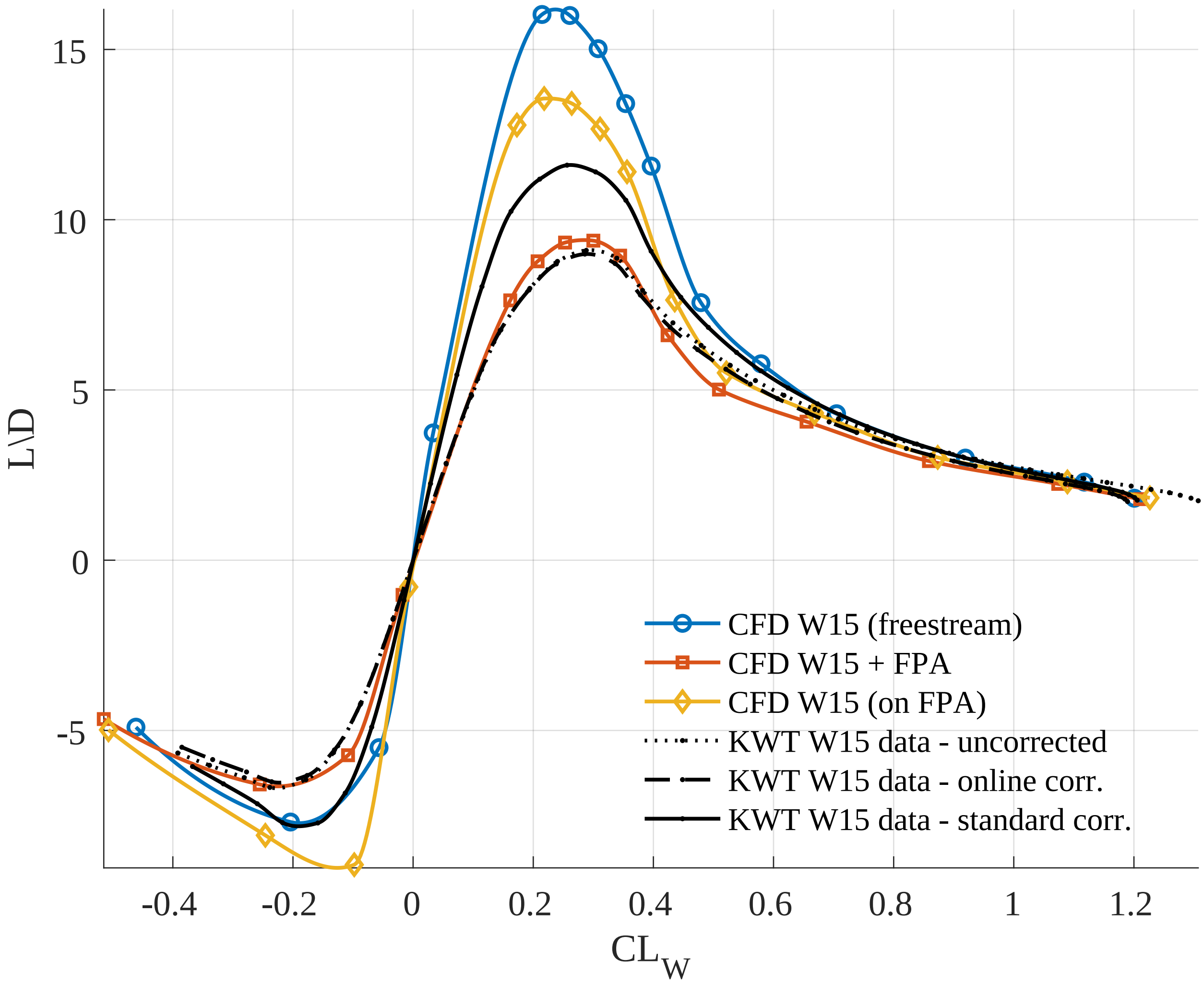

Figure 4.39: W15 Pitch Sweep CFD Results - Lift to Drag Ratio

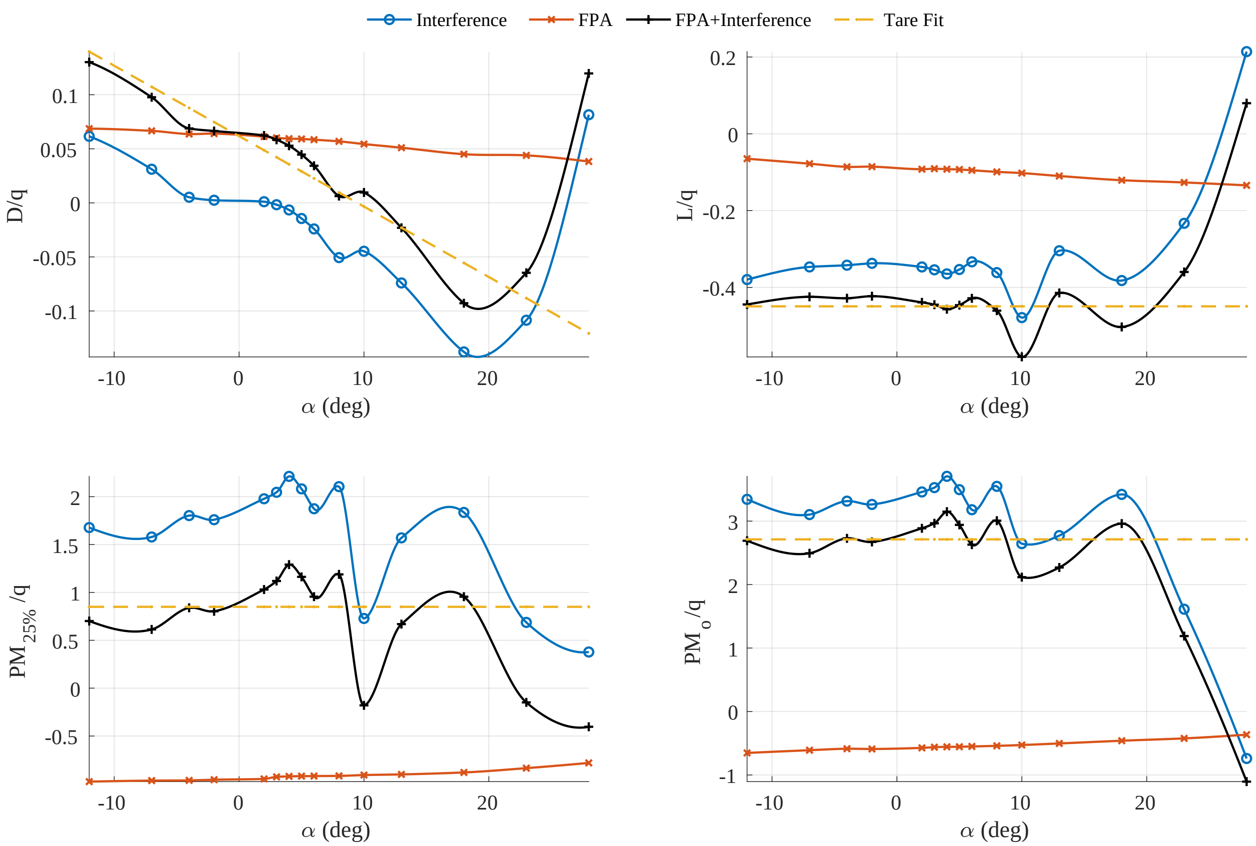

Figure 4.40: Interference, Fork and Pitch Arm Data, and Lift Corrections

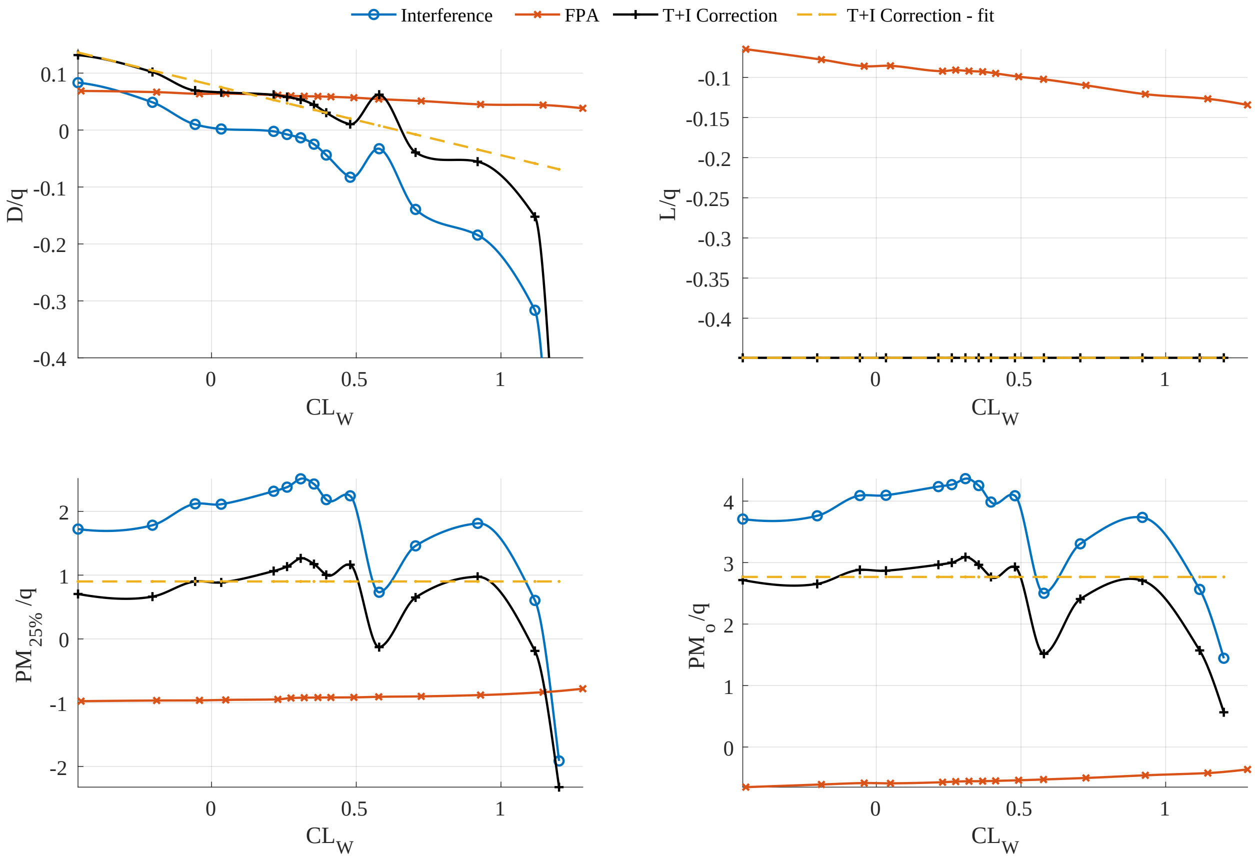

Figure 4.41: Interference, Fork and Pitch Arm Data, and Lift Corrections

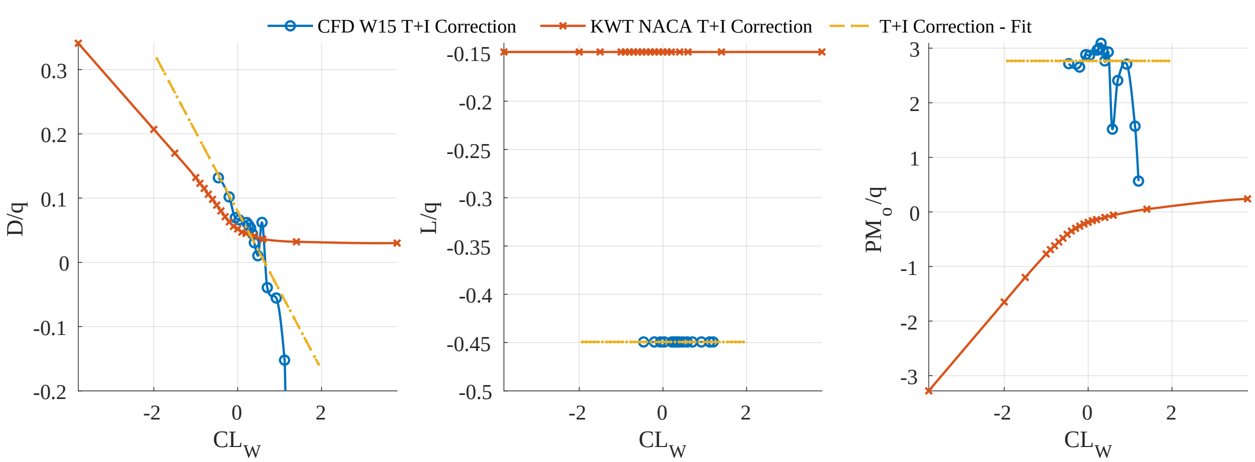

Figure 4.42: W15 CFD Corrections Compared to KWT NACA Wing Corrections

4.4 Fork Excrescence Drag Evaluation

Important information that the CFD simulations tell us is that the excrescence drag, $C_{D_{min}}$, of the FPA along with the interference on the model (and model on the FPA) is higher than what the original KWT reports and corrections predicted. The original KWT corrections include 67.5 counts of drag at zero lift and zero yaw angle (for W15 reference dimensions and q = 25+ psf), yet calculation with CFD and recent KWT data suggest the drag count should be significantly higher. Figure 4.43 helps visualize the lack of drag correction from the KWT. In this figure, drag from CFD simulations is shifted up 25 counts so the (W15+FPA) curve overlaps the KWT online data. The CFD freestream data is notably below the drag minimum from the corrected KWT data. Even the CFD drag estimations of the FPA itself, which has already proven to be a low estimation of the experimental FPA data, is about 12 counts larger than the KWT Standard T&I drag correction, Table 4.1.

FPA under	**CFD Fork CDo**
Pins	**0.007995**
Disk	**0.007957**
W15	**0.007659**

Table 4.1: FPA CFD Drag (q = 40 psf)

To more accurately calculate the FPA drag (at zero lift and sideslip), CFD incremental data (body drag + FPA induced interference) was subtracted from KWT experimental data for the three mounted bodies, i.e. the W15, the disk, and the pin fairings.

The CFD simulation of the disk in free stream air (at 40 psf dynamic pressure) yields a value of 0.722 lbf (21.77 counts) and a total drag of 0.973 lbf, yielding a form factor of 1.343 Considering the slenderness of the disk ($\sim$1% t/c), with a thickness to diameter ratio of 0.0104, a low form factor closer to 1.1 was expected. Extending all of the edges 2 inches with lenticular cross sections and deleting the blisters on the disk, reduced the form factor to 1.075.

Looking elsewhere for data to validate or reject the CFD derived form factor, a 1.35-1.4 form factor was estimated by using Kamaruddin's rounded edges disk excrescence drag values [23] with AGARD excrescence Reynolds number correction for drag [24]. Not only does this information validate the use of CFD simulations for derived form factors, it also validates the increments developed for the disk edge effects of

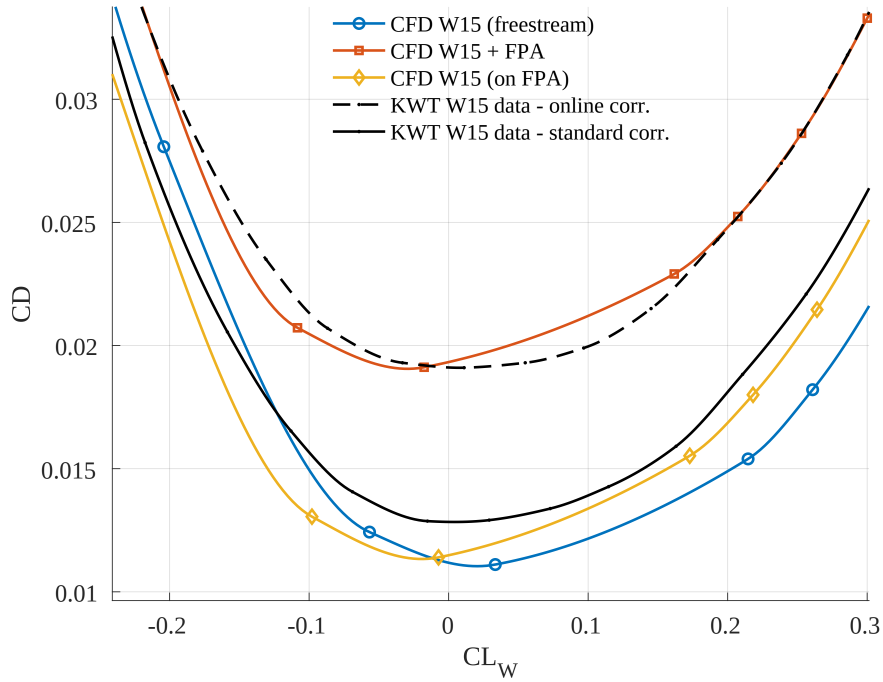

Figure 4.43: W15 and FPA Pitch Sweep CFD Results - FPA Excrescence Drag Close-up (q = 40 psf)

the CFD.

The calculations, Table 4.2 suggests a fork mount drag correction be between 99.7 and 103.1 drag counts, therefore the median value of 101 counts was settled upon as the final fork mount excrescence drag value for the new, CFD-derived T&I drag correction. This is 33.5 counts more than the current KWT drag correction. With this information, this incremental difference, the KWT Standard T&I drag correction may be corrected simply by shifting the drag values up.

Evaluating the impact of these yaw based T&I corrections through application to uncorrected KWT data will come in Chapter 7.

KWT Data		-	CFD Data		=	**Fork CDo Tare**
FPA+Pins	0.011289	-	Pins+Int	0.001320	=	**0.009968**
FPA+Disk	0.015070	-	Disk+Int	0.004756	=	**0.010311**
FPA+W15	0.019090	-	W15+Int	0.008887	=	**0.010203**

Table 4.2: FPA Excrescence Drag Evaluations (q = 40 psf)

Chapter 5

Wall and Blockage Corrections

5.1 Correction Calculation

The incremental CFD and KWT wall and blockage corrections are defined as positive additions to uncorrected data (the opposite as that done for T&I corrections), i.e.

$$C_{x_{corrected}} = C_{x_{uncorrected}} + \Delta C_x \tag{5.1}$$

The CFD-based blockage and wall effect corrections are found using CFD simulations of the W15 model wing in freestream conditions and in the test section:

$$\text{Wall + blockage effects = (W15 in test section) - (W15 freestream)} \tag{5.2}$$

These effects are investigated for both the longitudinal and lateral cases, independently, and are compared to Kirsten Wind Tunnel "Shindo's Simplified Blockage Correction" which follow classic wall correction methods [25]. The UW SCALOS tests at the KWT use Shindo's Simplified Blockage Correction (the standard KWT wall and blockage corrections), as directed from the 2020 UWAL (Kirsten Wind Tunnel) Test Letter and wall correction constants were copied from the 2020 test letter.

5.1.1 Shindo's Simplified Blockage Correction

Following the order of correction applied to KWT uncorrected data, Figure 2.3, the first correction is the dynamic pressure correction:

$$q_c = q_a(1+\epsilon)^2 \tag{5.3}$$

where the c subscript denotes corrected and the a subscript denotes actual, where "actual" dynamic pressure is the KWT's term for dynamic pressure corrected by a factor from the measured dynamic pressure in the wind tunnel. The correction factor, ϵ is defined as:

$$\epsilon = \frac{S_W}{C_A}[C_D - C_L^2(\frac{1}{\pi AR} - \delta_w \frac{S_W}{C_A})] \tag{5.4}$$

where δ_w is the wing wall corrections factor based on the wing dimensions and calculated by the KWT. C_A is the actual cross-sectional area of the test section including the effects of the corner fillets, 91.5 ft^2. Aspect ratio, AR is specifically calculated as; $AR = b^2/S_W$. All force and moment coefficients are then re-calculated using q_c.

The next correction is the flow angularity correction where the angle of attack is corrected by amount of upflow once measured in the tunnel; $\Delta\alpha_u =$ -0.012 deg.

Then the wall corrections are applied:

$$\Delta\alpha_{wc} = 57.3 \text{ rad/deg} \cdot \delta_w(\frac{S_W}{C})C_{L_W} \tag{5.5}$$

$$\Delta C_{M_{wc}} = 57.3 \text{ rad/deg} \cdot \delta_{A_S}\frac{\partial C_M}{\partial \delta_S} \cdot (\frac{S_W}{C})C_{L_W} \tag{5.6}$$

C_{L_W}, the coefficient of lift for the wing is obtained from a tail-off run of the same wing configuration, known as a Lift Set. $\partial C_M/\partial \delta_S$ is obtained from three runs with different stabilizer angles, known as a CMS set. C is the test section cross-sectional area neglecting fillets; 96 ft^2.

The flow angularity corrections differences are then applied to the force and moment coefficients of the model.

$$\begin{bmatrix} C_{L_{WA}} \\ C_{D_{WA}} \\ C_{Y_{WA}} \\ C_{M_{WA}} \\ C_{R_{WA}} \\ C_{N_{WA}} \end{bmatrix} = \begin{bmatrix} cos(\Delta\alpha_u + \Delta\alpha_{wc}) & sin(\Delta\alpha_u + \Delta\alpha_{wc}) & 0 & 0 & 0 & 0 \\ -sin(\Delta\alpha_u + \Delta\alpha_{wc}) & cos(\Delta\alpha_u + \Delta\alpha_{wc}) & 0 & 0 & 0 & 0 \\ 0 & 0 & 1 & 0 & 0 & 0 \\ 0 & 0 & 0 & 1 & 0 & 0 \\ 0 & 0 & 0 & 0 & cos(\Delta\alpha_u + \Delta\alpha_{wc}) & sin(\Delta\alpha_u + \Delta\alpha_{wc}) \\ 0 & 0 & 0 & 0 & -sin(\Delta\alpha_u + \Delta\alpha_{wc}) & cos(\Delta\alpha_u + \Delta\alpha_{wc}) \end{bmatrix} \begin{bmatrix} C_L \\ C_D \\ C_Y \\ C_M \\ C_R \\ C_N \end{bmatrix} + \begin{bmatrix} 0 \\ 0 \\ 0 \\ \Delta C_{M_{wc}} \\ 0 \\ 0 \end{bmatrix} \tag{5.7}$$

Since this case involves only the wing and no horizontal stabilizer, $\Delta C_{M_{wc}}$ and $\partial C_M/\partial\delta_S$ are taken to be zero. Including them makes no difference, quantitatively.

However, the method of adding Shindo's blockage with the wall corrections to KWT uncorrected data does not validate the standard data provided by the KWT. The coefficients in the test letter may be old, classical blockage corrections may have been used, and/or another unknown may be at cause. Additionally, the difference between online data (all corrections except the FPA T&I correction, i.e. blockage, tunnel flow angularity, and wall corrections applied) and uncorrected data is analyzed. This calculation gives the true, applied, incremental difference of the wall, blockage, and flow angularity corrections.

The values taken from 2020 test letter:

- $dC_M/d\delta_s$ = -0.0088
- δ_w = 0.11422
- δ_{as} = 0.0843

5.2 CFD Simulation Setup

The same standard mesh settings were used from the mesh refinement study on W15 and the same physics settings were used from the physics study, both of which are in Section 3.1.1. However, for the simulations modeling the W15 in the test section, the inlet was modeled as a velocity inlet and the outlet as a pressure outlet at the suggestion of Rodriguez [14]. The walls of the test section were given a slip condition. The thickness the boundary layers of the walls in the test section and where they start is uncertain. Modeling no boundary layer on the wall simplifies the problem while retaining the majority of the wall effects and drastically reduces the mesh and computation cost. Both sets of models, freestream and in the simplified KWT test section, had a volume cell count of approximately 8.3 million cells for a half model.

The KWT test section dimensions were taken from Figure 2.2. The front and end cross sections of the test section were extended 20 ft to help CFD convergence. Results were checked (in the $\alpha = 30^o$ simulation) to make sure pressure gradient contours did not reach the velocity inlet.

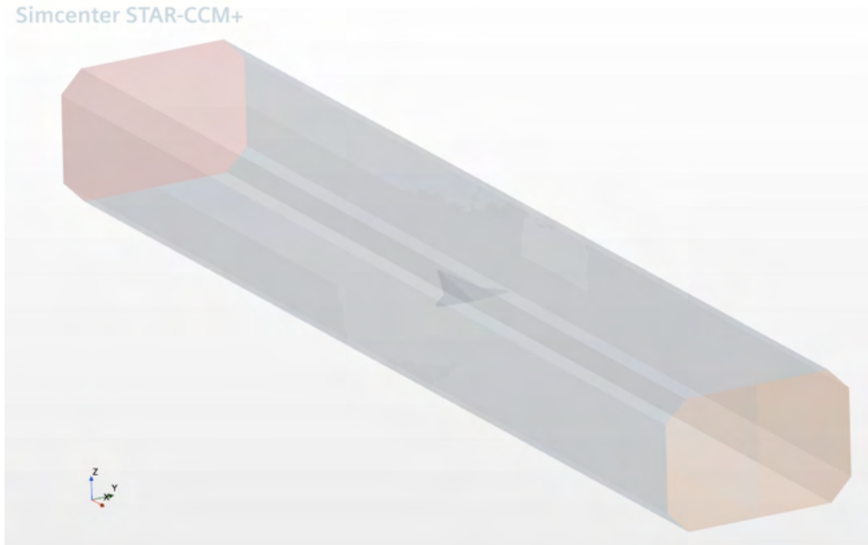

Figure 5.1: Model of W15 in KWT Extended Test Section Walls

5.3 Results

Results from the two sets of simulations: W15 in freestream and W15 within the KWT walls. Those are presented in Figure 5.2 and 5.3. The reader should note the large data asymmetries in the data from the KWT, this is probably be due to the data asymmetries seen on the fork mount - a result of asymmetry of the fork mount itself. Figure 4.13.

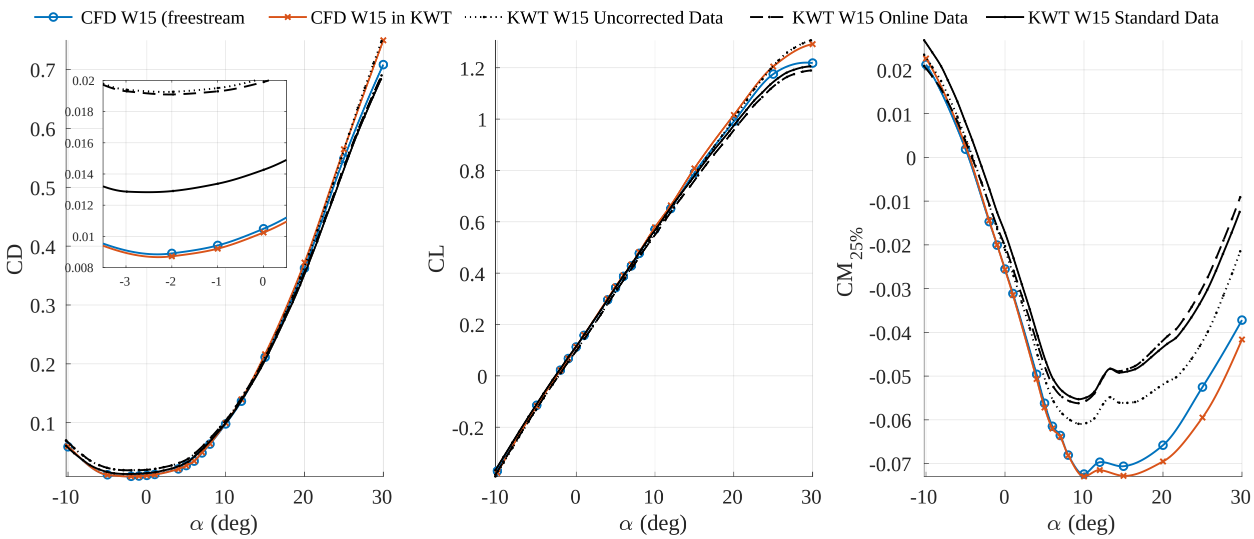

Figure 5.2: CFD Results and KWT Data of W15 in KWT Test Section vs. α

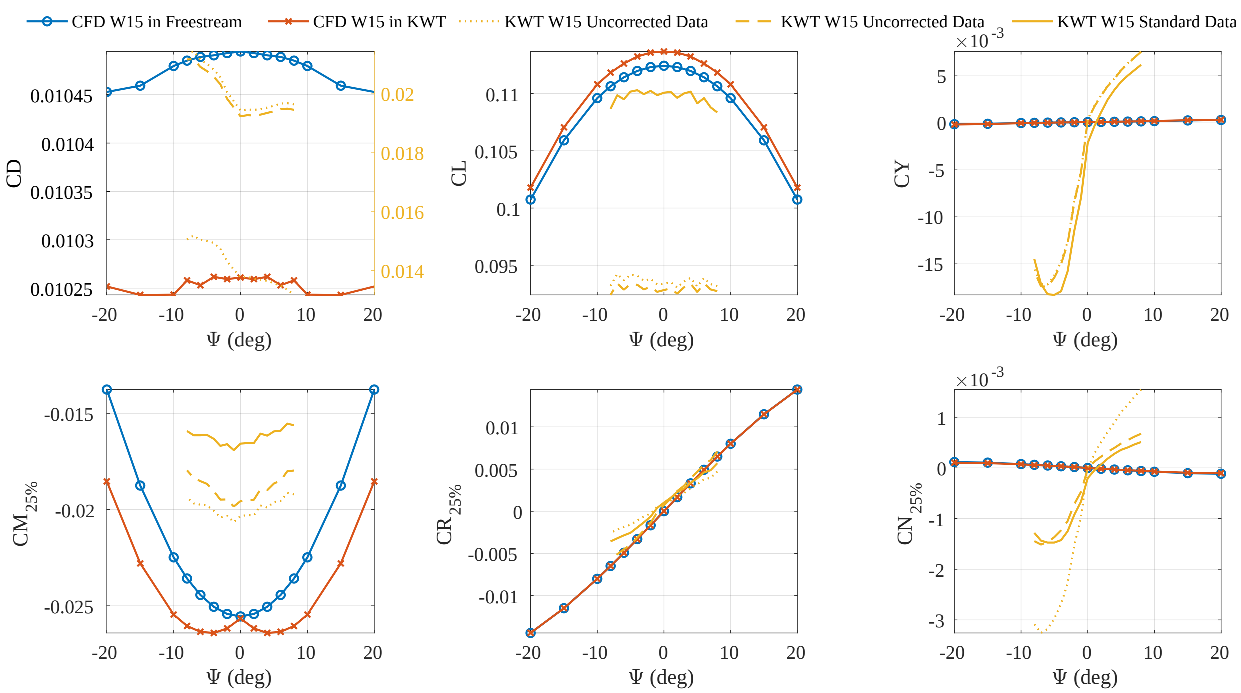

Figure 5.3: CFD in KWT Walls Results vs. Ψ

5.4 Comparison to KWT corrections

The blockage and wall effects are shown in Figure 5.4 and 5.5. Again, two sets of KWT corrections are shown: the theoretical correction of Shindo's Simplified Correction, and the real correction applied calculated by the difference between uncorrected data (does include balance interactions and model weight tares) and Online Data (partially corrected data - only omitting the FPA T&I correction).

The CFD incremental correction trends better match the KWT applied corrections for drag and lift. However, the CFD correction trends better match Shindo's correction with great agreement of the slope of the curve in the linear flight regime. An investigation on the reason for the differences between the theoretical (Shindo) corrections and the applied corrections needs to be done by the SCALOS team. From here on, the CFD corrections will be directly compared to the **applied** KWT wall and blockage corrections.

Some of the differences between the CFD and applied KWT corrections may be attributed to the presence of the MSS in the KWT test section during KWT tests, which was not modeled by the CFD free-stream and within-walls runs. There are large asymmetries in the sideslip KWT data blockage and wall effect increments and the difference from the CFD-based corrections is significant. The reason may be, again, the asymmetry of the actual fork and pitch-arm hardware versus the symmetric CFD model plus effects of the pylon and form that were not included in the in-section CFD simulations for wall and blockage effects. In addition, the configurations that were used by the KWT to develop its wall and blockage corrections were quite different from the W15 configuration used for the CFD corrections [25].

The applicability of the KWT derived wall and blockage corrections for a full model, i.e. tail, fuselage,

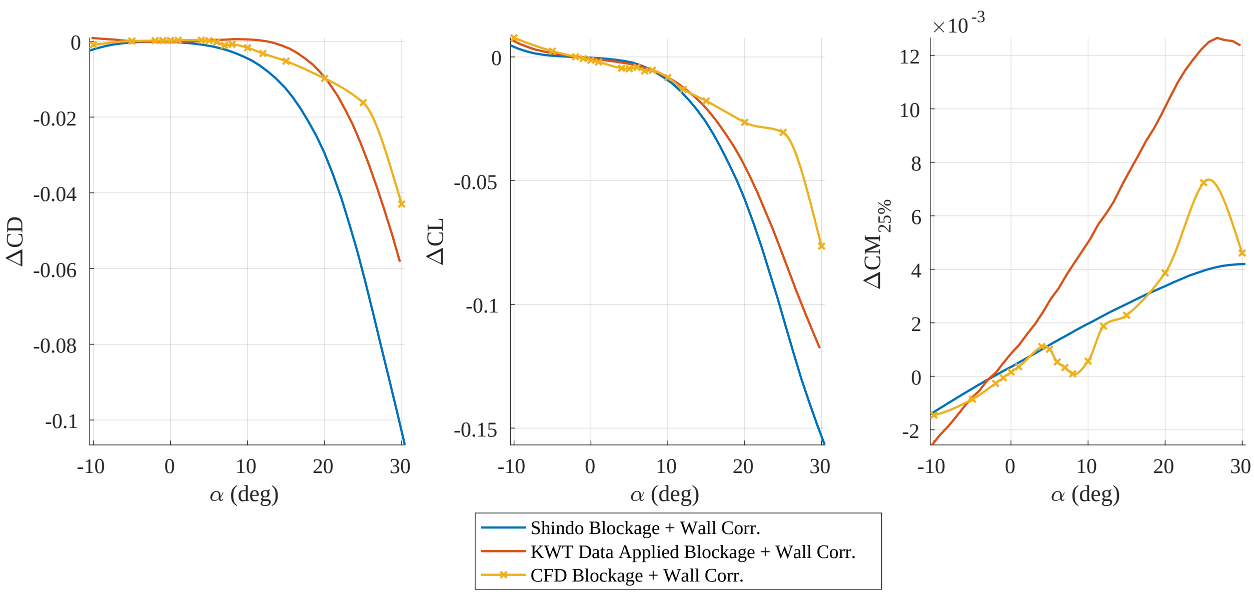

Figure 5.4: Incremental Blockage and Wall Effects vs. α

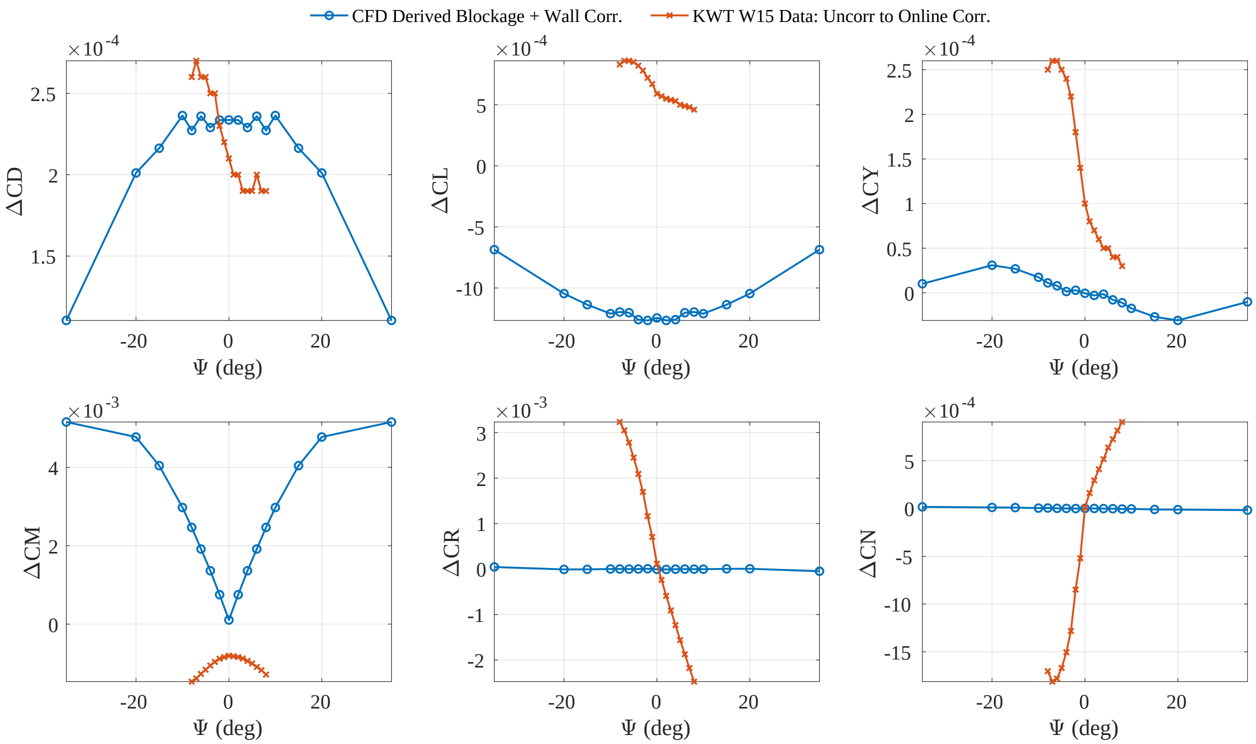

Figure 5.5: Incremental Blockage and Wall Effects vs. Ψ

Chapter 6

Nacelle Interior Drag Corrections

6.1 Introduction

The wind tunnel model's engine nacelles are hollow (flow-through). The forces created by the contact of flow with the inside surfaces of the nacelles must be taken into account and removed from the test data of the model since the effect will not be present on the actual airplane, where the inside flow through the engines will be modeled by the math models of the propulsion system and its integration with the airframe. Theoretically, the effect of this internal drag can be measured in the tunnel by testing with flow-through nacelles and with nacelles that are sealed and that are bounded by streamlines forward and aft solid bodies, but those forward and aft inserts would also contribute to drag and other loads. This section describes how CFD is used in this work to account for the model nacelles' flow-through effect.

Calculating a form factor for the nacelles is a convenient and clever method to estimate the friction drag on the nacelle internal duct without relying *directly* on the skin friction drag results provided by CFD simulations. Rather, calculating the factor in which drag has changed allows the use of handbook or experimental equations, such as the Prandtl friction coefficient for turbulent flow (Equation (3.9)) to more accurately calculate the drag inside of the nacelles. While imperfect, this has a modest uncertainly on this relatively small % of total configuration drag is not that significant for a low-speed test.

6.2 Setup

The nacelle simulations use the same mesh settings as the W15 standard settings and use the Spalart-Allmaras turbulence model. The internal area of the 2020 nacelle was found, using the CAD package NX, to be 158,831 mm^2 (or 246.19 in^2), with a length of 528 mm (20.79"). This area is mathematically opened and flattened into a flat plate with the same area. With this, comparisons of the drag of the inside of the flow-through nacelle and a flat plate can be made and the results can be translated into a form factor that would convert the friction of a flat plate of the same area as the inside of the nacelle to the drag contribution of the flow-through flow tube. The plate model has equivalent length and area and is perfectly flat (2D). The two models are shown in Section 6.2.

The form factor is calculated as:

$$\text{Form Factor} = \frac{\text{Nacelle Internal Friction Drag}}{\text{Plate Friction Drag}} \tag{6.1}$$

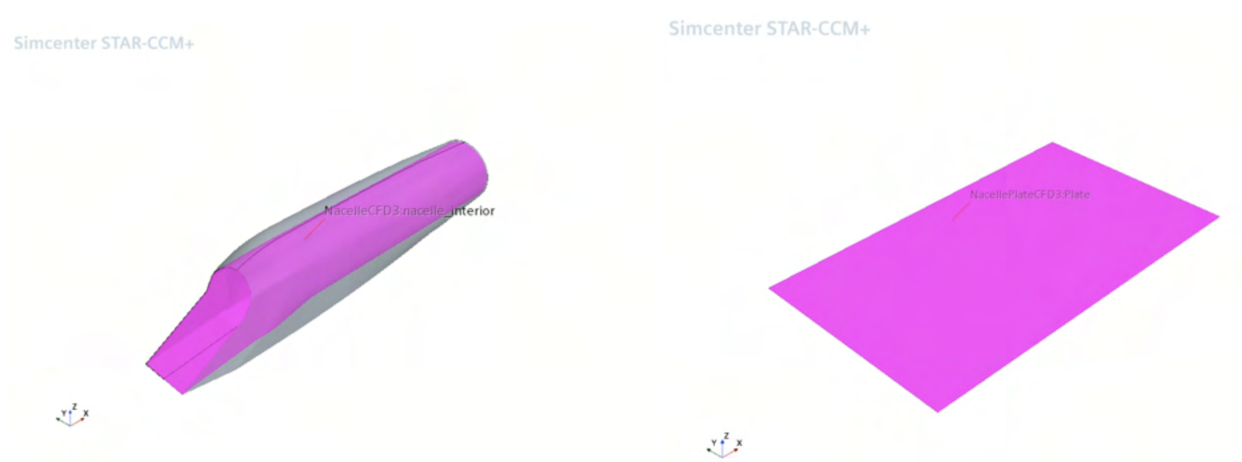

(a) Interior Nacelle Area **(b)** Equivalent Plate Area

Figure 6.1: Nacelle Model Definitions

6.3 Results

The variation of nacelle form factors with the dynamic pressure of the incoming flow is shown in Figure 6.2. The trend of the form factor appears logical considering how boundary layer height decreases as Reynolds number increases, effectively decreasing the effective nacelle cross-sectional area and increasing flow velocity. The interior area of the nacelle produces about 88.8% of the drag (in the nacelle axial direction) compared to the equivalent area plate at a dynamic pressures of 40 psf. Shear drag and coefficient of friction equations were given earlier in Section 3.1.1, Equations (3.9) and (3.10). The nacelle centroids and centerline vectors are given in Table 6.1 for both top and bottom mounted nacelles on at 0^o angle of attack for W15. Centroid coordinates are relative to BMC.

Mount	Centroid (in)	Centerline Vector
Top	(17.705, $\pm$ 6.965, 1.919)	$\left\langle \cos(-5.2^o) , 0, \sin(-5.2^o) \right\rangle$
Bottom	(17.321, $\pm$ 6.982, -3.020)	$\left\langle \cos(0.75^o) , 0, \sin(0.75^o) \right\rangle$

Table 6.1: Top and Bottom Nacelle Centroid Coordinates and Centerline Vectors

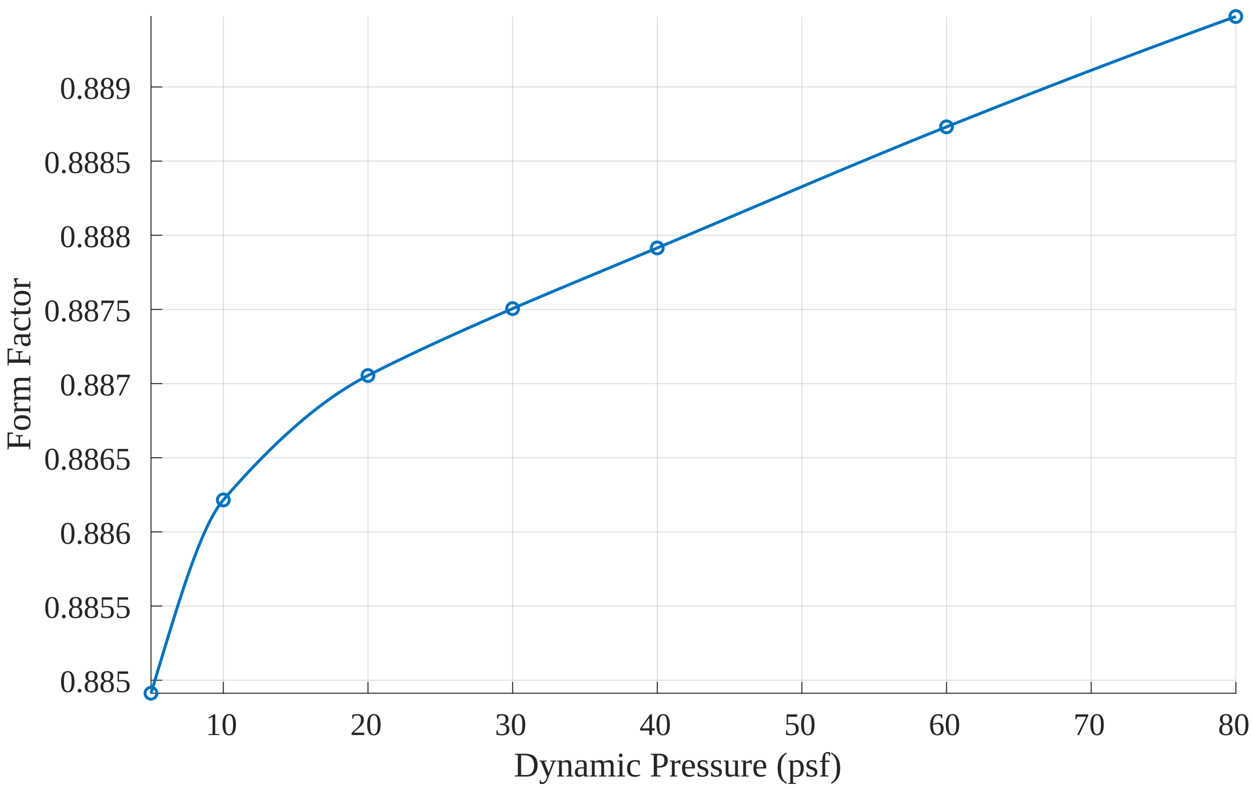

Figure 6.2: Nacelle Form Factor vs Dynamic Pressure

Chapter 7

The Application of All Corrections

This chapter presents a comparison of wind tunnel test results corrected by the CFD derived corrections to wind tunnel test results corrected by the standard KWT-derived correction KWT and to CFD freestream simulations. The purpose of wind tunnel corrections is, after all, to produce results for the "free flying" model based on the measured raw wind tunnel test results. From the start, the overall goal of this work was to evaluate, using CFD simulations, the standard corrections that the KWT has been using for the fork mount, its fairing, and its walls, and to replace the standard KWT corrections by better corrections early in the SCALOS research plan before corrections for SCALOS configurations can be obtained by tests in the KWT using an image fork and fairing system.

Three configurations are analyzed:

1. The 2015 wing-only model (W15)
2. The 2020 Baseline Configuration without flow-through nacelles
3. The 2020 Baseline Configuration with flow-through acelles

The '2020 Baseline' configuration, designated UW-S-20A, has forward positioned 2015 canards, the 2020 wing, the 2020 T-tail, the top mounted 2020 nacelles, and no surface deflections. Recall that this configuration without nacelles was the subject of the physics study in Section 3.2.2.

As has already been discussed, The "standard" KWT corrections are applied sequentially to account for walls, blockage, and the interference with the fork and the fairing of the model support system. All those were investigated separately with the W15 using CFD to evaluate those corrections step by step.

It is important to note here that in essence the overall corrections could be generated by CFD in one step in which results for a model on the fork, in the test section, in the presence of support fairing are compared to the results for the model in the free stream. The work presented here sought to understand and gain insight into each step of the correction process that the KWT has been using. This kind of understanding is important for test campaigns in which because of schedule and funding constraints wind tunnel test data have to be transformed into free flight data quickly, without establishing corrections experimentally by an image system, and without enough time, possible, to mesh and run substantial CFD simulations.

The step by step evaluation of CFD-based corrections was not done for the 2020 baseline configuration.

All KWT test results for the W15 case presented in this section are taken from KWT test number UW 2320. Results for the 2020 baseline configuration are also taken from test UW 2320 but test results for the 2020 Baseline configuration without nacelles are taken from test UW 2331. At the time of writing, the uncorrected data from UW 2331 has not yet been delivered by the KWT.

In the following plots KWT "online data" and "standard data" are presented - the two sets of data the KWT delivers to customers. As has been explained earlier, "online data" is corrected data missing only the model support corrections. This is done to help customers with almost immediate results during a test for the evaluation of trends, key characteristics, problems, etc., and to expedite data visualization while customers are onsite. "Online data" may leave out additional correction factors specified by the customer. "Standard data" accounts for every correction listed in Figure 2.3 and is delivered by the KWT to customers after the test is concluded. Remember, all of the data and results plotted in this chapter is in wind axes since all KWT corrections are applied in wind axes.

What makes these CFD corrections especially difficult to analyze is the fact that we don't know the "true" behavior of each configuration in free flight. All we can do is compare corrected results using two techniques and trying to understand the reasons for the differences. CFD models the aerodynamics of configurations remarkably well for some configurations, knowing whether the differences to experimental data are attributed to experimental corrections or limitations of CFD is not always clear. However, what has been validated earlier in this thesis is the use of increments from CFD, so, while we don't know which is more correct, KWT standard data of CFD results, we can trust the incremental corrections to the KWT uncorrected data. The effects of these incremental corrections, their applicability (when to use them), and how well they compare the CFD freestream predictions are presented in this chapter.

7.1 The W15 Case

7.1.1 Lift

As explained earlier in Section 2.1, the order in which corrections are applied can make a difference. The figures below show that in the W15 case the differences are very small. The red and yellow data curves switch the order of the fork correction application: The ’KWT Uncorrected Data + CFD Fork correction + KWT Wall Corrections’ curve (red) applies the fork correction in the "standard" KWT order. The ’KWT Online Data + CFD Fork correction’ applies the fork correction after the blockage and wall corrections. Recall that "Online Data" are the results from the KWT corrected, except for the fork mount. That is, it inherently includes the KWT wall and blockage corrections. In figs. 7.1 and 7.5 the "correct" (standard KWT process) application order (yellow) follows the "incorrect" order (red) almost identically. There is no discernible difference. In the W15 case, the order of application of corrections is not important.

Evident from the figures is the fact that the CFD derived fork corrections are too large in lift relative to the KWT corrections, and this is most notably expressed in the lift to drag ratio, Figure 7.4, which is effectively shifted down in alpha. This was expected considering the conclusions of lift-loss over-prediction in Section 4.1 mainly due to the forces on the FPA, not the induced interference. Figure 7.1 shows the CFD drag correction is too great at high alpha cases.

The CFD pitching moment correction looks much closer to the standardized KWT fork correction, Figure 7.3, with both the KWT and CFD applied blockage and wall corrections. For the purposes of plotting, wall and blockage corrections are designated only as wall corrections since the walls of the test section do influence the blockage corrections.

Given the drag and lift over-predicted corrections from CFD, hybrid corrections were produced to improve the corrections to the fork mount. Refer back to Figure 4.17 to see how CFD did not capture the lift-based fork correction exceptionally well - the hybrid correction is an attempt to use the KWT Standard fork correction with corrections to it based on CFD results.

The **hybrid fork correction** uses the KWT drag correction and adds 33.5 drag counts (taken from Section 4.4), uses the standardized KWT lift correction (i.e. disregard the CFD lift correction because it was too great), and the CFD pitching moment correction (because CFD predicted the linearity of the fork pitching moment correction with the NACA wing, now use the linearized fork pitching moment correction with the W15). The resulting adoption of this correction brings the resulting curves closer to the simulated W15 freestream case yet not dissimilar to the KWT final data, Figures 7.1 - 7.7.

The difference between the KWT wall corrections and the CFD derived wall corrections with the hybrid fork correction (green and light blue curves, respectively) is more subtle. The KWT correction looks like a possible over-correction for lift, drag, and especially pitching moment at high angles of attack. Referring back to the comparison of the pitching moment wall and blockage correction in Figure 5.4, the KWT correction is much greater in slope and magnitude. Also notable is the effect of the vortex breakdown near 8 degrees of angle of attack on the pitching moment blockage and wall correction from the CFD data, something that is missing from the KWT corrections, which are derived from theoretical equations for attached flow.

Considering the CFD wall effects were calculated without the presence of the fork mount and fairing, perhaps the increased dynamic pressure adjustment from the blockage correction done by the KWT (including the blockage of the MSS fairing) is the cause of the steeper slope of the pitching moment wall effects. On the other hand, the fork mount does create a loss of lift, which in turn lowers the pitching moment effect of the walls (since Shindo's corrections are functions of lift). Thus, considering the improvement in the lift, drag, and pitching moment curves relative to the CFD freestream simulations, the CFD blockage and wall corrections are taken to be more accurate.

Therefore, for the W15 alone case, it appears that the best set of corrections are the hybrid fork corrections and the CFD derived wall and blockage correction.

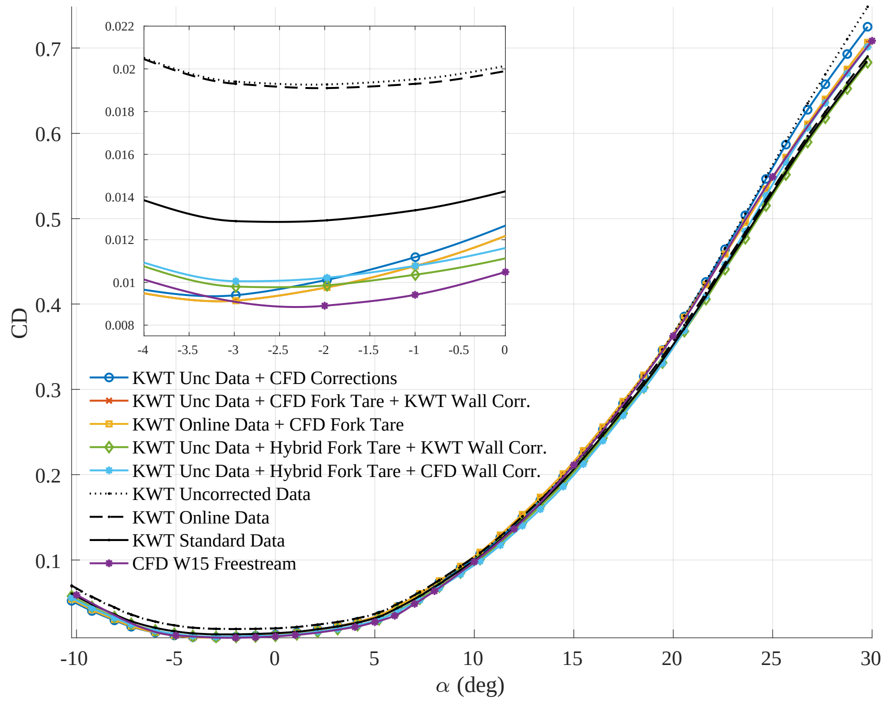

Figure 7.1: Various Correction Methods to W15 KWT Data - Drag vs. α

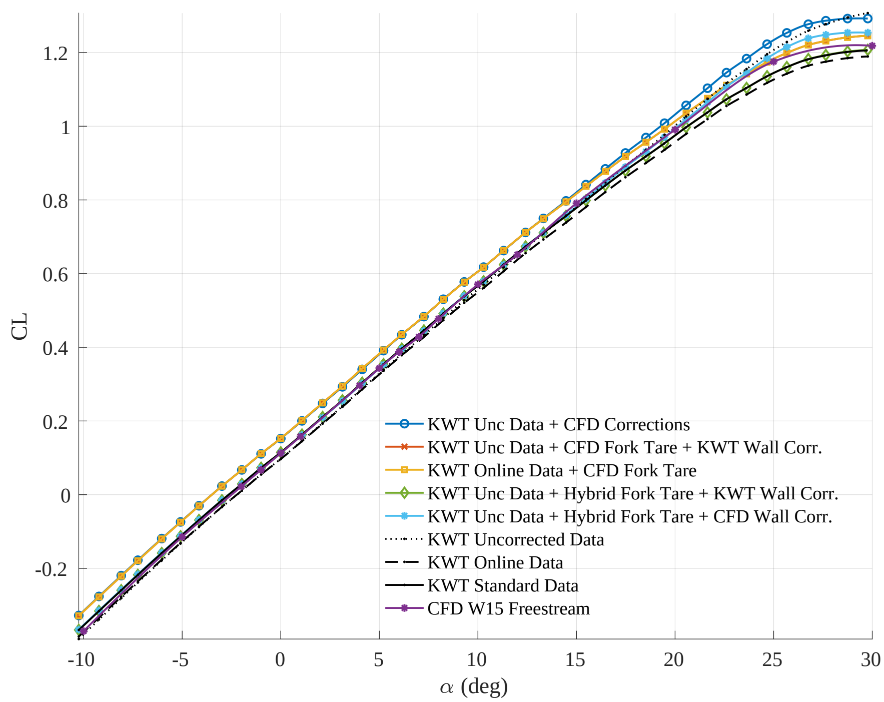

Figure 7.2: Various Correction Methods to W15 KWT Data - Lift vs. α

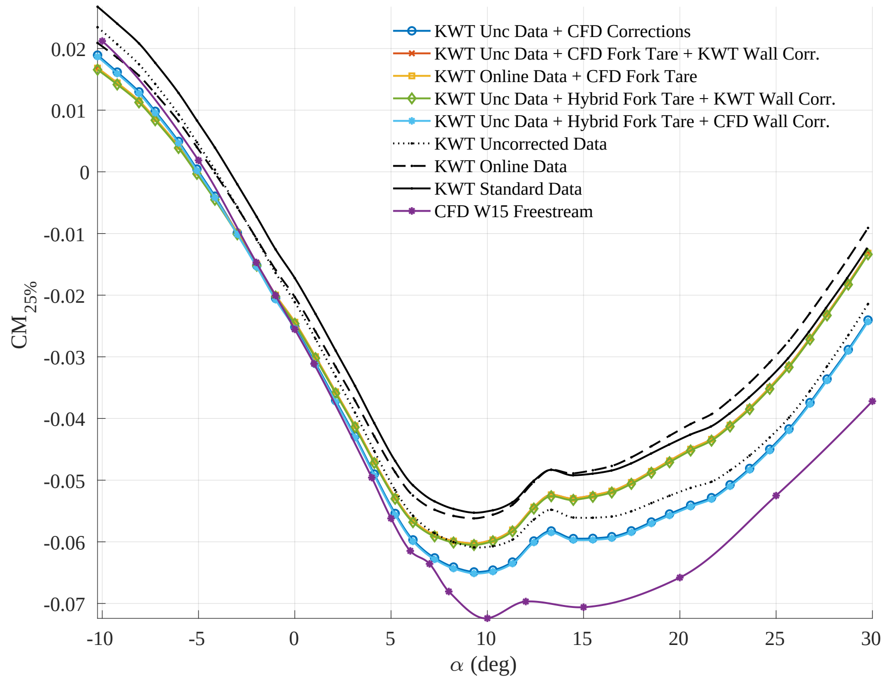

Figure 7.3: Various Correction Methods to W15 KWT Data - PM vs. α

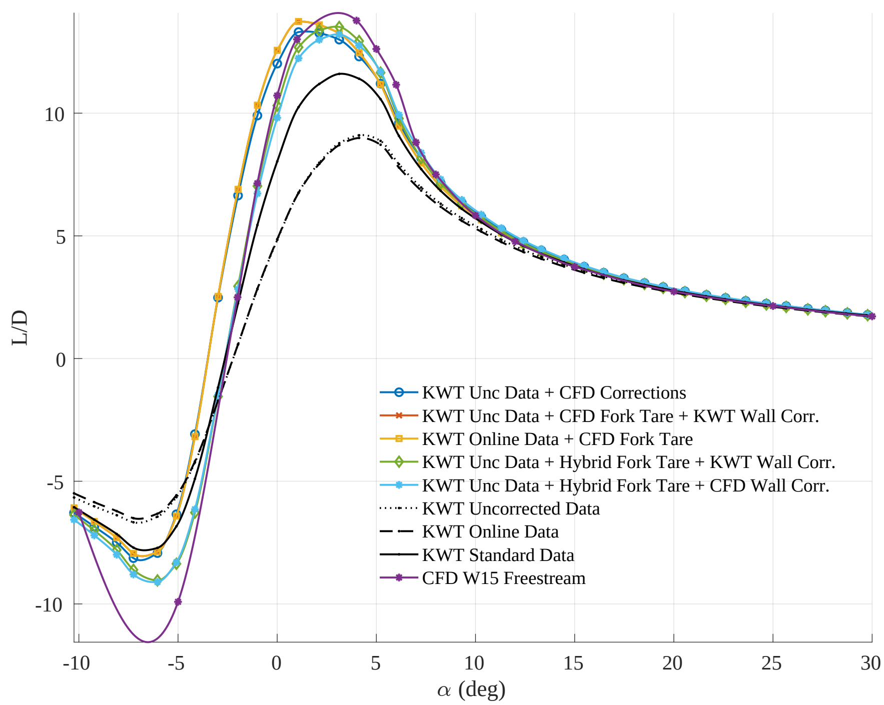

Figure 7.4: Various Correction Methods to W15 KWT Data - L/D vs. α

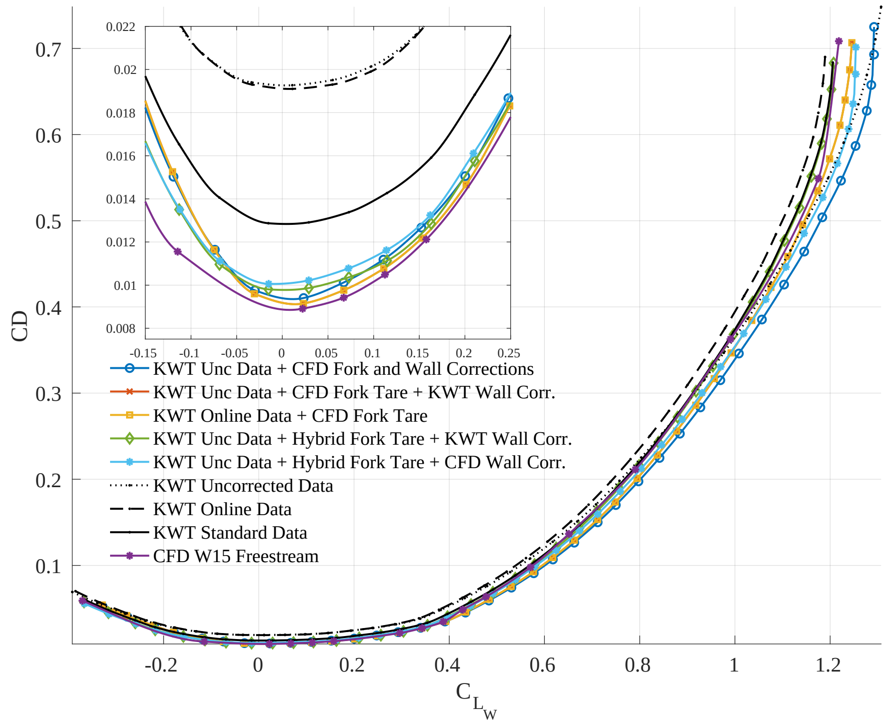

Figure 7.5: Various Correction Methods to W15 KWT Data - Drag vs. C_{L_W}

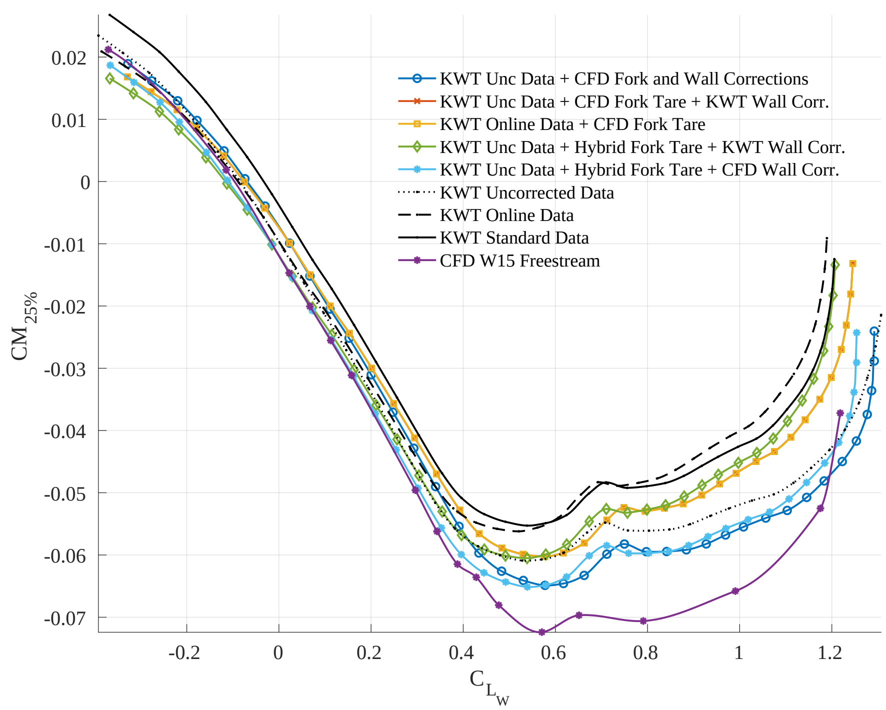

Figure 7.6: Various Correction Methods to W15 KWT Data - PM vs. C_{L_W}

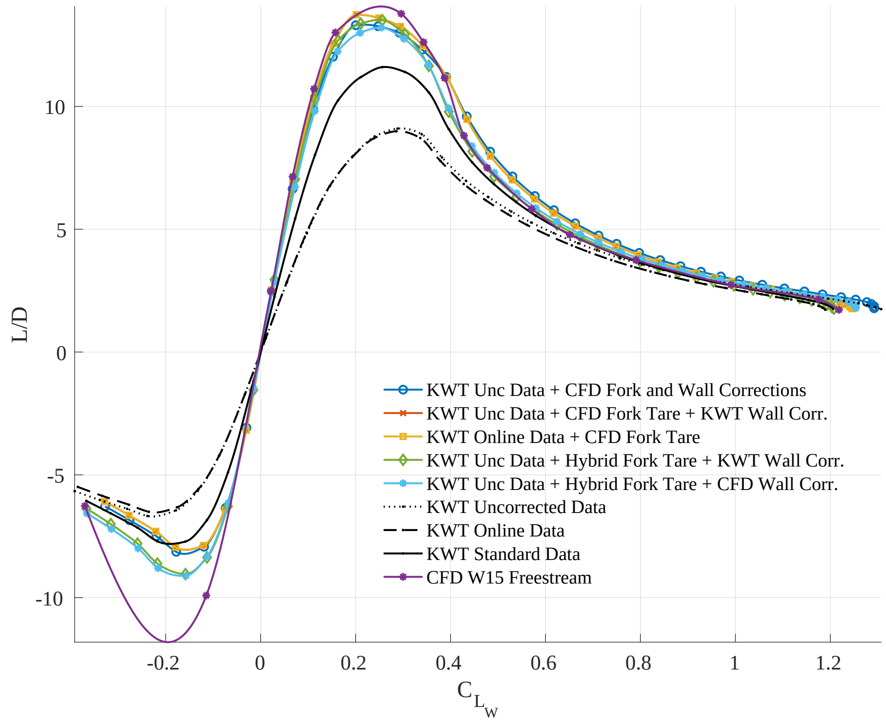

Figure 7.7: Various Correction Methods to W15 KWT Data - L/D vs C_{L_W}

7.1.2 Sideslip

The side force loads predicted by the CFD simulations are vastly lower than those provided by the KWT, Figure 7.10, which in turn also has the same effect of the yawing moment, Figure 7.13. This is likely due to the asymmetric forces and moments of the FPA (recall Figure 4.30). Adding the hybrid yaw FPA T&I correction (which accounts for the asymmetries) to the uncorrected data improves the asymmetries and brings the curves closer to the CFD freestream predictions.

In the pitching moment case, Figure 7.11, using the CFD derived fork corrections replicates the exponential shape of the curve from CFD freestream simulations. The drag correction is greatly improved, nearly equaling the CFD predicted drag value and flattening the curve to be more symmetric. This is because the CFD derived corrections take into account the most recent KWT data of the fork, including the asymmetries. The lift correction also appears to draw the experimental data closer in agreement with the CFD data, Figure 7.9. However, the new hybrid yaw corrections add a slight slope to CL with yaw. The difference between the KWT applied wall corrections and the CFD derived wall corrections initially seemed large, Figure 5.5, comparing the application of the two shows the differences are negligible in the side force, rolling moment, and yawing moment. The differences that appear in lift, drag, and pitching moment are primarily differences stemming from the lift-based wall correction since the wing is at a small lift coefficient at 0 degrees of angle of attack.

The asymmetries, and sharp moment curve break at 0 degrees of sideslip, in the side force and yawing moment needs investigation as possible vortex hysteresis or LE suction hysteresis. This could also be from worn bushir

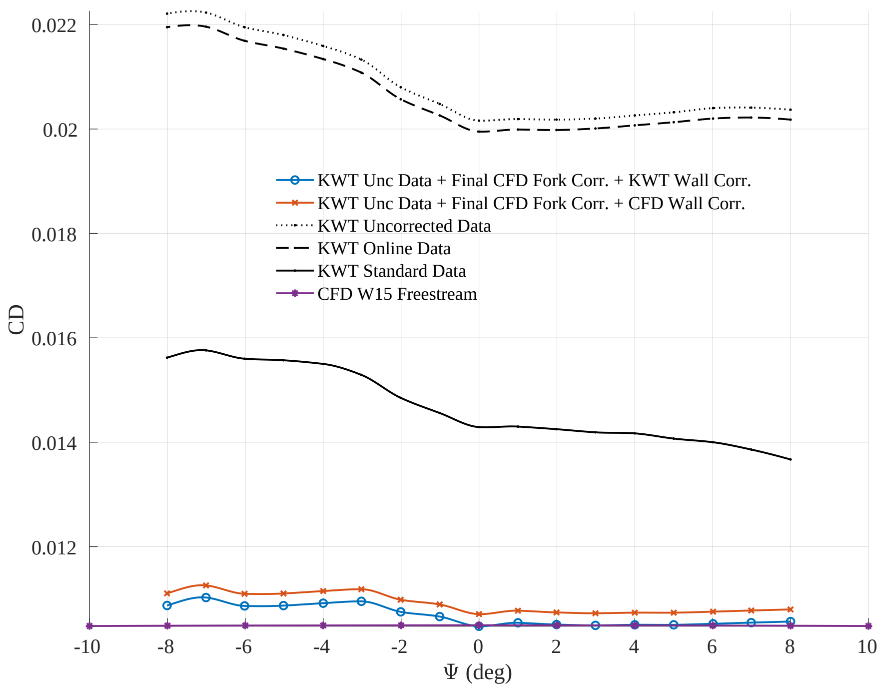

Figure 7.8: Various Correction Methods to W15 KWT Data - Drag vs. Ψ

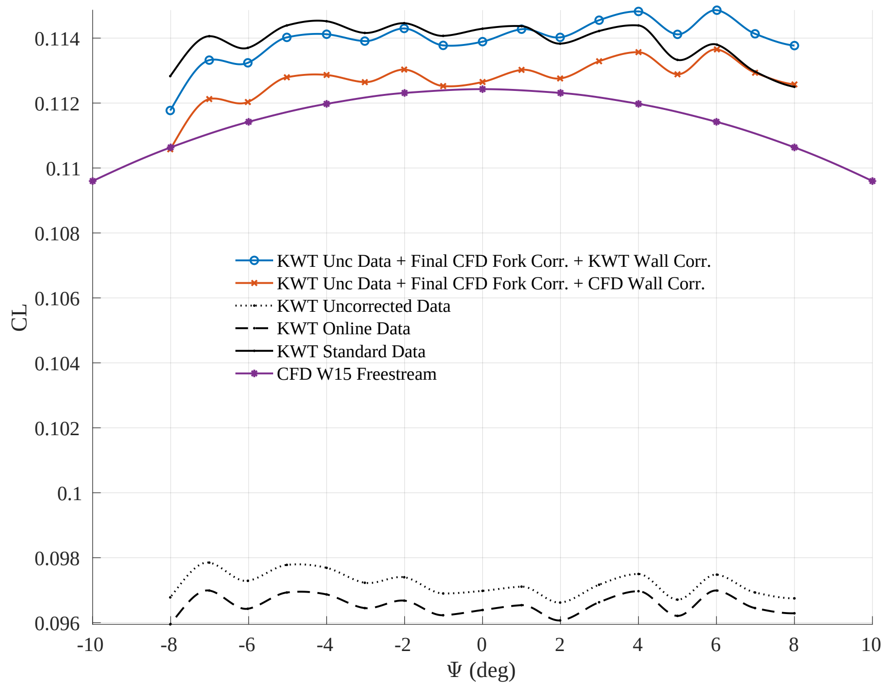

Figure 7.9: Various Correction Methods to W15 KWT Data - Lift vs. Ψ

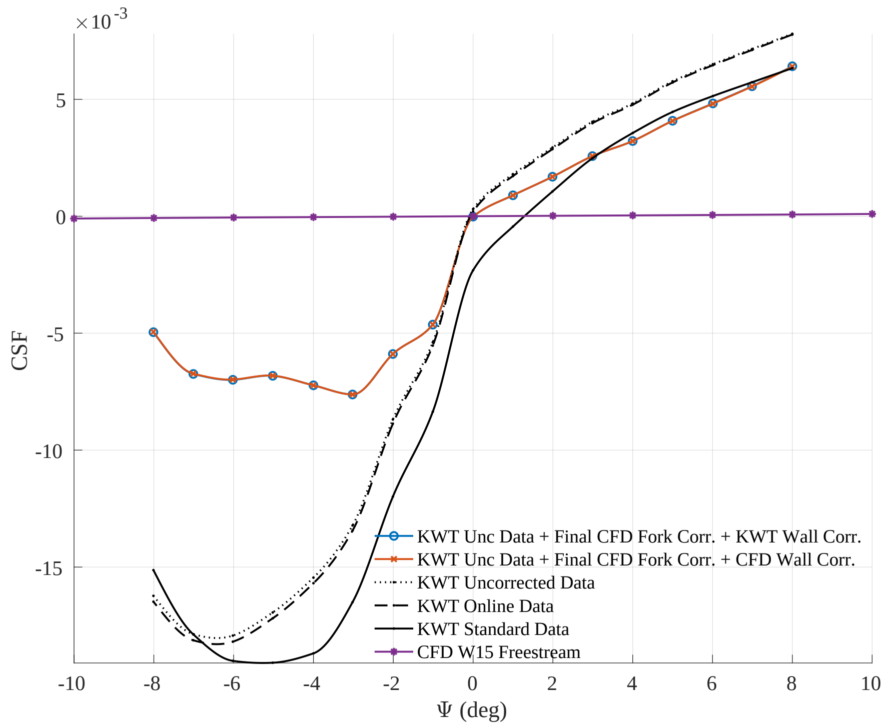

Figure 7.10: Various Correction Methods to W15 KWT Data - Side force vs. Ψ

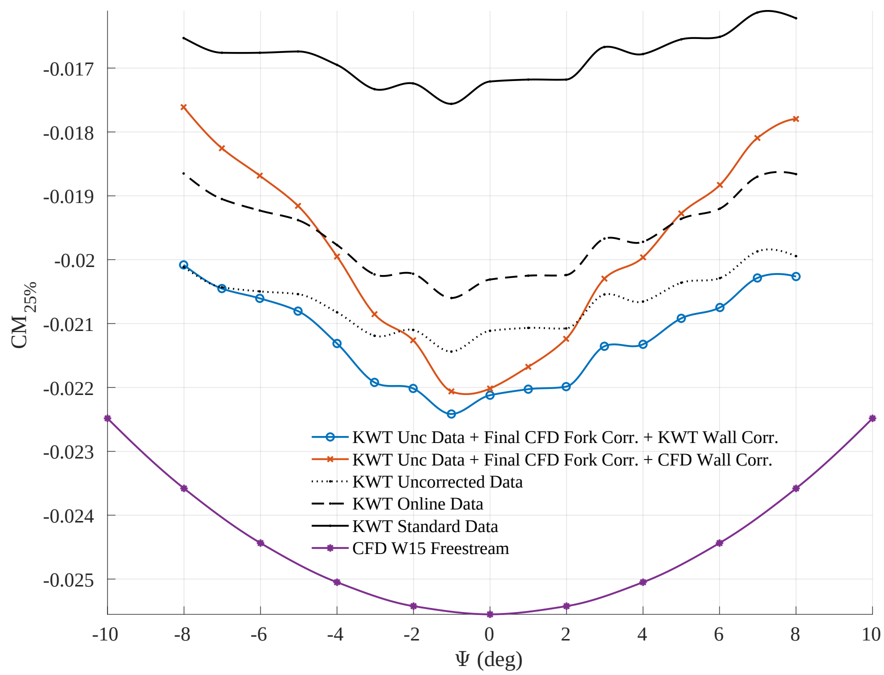

Figure 7.11: Various Correction Methods to W15 KWT Data - Pitching Moment vs. Ψ

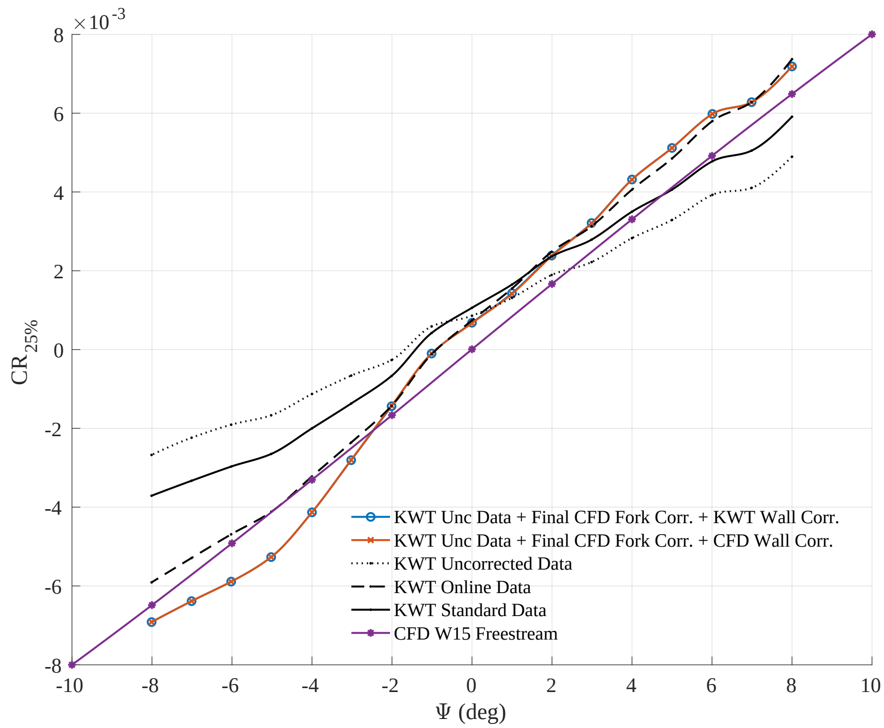

Figure 7.12: Various Correction Methods to W15 KWT Data - Rolling Moment vs. Ψ

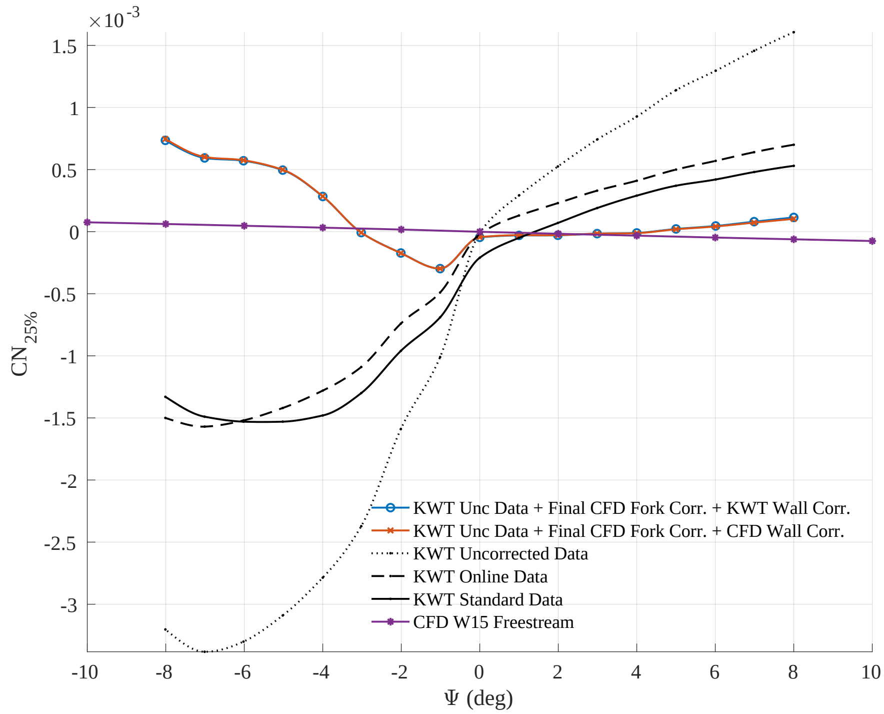

Figure 7.13: Various Correction Methods to W15 KWT Data - Yawing Moment vs. Ψ

7.2 2020 Baseline Configuration without Nacelles

7.2.1 Lift

The hybrid lift and drag corrections look much improved on this configuration as well; the corrected test data appears to compare well to both AD Flow and Star-CCM+ data, Figures 7.14, 7.15 and 7.18. The corrected pitching moment data (which uses the CFD derived correction), shifts the entire curve down and away from both CFD predictions and KWT Standard data, Figures 7.16 and 7.19. This is not surprising, in fact it is expected because the full configuration (the 2020 Baseline) has horizontal stabilizers and canards, both of which greatly impact pitching moment and the corresponding correction.

However, at and past 5 degree of angle of attack, the corrected data looks like it could be more accurate but it is hard to say with certainty because RANS solutions are known to be less dependable when the flow is highly separated. With this taken into consideration, it is most likely that the nose and canards of the configuration alter the flow around the fork mount enough to completely change the interference effects, specifically for the pitching moment, recall Figure 4.41. A pitch angle of five degrees is a reasonable amount of pitch (considering the long lever arm, about 1.5 m) to presume the fork mount is free of the nose and canard wake. Below this value, it is reasonable to presume the fork mount is entirely in the nose and canard wake. Additionally, the CFD simulations suggest a greater pitching moment past 15 degrees, perhaps suggesting neither CFD nor KWT pitching moment corrections are sufficient for aft horizontal stabilizers. Therefore, a new correction should be calculated for a configuration donning a nose, canards, and aft horizontal stabilizers.

It should be noted that the blockage and wall corrections applied to the uncorrected data here are newly calculated by taking the difference between Online and Uncorrected data for the 2020 Baseline Configuration, which

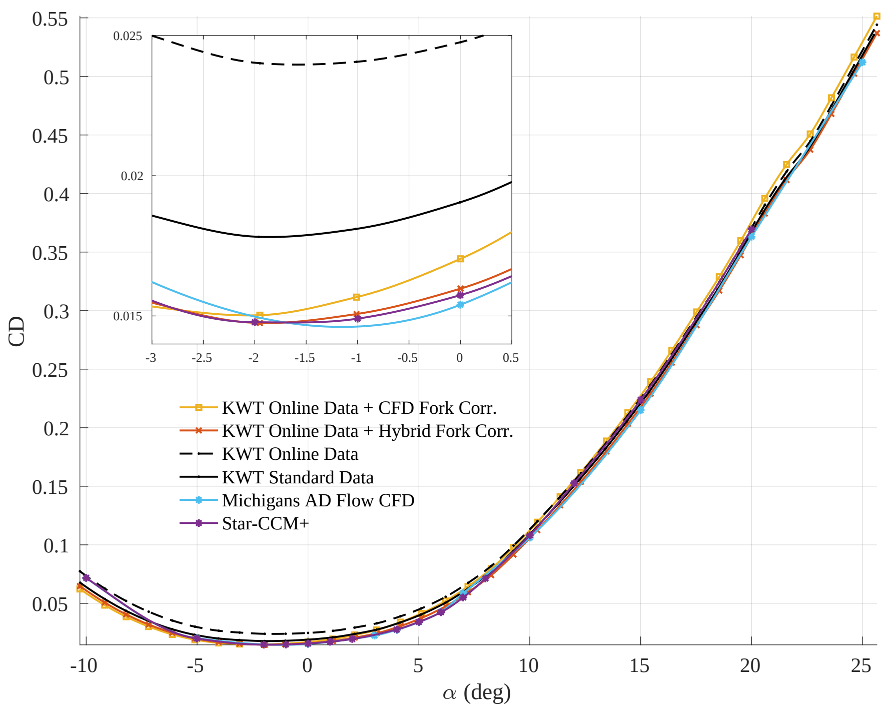

Figure 7.14: Various Correction Methods to 2020 Baseline No Nacelles KWT data - C_D vs. α

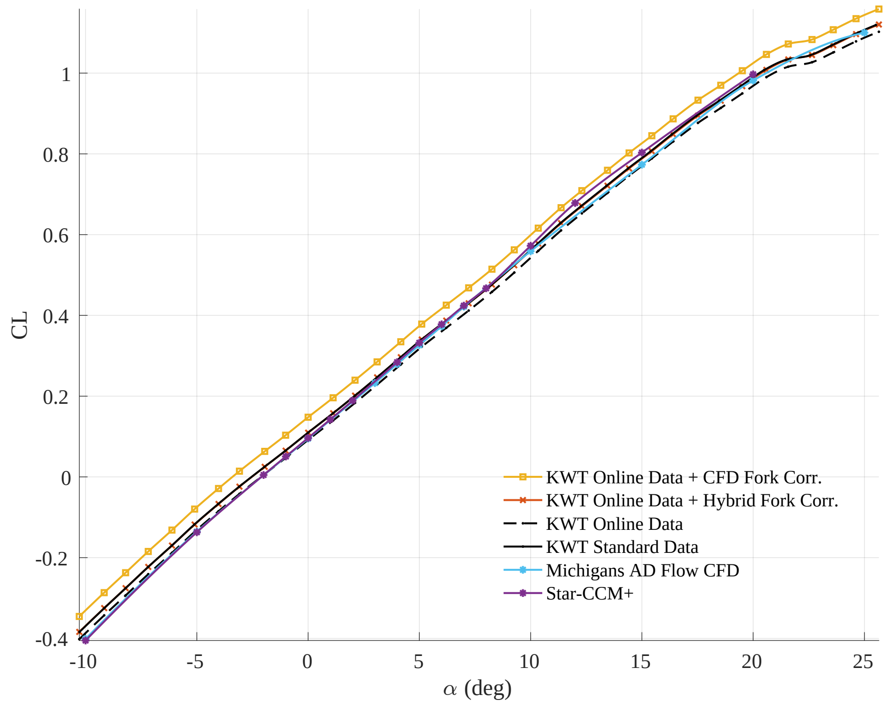

Figure 7.15: Various Correction Methods to 2020 Baseline No Nacelles KWT data - C_L vs. α

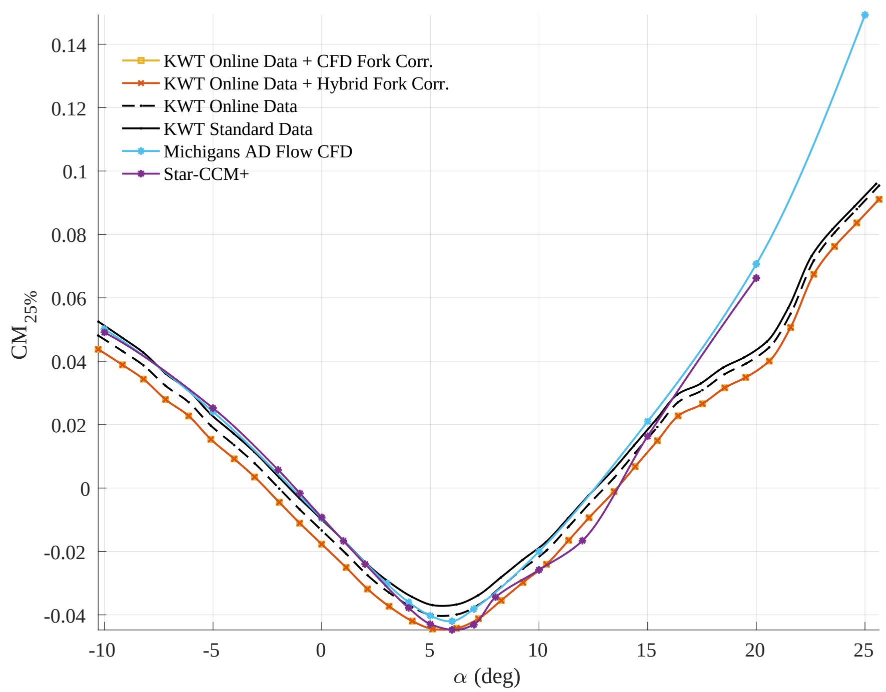

Figure 7.16: Various Correction Methods to 2020 Baseline No Nacelles KWT data - C_M vs. α

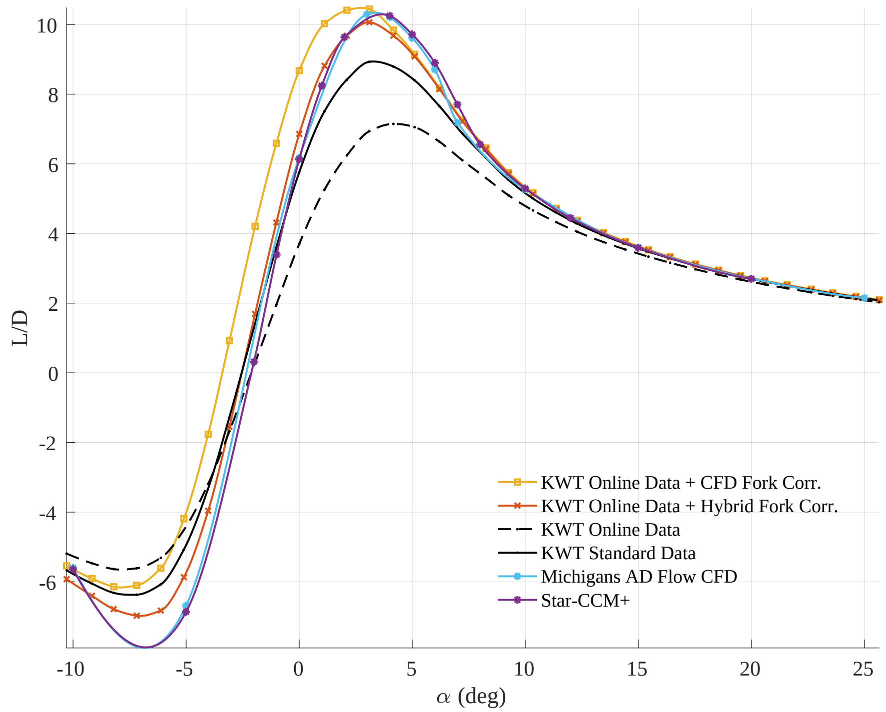

Figure 7.17: Various Correction Methods to 2020 Baseline No Nacelles KWT data - L/D vs. α

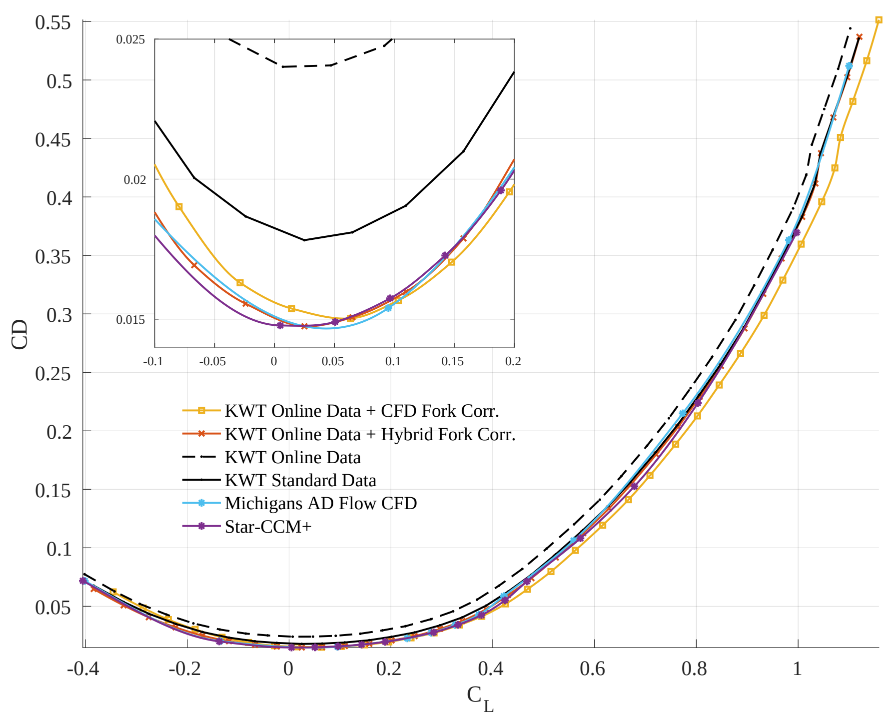

Figure 7.18: Various Correction Methods to 2020 Baseline No Nacelles KWT data - C_D vs. C_L

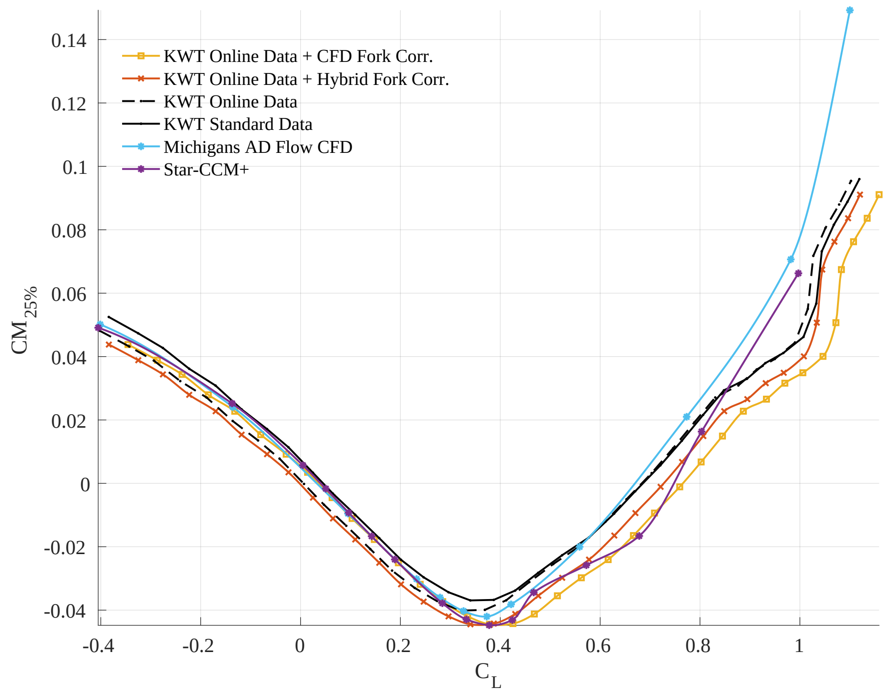

Figure 7.19: Various Correction Methods to 2020 Baseline No Nacelles KWT data - C_M vs. C_L

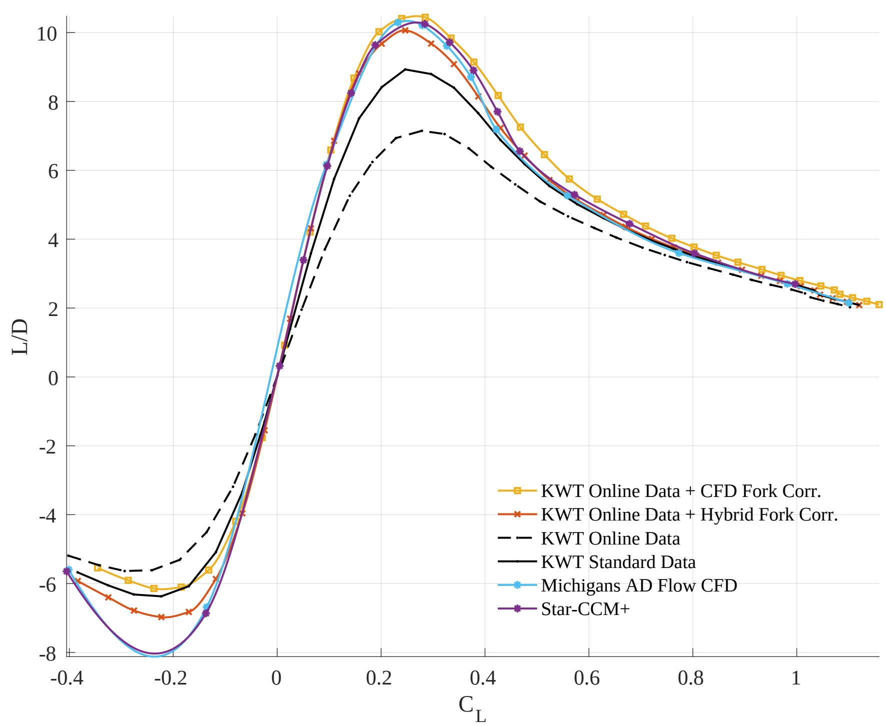

Figure 7.20: Various Correction Methods to 2020 Baseline No Nacelles KWT data - L/D vs. C_L

7.2.2 Sideslip

No CFD simulations for the full 2020 configuration were run, neither by myself nor the University of Michigan, and so there are no CFD results to present and compare here. Only the differences between corrections and their respective impacts on the full 2020 Baseline configuration are analyzed. Again, KWT uncorrected data for this configuration was unavailable at the time of writing. In the previous section, it was noted the order of corrections made no discernible difference, therefore using Online data with the fork corrections should look exactly the same as all corrections applied in the correct order.

Also recall that the full fork T&I correction is a combination of the lift-based correction and the yaw-based correction. The first step is to apply the lift-based correction, then the yaw-based correction. The lift-based correction applied here is the Hybrid correction (modified drag, KWT standard lift, CFD PM) and the yaw-based correction is also the Hybrid version (all measure KWT forces/moments corrected with CFD calculated interference values).

Applying the fork mount sideslip corrections to the KWT online data for this configuration concludes three of the same points as above with the 2020 Baseline lift correction near zero sideslip - the Hybrid fork lift correction is the KWT lift correction, the modified drag correction compares well, and the pitching moment correction shifts the curve in the wrong direction. Again, this indicates the fork lift-based corrections are very sensitive to configuration and the W15 fork lift-based correction does not work well for the full configuration - new fork lift-based corrections must be created for a configuration with canards and horizontal stabilizers.

The yaw-based corrections improve the symmetry of the curves in every case with worsening the asymmetry very slightly in the lift curve. The side force, rolling moment, and yawing moment Hybrid fork corrections have a small yet notable effect when applied to the Online data for the full configuration. The effects are much less significant than those applied to W15 alone. The CFD corrections generally make the yawing data of the configuration more linear yet overall the curves do not drastically differ from the Standard data.

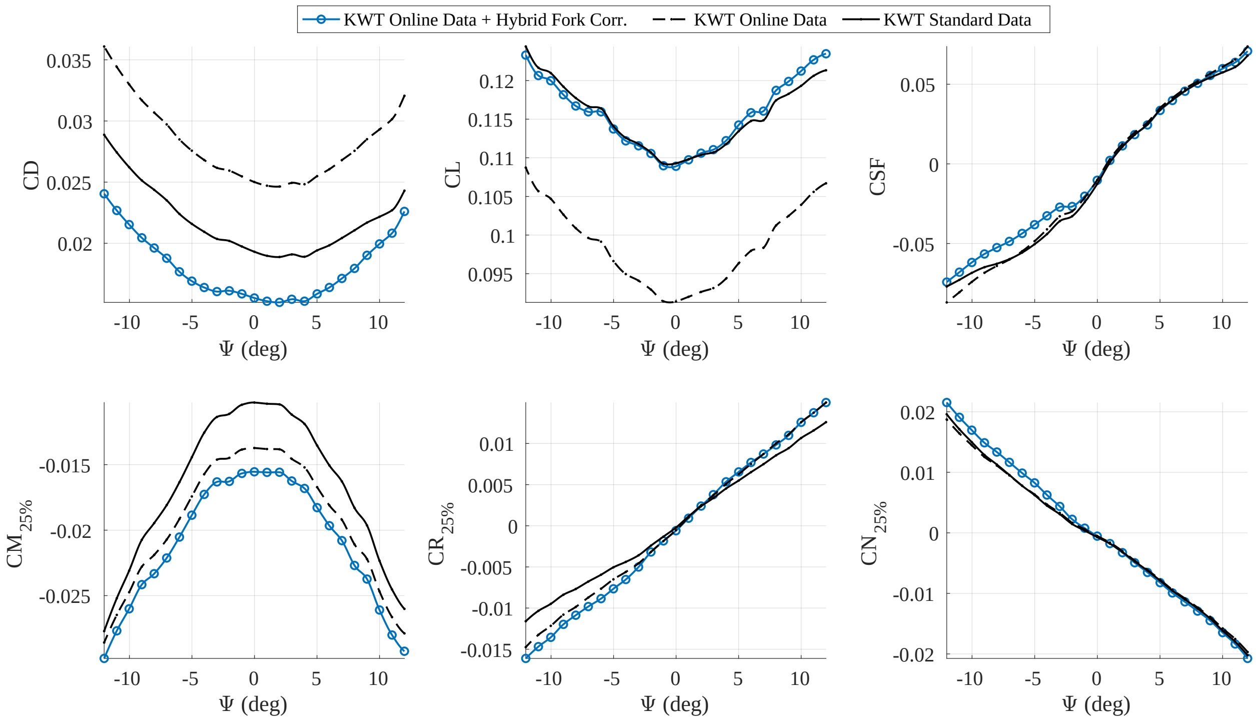

Figure 7.21: Various Correction Methods to 2020 Baseline No Nacelles KWT data vs. Ψ

7.3 2020 Baseline Configuration

The results presented here are selected to show the effects of the nacelle corrections on a configuration with nacelles. While the force components of the internal duct drag are seemingly very small (about 5.8 counts of drag per nacelle) and have little impact on the lift, drag, and pitching moment curves, Figures 7.22 to 7.24, 7.26 and 7.27, the impacts on the lift to drag ratio, i.e. the airplane performance at cruise, is not small Figures 7.25 and 7.28. All of the figures presented in this section also show the importance of accurate fork mount corrections to the evaluation of airplane performance.

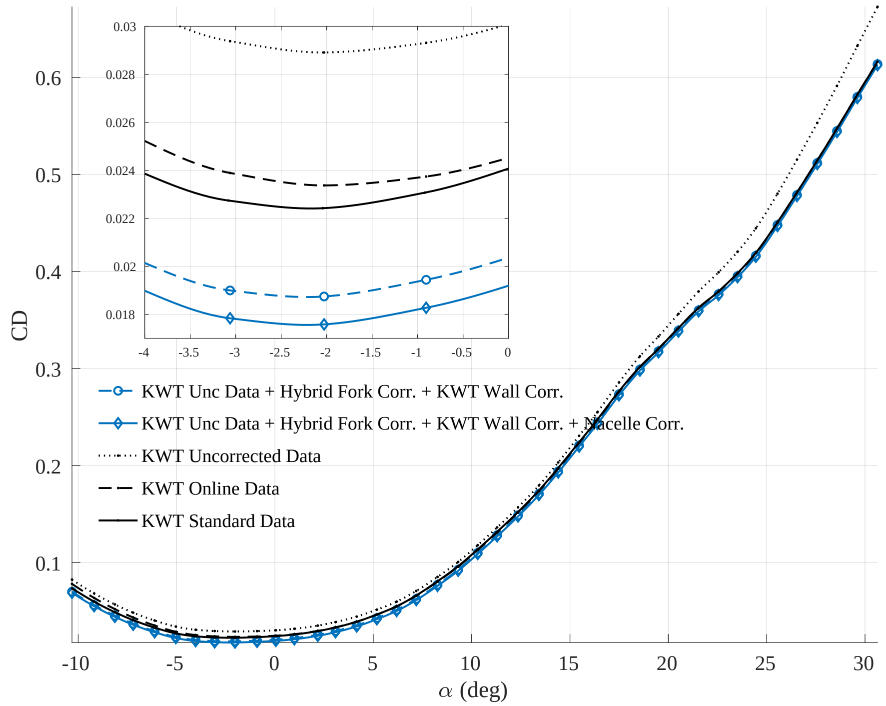

Figure 7.22: Various Correction Methods to 2020 Baseline KWT data - C_D vs. α

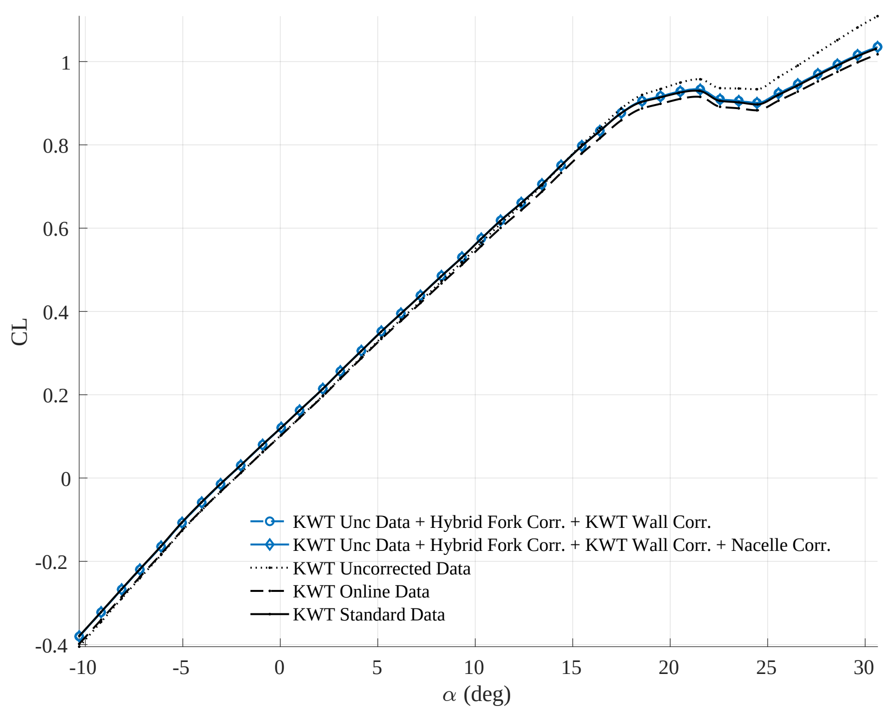

Figure 7.23: Various Correction Methods to 2020 Baseline KWT data - C_L vs. α

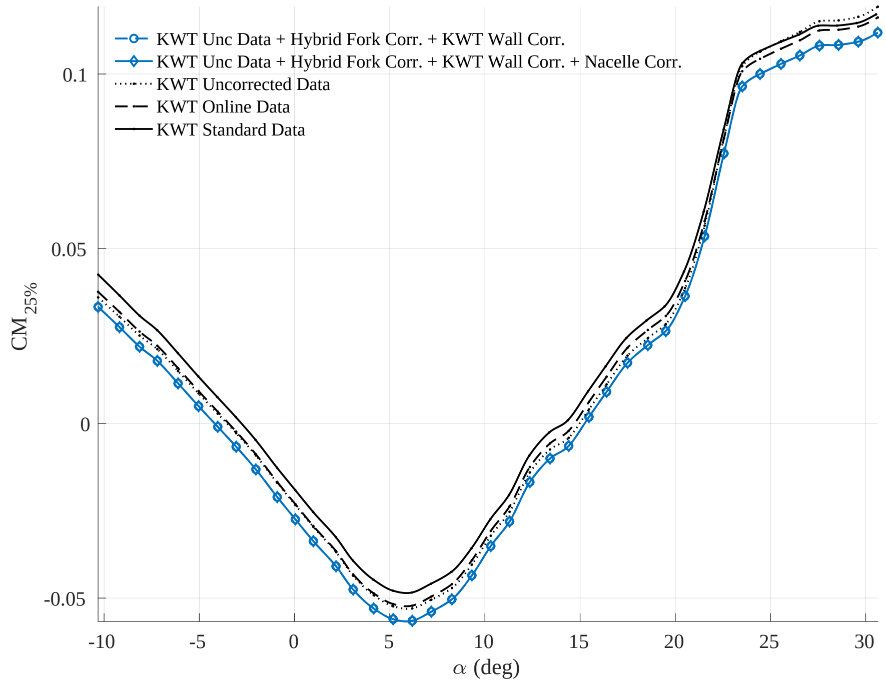

Figure 7.24: Various Correction Methods to 2020 Baseline KWT data - C_M vs. α

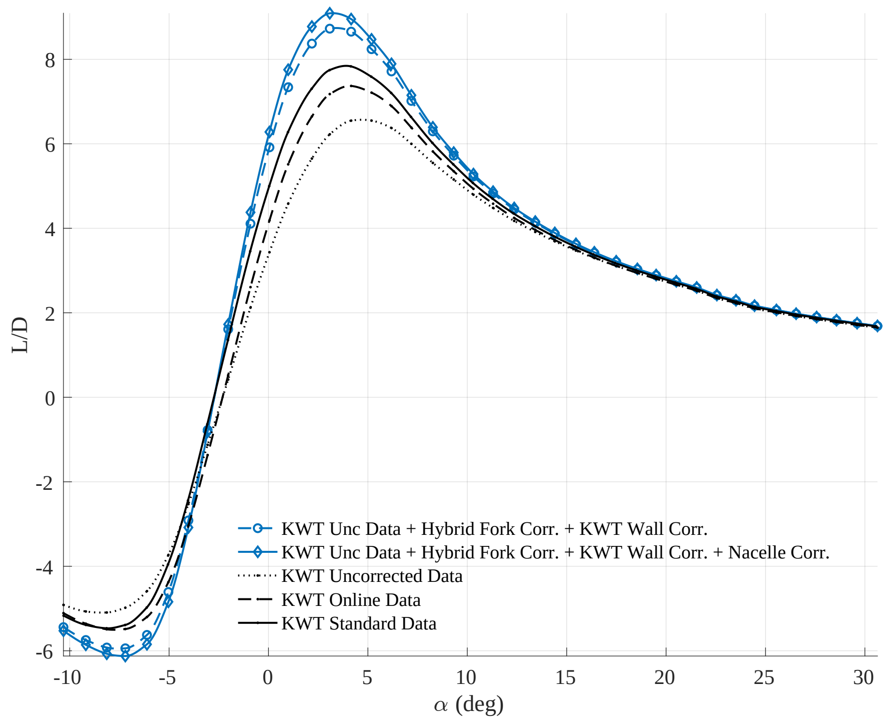

Figure 7.25: Various Correction Methods to 2020 Baseline No Nacelles KWT data - L/D vs. α

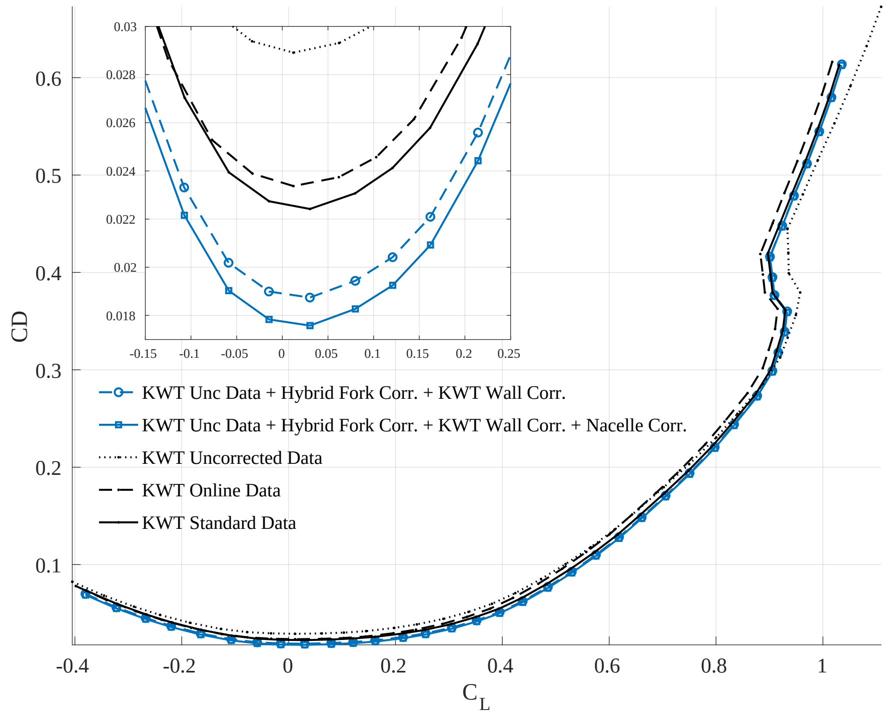

Figure 7.26: Various Correction Methods to 2020 Baseline No Nacelles KWT data - C_D vs. C_L

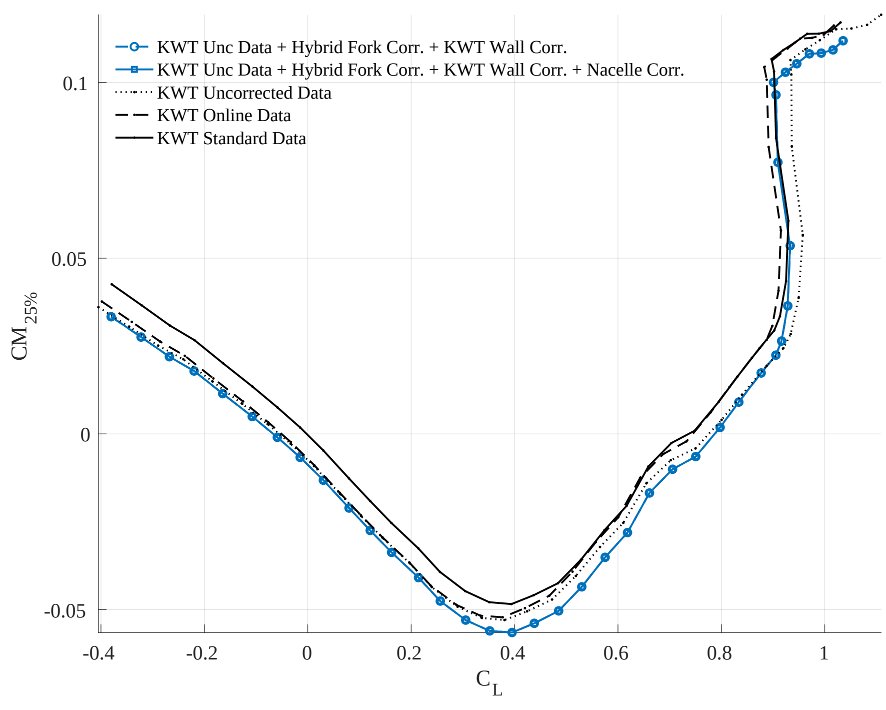

Figure 7.27: Various Correction Methods to 2020 Baseline No Nacelles KWT data - C_M vs. C_L

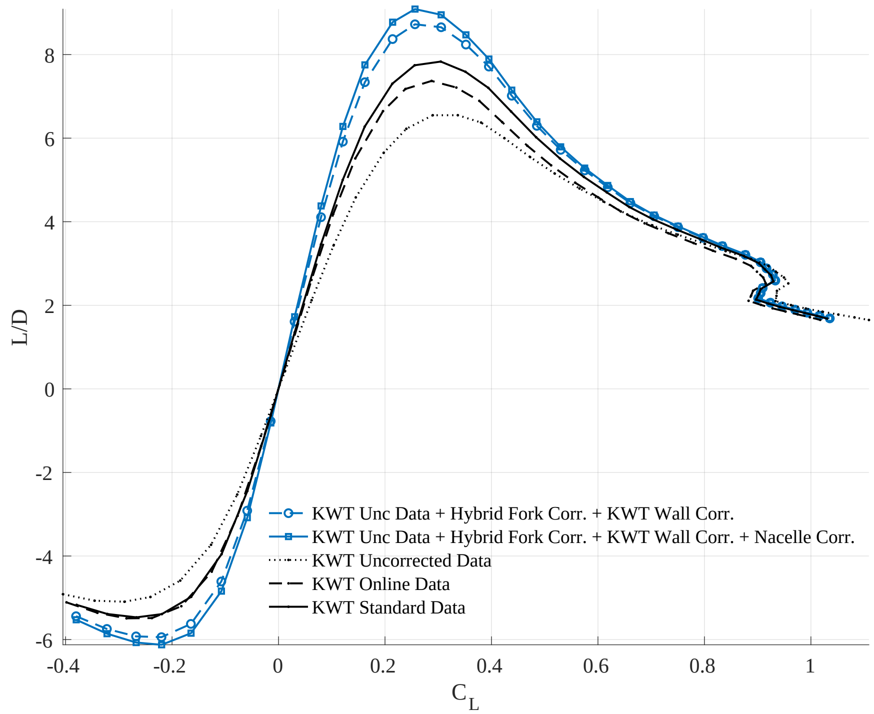

Figure 7.28: Various Correction Methods to 2020 Baseline No Nacelles KWT data - L/D vs. C_L

7.4 Final MSS Corrections

Following the conclusions from the application of multiple corrections, we arrive at the facts:

1. lift-based fork correction depends greatly on the configuration with the pitching moment correction being most sensitive to configuration changes

2. CFD was unable to accurately predict the lift-based, lift and drag corrections. Therefore the KWT standard corrections are used with a CFD incremental adjustment to the drag corrections. Linearized pitching moment corrections appear to be an improvement on the KWT standard correction for the case of W15 alone.

3. KWT data coupled with CFD increments produced good sideslip corrections.

The final MSS corrections are in Figures 7.29 and 7.30. The sideslip-based corrections are shifted to start at zero as they are intended to function as incremental corrections to the lift-based corrections.

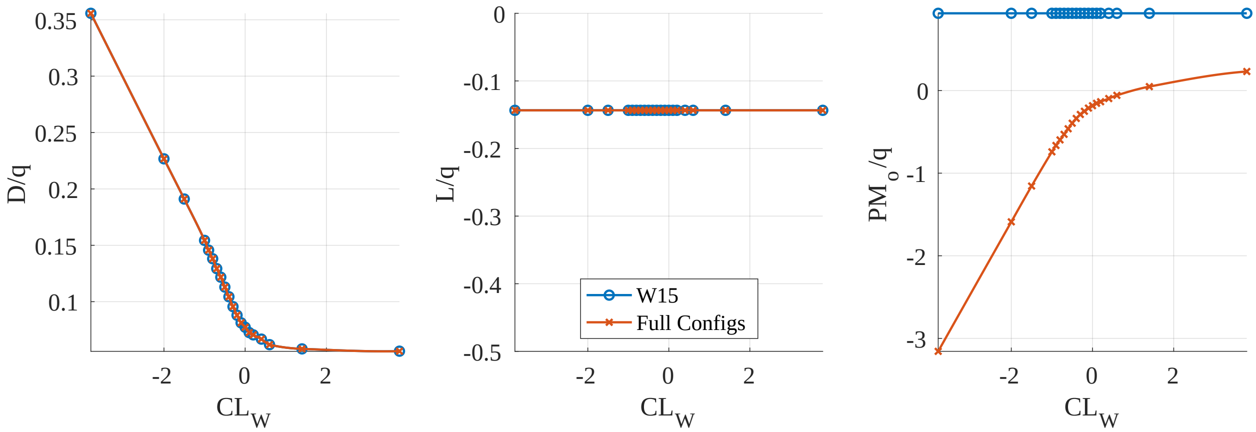

Figure 7.29: Final Fork Lift Tare for SCALOS Models

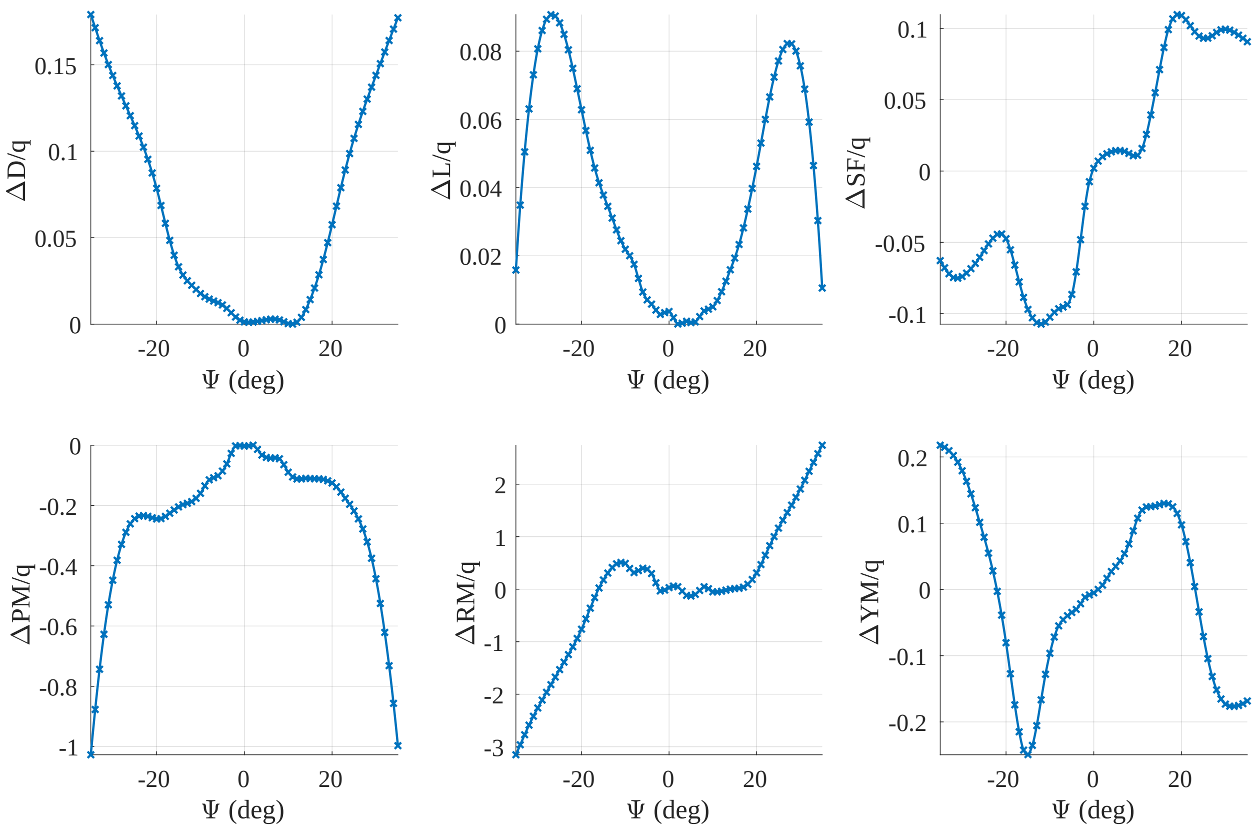

Figure 7.30: Final Fork Sideslip Tare for SCALOS Models

Chapter 8

Conclusion

The development of corrections that would transform measured wind tunnel test results to results for the model in free flight is an essential part of any wind tunnel test since in the end it is the free flight information that is sought. Commonly, and especially in the case of new configurations, such corrections are based on tests of the model on its support system in various positions in the presence of an image support system from the ceiling of the tunnel and without it.

But often there are not enough time and budget for such tests, and wind tunnel tests have to move forward fast. In such cases each wind tunnel has its set of standard corrections for its test section and support systems. Such corrections may or may not be accurate enough for particular cases of interest. The growing practicality and accuracy of RANS-based CFD has made it possible to establish wind tunnel corrections based on CFD simulations.

In the case of the SCALOS project, the expectation was that the standard Kirsten Wind Tunnel fork mount corrections would need improvement for the kind of configurations that the SCALOS project spans. Because of the availability of models but not image systems and the capability to mount the models upside down at the early stages of the project, work was launched to examine the KWT corrections, compare them to CFD-based corrections, and lead to improved corrections for the tests. Star-CCM+ was used for the CFD task.

The work progressed as follows:

A rectangular NACA 0015 wing that was used for the KWT corrections, a disk, and a double delta wing

(W15 - a wing-only model) representative of SCALOS configurations were simulated in free flight and on the fork support system that was used for all SCALOS tests. CFD simulations of the configurations within the test section and in free flight (for walls and blockage effects) were carried out using STAR-CCM+. The CFD based corrections were compared to the standard KWT corrections, step by step, following the practice at the KWT of applying corrections for the various wind tunnel effects sequentially.

A new set of corrections was then generated, based on the standrad and CFD-based corrections. Using wind tunnel raw data, corrected results were generated and compared to each other and to CFD results for the models in free flight.

In the absence of measured results for the free flight model configurations, new corrections were developed based on the insights gained by the trends of the various corrected force and moment curves, their differences, and their relation to the CFD free flight results.

The conclusions reached based on the work presented here are:

- RANS-CFD simulations captured the trends of the force and moment curves for the configurations analyzed here quite well, with predictable inaccuracy in regions of flow separation and strong vortex action.

- Differences between the CFD models (with their symmetric or half model meshes) and the actual model hardware, including the fork support, and its asymmetries led to mismatch between CFD predictions and test results especially in the lateral directional cases.

- The "standard" KWT corrections that were developed experimentally years ago based on tests of a rectangular NACA 0015 wing were not adequate for the SCALOS types of configurations with their double delta wings and slender fuselages.

- The new corrections, based on a combination of the standard and W15 CFD based corrections, worked reasonably well overall in the case of the W15 wing that was used to develop them. But they led to results that deviated from the CFD-predicted free flight characteristics in the case of full SCALOS configurations (with tails and canards) in certain cases of force and moment curves. This leads to the conclusion that corrections should be developed separately (by tests or CFD or both) for families of configurations that are much different in shape.

- Overall, the addition of W15 CFD-based corrections to the standard KWT corrections led to corrections that matched free flight CFD simulations of a full configuration (the 2020 configuration) quite well overall.

8.1 Recommended Future Work

In general, more experimentation in CFD modeling is recommended. Also, in addition to the step by step effect by effect approach of creating CFD corrections, create "total" CFD based corrections using simulations of a full model in free flight and the same model on the support system in the wind tunnel. Also, carry out T&I tests with new dummy forks and with the W15 machined to be able to be mounted inverted.

In more detail:

- Perform an additional mesh study on the FPA model.
- Experiment with the K-ω turbulence model (or other more accurate models) and compare the simulations and derived corrections with the corrections using the Spalart-Allmaras model.
- Perform a wall and blockage effect increment calculation with Star-CCM+ for the 2020 baseline configuration or any configuration with a tail. Furthermore, an individual study for T-tail, mid-tail, and low-tail configurations.
- Create "total" CFD based corrections using simulations of a full model in free flight and the same model on the support system in the wind tunnel.
- Perform a standard T&I test in the KWT with an image FPA on W15 and a selected full configuration. This will help validate the CFD created tares and identify the extent to which different model support tares are necessary for configurations with long noses and tails.

Bibliography

[1] of Washington Aeronautics & Astronautics, U., "Kirsten Wind Tunnel Technical Guide - Model Support Effects," , 2022. URL `https://www.aa.washington.edu/AERL/KWT/techguide/modelsupport`.

[2] Barlow, J. B., Rae, W. H. J., and Pope, A., *Low Speed Wind Tunnel Testing*, 3rd ed., John Wiley & Sons, 1999.

[3] Rogers, S., "Report 397-F, Fork Tare and Interference Survey, UWAL 14-H Fork," Tech. Rep. 397-F, University of Washington Aeronautical Laboratory, 1988.

[4] Nelson, C., Ting, K.-Y., Mavriplis, N., Soltani, R., and Livne, E., "Supersonic Configurations at Low Speeds (SCALOS): Project Background and Progress at University of Washington," *AIAA Scitech 2022 Forum*, 2022, p. 1803. doi:{10.2514/6.2022-1803}.

[5] Mavriplis, N., Ting, K.-Y., Soltani, R., Livne, E., and Nelson, C., "Supersonic Configurations at Low Speeds (SCALOS): Test / Simulation Correlation Studies," *AIAA Scitech 2022 Forum*, 2022, p. 1801. doi:10.2514/6.2022-1801.

[6] Benek, J. A., Kraft, E. M., and Lauer, R. F., "Validation Issues for Engine-Airframe Integration," *AIAA Journal*, Vol. 36, No. 5, 1998, pp. 759–764. doi:10.2514/2.434, URL `https://doi.org/10.2514/2.434`.

[7] Ito, Y., Murayama, M., Yokokawa, Y., Yamamoto, K., Tanaka, K., and Hirai, T., "Wind Tunnel Installation Effects on Japan Aerospace Exploration Agency's Standard Model," *Journal of Aircraft*, Vol. 59,

No. 5, 2022, pp. 1281–1302. doi:10.2514/1.C036741, URL https://doi.org/10.2514/1.C036741.

[8] NAMBU, T., HASHIMOTO, A., AOYAMA, T., and SATO, T., "Numerical Analysis of the ONERA-M6 Wing with Wind Tunnel Wall Interference," *Transactions of the Japan Society for Aeronautical and Space Sciences*, Vol. 58, No. 1, 2015, pp. 7–14. doi:10.2322/tjsass.58.7.

[9] Toledano, A., Morency, F., Weiss, J., Broughton, C., and Benmeddour, A., "Improvement of Wall-Corrections at the National Research Council's Trisonic Wind Tunnel," *Journal of Aircraft*, Vol. 56, No. 6, 2019, pp. 2299–2308. doi:10.2514/1.C035545, URL https://doi.org/10.2514/1.C035545.

[10] Waldmann, A., Lutz, T., and Krämer, E., "Wind Tunnel Support System Influence on NASA Common Research Model at Low-Speed Conditions," *Journal of Aircraft*, Vol. 55, No. 5, 2018, pp. 1762–1772. doi:10.2514/1.C034440, URL https://doi.org/10.2514/1.C034440.

[11] University of Washington Aeronautics & Astronautics, "Kirsten Wind Tunnel Technical Guide," , 2022. URL https://www.aa.washington.edu/AERL/KWT/techguide/testsect.

[12] Capstone Class of 2013, "2013 Capstone Project - StarFox - Supersonic Tailless Aircraft: Research for Optimized Cross-Sections," Tech. rep., University of Washington, 2013.

[13] Brian C. Vermeire, H. K., Carlos A. Pereira, *Computational Fluid Dynamics*, Concordia University, 2020.

[14] Rodriguez, S., *Applied Computational Fluid Dynamics and Turbulence Modeling*, Springer, 2019.

[15] NASA, "Isentropic Flow Equations," , 2021. URL https://www.grc.nasa.gov/www/BGH/isentrop.html.

[16] Siemens, "Best Practices: External Aerodynamics for Aerospace Applications," , 2020. URL https://support.sw.siemens.com/knowledge-base/KB000031728_EN_US.

[17] Götten, F., Finger, D., Marino, M., Bil, C., Havermann, M., and Braun, C., "A review of guidelines

and best practices for subsonic aerodynamic simulations using RANS CFD," *Asia Pacific International Symposium on Aerospace Technology*, 2019.

[18] Cadence Design Systems Inc., "Compute Grid Spacing for a Given Y+," , 2022. URL https://www.cadence.com/en_US/home/tools/system-analysis/computational-fluid-dynamics/y-plus.html.

[19] NASA Langley Research Center - Turbulence Modeling Resource, "The Spalart-Allmaras Turbulence Model," , 2022. URL https://turbmodels.larc.nasa.gov/spalart.html.

[20] "Simcenter STAR-CCM+ Documentation," , 2022. URL https://docs.sw.siemens.com/documentation/external/PL20210316104759000/en-US/userManual/userguide/html/index.html.

[21] NASA Langley Research Center - Turbulence Modeling Resource, "Turbulence Model Numerical Analysis - 3D ONERA M6 Wing Validation," , 2021. URL https://turbmodels.larc.nasa.gov/onerawingnumerics_val_sa.html.

[22] Easterbrook, D., "Report 397-B, Fork Tare and Interference Survey, UWAL 14-H Fork," Tech. Rep. 397-B, University of Washington Aeronautical Laboratory, 1956.

[23] Mohammad Kamaruddin, N., "Dynamics and Performance of Flying Discs," Ph.D. thesis, University of Machester, 2011.

[24] Young, A. D., and Paterson, J. H., "Aircraft Excrescence Drag," Tech. rep., NATO Advisory Group for Aerospace Research and Development, 1981.

[25] Shindo, S., "Simplified Tunnel Correction Method," *Journal of Aircraft*, Vol. 32, No. 1, 1995, pp. 210–213. doi:10.2514/3.46705, URL https://doi.org/10.2514/3.46705.

Chapter A

Appendix One

All curves generated from CFD data points was splined with the Makima interpolation function in Matlab.

Nominal definitions for force and moment coefficients are:

$$C_D = \frac{D}{qS_{ref}}$$

$$C_L = \frac{L}{qS_{ref}}$$

$$C_Y = \frac{SF}{qS_{ref}}$$

$$C_M = \frac{PM}{qS_{ref} \cdot MAC}$$

$$C_R = \frac{RM}{qS_{ref} \cdot b}$$

$$C_Y = \frac{YM}{qS_{ref} \cdot b}$$

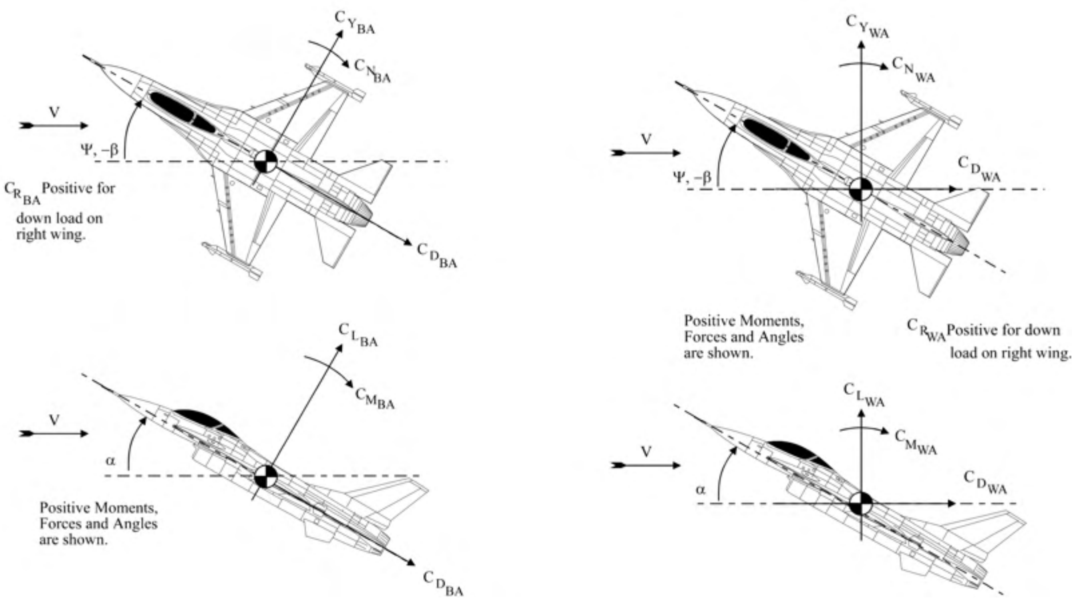

(a) Body Axes Diagram

(b) Wing Axes Diagram

Figure A.1: Axes Diagrams

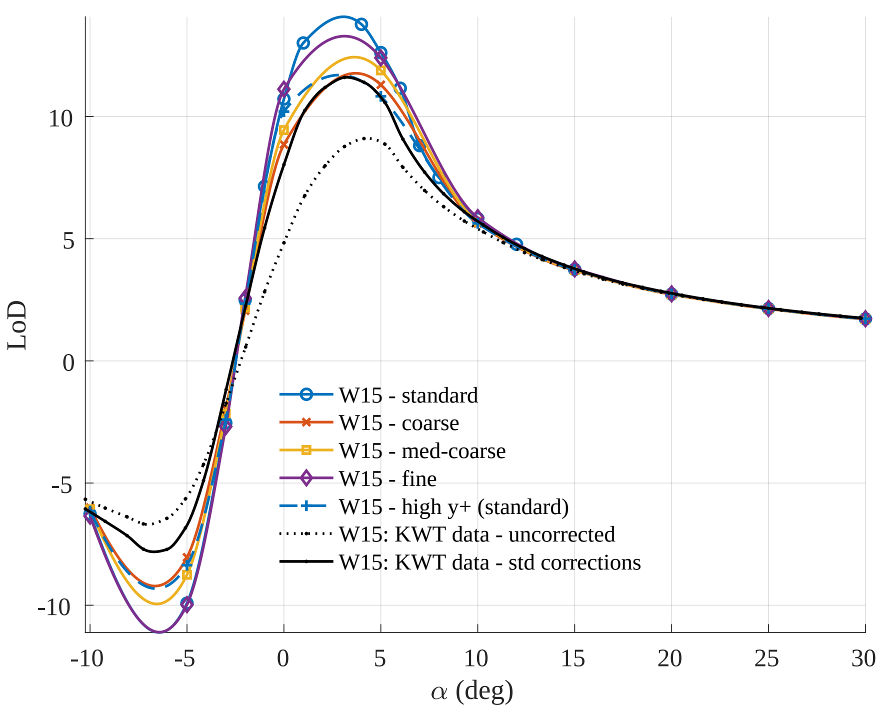

Figure A.2: W15 Drag Polar for Various Meshes vs C_{L_W}

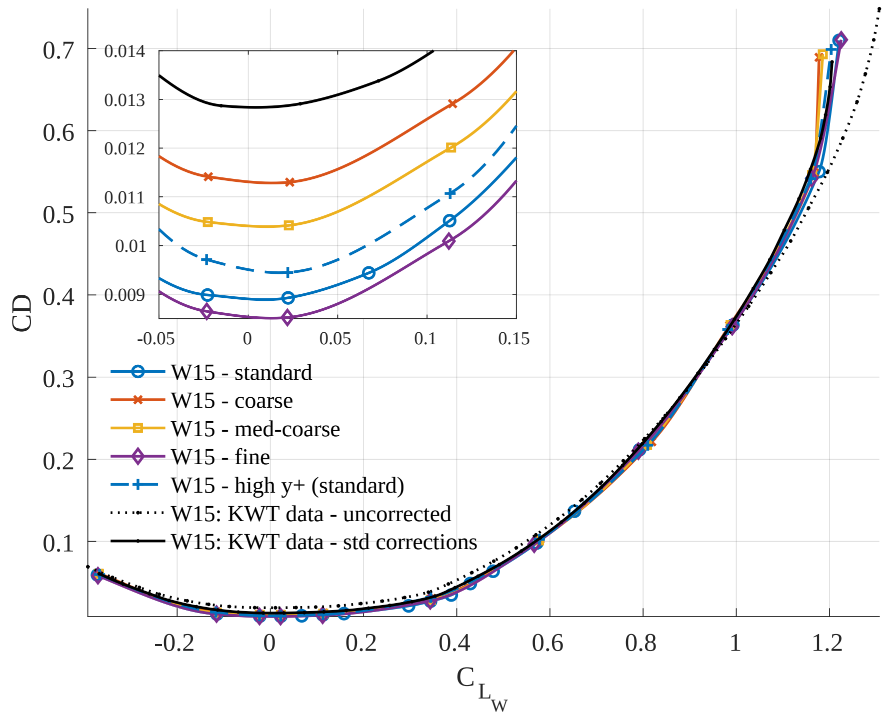

Figure A.3: W15 Lift Curve for Various Meshes vs C_{L_W}

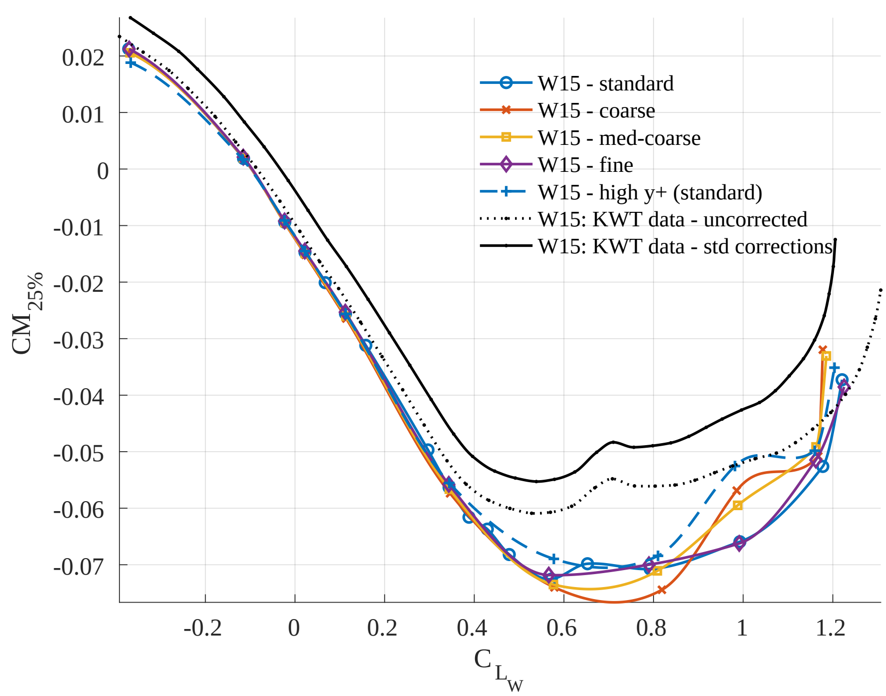

Figure A.4: W15 Pitching Moment for Various Meshes vs C_{L_W}

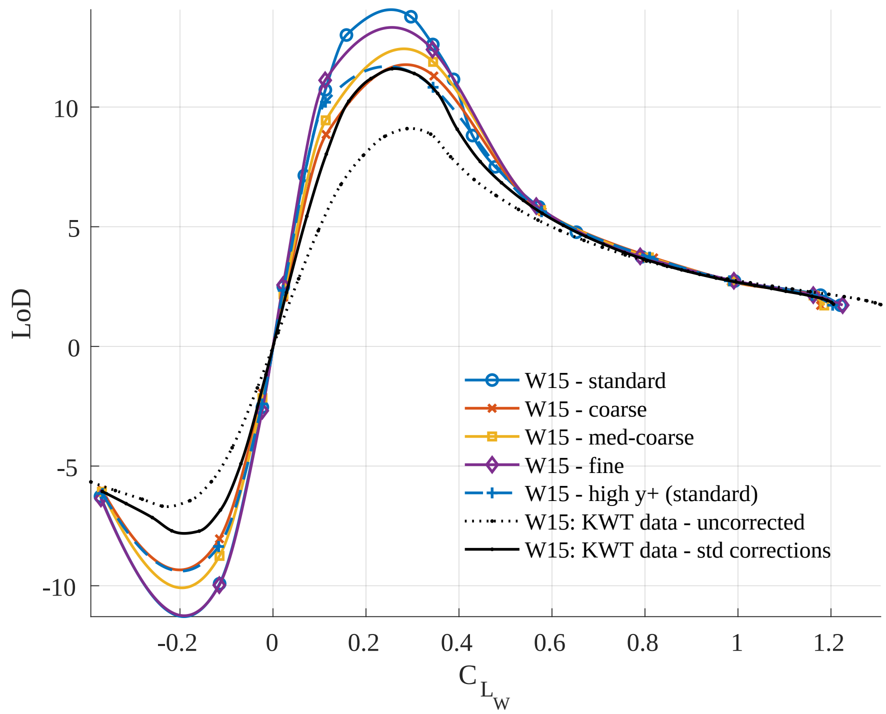

Figure A.5: W15 Lift to Drag Ratio for Various Meshes vs C_{L_W}

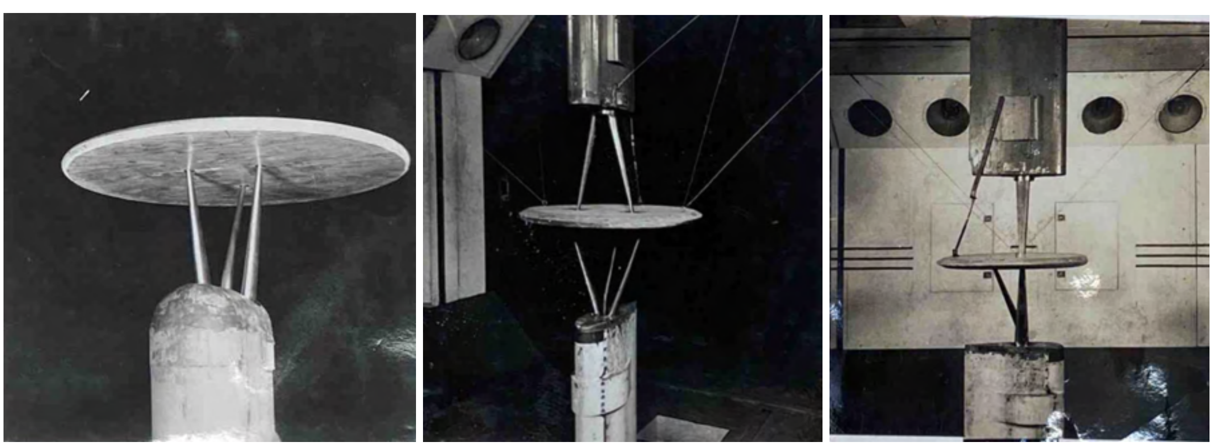

Figure A.6: Photos from the 1956 Fork T+I Test with a Disc Model